UNIVERSITÄT PADERBORN
FAKULTÄT FÜR NATURWISSENSCHAFTEN – DEPARTMENT PHYSIK

Barium Halide Nanocrystals in Fluorozirconate based Glass Ceramics for Scintillation Application

Dissertation zur Erlangung des akademischen Grades
Doktors der Naturwissenschaften
vorgelegt dem
Fachbereich Physik
der Fakultät für Naturwissenschaften
Universität Paderborn
von

DIPL. PHYS. JULIA SELLING

Paderborn, 2007

Abstract

Europium (Eu)-activated barium halide nanocrystals in fluorozirconate based glass ceramics represent a promising class of x-ray scintillators. The scintillation in these glass ceramics is mainly caused by the emission of divalent Eu incorporated in hexagonal $BaCl_2$ nanocrystals which are formed in the glass matrix upon appropriate annealing. Experiments with cerium (Ce)-activated fluorozironate glass ceramics showed that Ce is an interesting alternative. In order to get a better understanding of the scintillation mechanism in Eu- or Ce-activated barium halide nanocrystals, an investigation of the processes in the corresponding bulk material is essential. The objective of this thesis is the investigation of undoped, Eu-, and Ce-doped barium halides by x-ray excited luminescence (XL), pulse height, and scintillation decay spectra. That will help to figure out which of these crystals has the most promising scintillation properties and would be the best nanoparticles for the glass ceramics. Furthermore, alternative dopants like samarium (Sm) and manganese (Mn) were also investigated.

Besides the above-mentioned optical investigation electron paramagnetic resonance (EPR) and Mössbauer measurements were carried out in order to complete the picture of Eu-doped barium halides. The EPR data of Eu-doped BaI_2 is anticipated to yield more information about the crystal field and crystal structure that will help to understand the charge carrier process during the scintillation process. The main focus of the Mössbauer investigations was set on the Eu-doped fluorochlorozirconate glass ceramics. The results of this investigation should help to improve the glass ceramics. The Eu^{2+}/Eu^{3+} ratio in the glass ceramics should be determined and optimize favor of the Eu^{2+}. We also want to distinguish between Eu^{2+} in the glass matrix and Eu^{2+} in the nanocrystals. For a better understanding of Mössbauer spectroscopy on Eu also measurements on Eu in a CaF_2 host lattice were carried out.

In physics, you don't have to go around making trouble for yourself
- nature does it for you.
Frank Wilczek [1]

[1] Nobel prize-winning American theoretical physicist. Along with H. David Politzer and David Gross, he was awarded the 2004 Nobel Prize in Physics "for the discovery of asymptotic freedom in the theory of the strong interaction".

Contents

1 Introduction 1

2 Physical and theoretical background 3
1 Optical Spectroscopy . . . 3
1.1 Photo- and x-ray luminescence . . . 3
1.2 Decay time measurements . . . 4
1.3 γ Spectroscopy: Pulse height spectra . . . 4
2 Electron Paramagnetic Resonance (EPR) . . . 5
3 Mössbauer Spectroscopy . . . 7
3.1 Mössbauer Effect . . . 7
3.2 Mössbauer Isotope ^{151}Eu . . . 8
3.3 Hyperfine Interactions . . . 9

3 Barium halide scintillators for x-ray and γ-ray detections 13
1 Characteristics of scintillators . . . 13
2 Crystal structure . . . 14
3 Sample preparation . . . 17
4 Photoluminescence (PL) . . . 17
5 X-ray excited luminescence (XL) . . . 19
6 Afterglow . . . 23
7 Light yield and energy resolution . . . 25
8 Scintillation decay . . . 29
9 Discussion . . . 32

4 Ce-doped glass ceramics 37
1 Experimental results . . . 38
2 Discussion . . . 41

5 Sm- and Mn-doped single crystals and glass ceramics 43
1 Motivation . . . 43
2 Sample Preparation . . . 44
3 Experimental results . . . 45
3.1 Sm-doped samples . . . 45
3.2 Mn-doped samples . . . 51
4 Discussion . . . 55

6 Electron Paramagnetic Resonance on Eu-doped BaX_2 57

1 Crystal field calculation . . . 58
2 Preliminary EPR investigations on Eu-doped BaI_2 . . . 63

7 ^{151}Eu-Mössbauer Spectroscopy on Eu-doped CaF_2, $BaCl_2$, and Glasses 67
1 Eu-doped CaF_2 . . . 67
1.1 CaF_2 doped with 0.1% Eu . . . 70
1.2 CaF_2 doped with 2% Eu . . . 78
1.3 CaF_2 doped with 2% Eu in a small magnetic field of 0.2 T . . . 78
1.4 CaF_2 doped with 2% Eu in a magnetic field of 6 T . . . 81
1.5 Discussion . . . 83
2 Eu-doped $BaCl_2$ . . . 86
3 Glass Ceramics . . . 87
4 Discussion . . . 92

8 Conclusion 95

A The Stevens operators O_k^q 97
1 The Stevens operators O_k^q . . . 97
2 Hyperfine matrix of the ground state . . . 100
3 Hyperfine matrix of the excited state . . . 109

B Transition probability 119

C Maple programm 125

Bibliography 135

Publications 139

Danksagung 141

1 Introduction

On a cold and grey November evening in 1895 W. C. RÖNTGEN discovered x-rays. In 1896 A. H. BECQUEREL discovered another type of ionizing radiation: γ-rays. Nowadays, x-ray and γ-ray radiography are very important methods in medical diagnostics, non-destructive testing and many fields of physical and chemical research. For all applications the detection of radiation intensity distribution is essential. An important tool used for the detection of ionizing radiation are x-ray scintillators which are common scintillators based on inorganic materials. Radiation detection with scintillators is based on the detection of scintillation light produced by ionizing radiation. Scintillation research has become very important during the last twenty years.

Europium (Eu)-activated fluorozirconate-based glass ceramics represent a novel class of x-ray scintillators [1, 2]. In contrast to common single crystal scintillators, glass ceramics can be manufactured easily in any shape or size. The scintillation in these glass ceramics is caused mainly by the typical $5d$-$4f$ transition of Eu(II), incorporated in $BaCl_2$ nanocrystals, which are formed in the glass matrix upon appropriate thermal processing. Since research on fast scintillators has become important during the last two decades, experiments with cerium (Ce)-activated fluorozirconate glass ceramics have been performed, showing that Ce is an interesting alternative [3, 4]. Ce-activated single crystals like $LaCl_3$ [5] or $LaBr_3$ [6] are known as fast scintillators with a high light output. A short scintillation decay time is necessary for fast timing or high rate counting applications.

In order to get a better understanding of the scintillation mechanism in Eu- or Ce-activated barium halide nanocrystals, an investigation of the processes in the corresponding bulk material is essential. This thesis studies the optical properties of Eu- and Ce-activated barium halides upon x-ray and γ-ray excitation. To get a closer look on the crystal structure and the crystal field of Eu-doped BaI_2, electron paramagnetic resonance spectroscopy measurements were carried out. Those EPR investigations on Eu-doped $BaCl_2$ and $BaBr_2$ have already been made by Wever and den Hartog [7] and Schweizer et al. [8], respectively.

Although the glass ceramics were doped with europium(II) fluoride (EuF_2) there is also a large fraction of Eu(III) in the glass. Most likely, the divalent Eu is converted to trivalent Eu during the melting process. To optimize the glass ceramics it is important to optimize the Eu^{2+}/Eu^{3+} ratio in favor of the Eu^{2+}. Mössbauer spectroscopy provides an excellent method to detect and to distinguish between di- and trivalent europium. In addition, the abundance ratio between the two valence states of europium can also be determined. For a better understanding of Mössbauer spectra exemplary measurements on Eu-doped CaF_2 single crystals were carried out.

It is already known from previous measurements [4, 9] that the main problem with doping fluorozirconate glass ceramics with trivalent Ce is to get the Ce into the nanocrystals. The valence state of Ce seems to be the problem. While in the case of Eu^{2+} a divalent rare-earth ion substitutes for a divalent barium in the nanocrystals, the Ce ion is trivalent. The idea is to add a monovalent ion for charge compensation. Potassium (K) was selected to be that ion.

A brief introduction to the physical and theoretical background of optical, electron paramagnetic resonance (EPR), and Mössbauer spectroscopical methods is given in chapter 2. Chapter 3 presents the results of the optical investigations on undoped, Eu-, and Ce-doped barium halides. It also gives a short overview of the most important characteristics of scintillators. For the solution of the problem with trivalent Ce-doped glass ceramics fluorozirconate base glass ceramics doped with Ce and those doped with Ce and K are investigated in chapter 4. The alternative dopants Sm and Mn are investigated for applications as fluorescence standard and scintillator. Chapter 5 gives a short introduction to fluorescence standards and summarizes the results of the Sm- and Mn-doped single crystals and glass ceramics. The EPR data of Eu-doped BaI_2 should yield more information about the crystal field and crystal structure and should help to understand the charge carrier process during the scintillation process. These EPR measurements of Eu-doped BaI_2 are shown in chapter 6. Furthermore, the crystal fields of the barium halides are calculated. Chapter 7 summarizes the Mössbauer investigation and results of Eu-doped CaF_2, Eu-doped $BaCl_2$, and Eu-doped fluorochlorozirconate glass. At last, all important results of the presented investigations are concluded in chapter 8.

2 Physical and theoretical background

The following chapter will only give a brief introduction to the methods. Further reading for each method is suggested in the corresponding section. Since in general three different kinds of spectroscopic methods were used (optical, electron paramagnetic resonance, and Mössbauer spectroscopy) the chapter is divided into three parts: one for each method. In the first part an introduction to the optical measurement methods will be given, followed by the electron paramagnetic resonance (EPR) and completed by the Mössbauer spectroscopy.

1 Optical Spectroscopy

The optical investigations were carried out with visible and ultraviolet (UV) light, x-rays, and γ-radiation. All these methods are based on the fact that materials absorb the energy of the exciting photons and emit some of the energy in the form of luminescent light. Since the luminescence light is characteristic of the dopant and its environment, information on the dopant (e.g. valence state or just the element) and the influence of the surrounding (single crystal or glass matrix) can be elucidated. The energy transfer leading to the conversion of energy from the exciting photon to the emission luminescence depends on the dopant and its surrounding.

1.1 Photo- and x-ray luminescence

The excitation source characterizes the luminescence. Luminescence excited by light and x-rays is called photoluminescence (PL) and x-ray excited luminescence (XL), respectively. If a spectrum is recorded after x-irradiation it is called afterglow. The PL, XL, and afterglow spectra were recorded using a 0.22 m double monochromator (Spex) in combination with a cooled photomultiplier (Hamamatsu R943-02) working in single-photon counting mode (HP 5370B Universal Time Interval Counter). Spectra were not corrected for sensitivity of the experimental setup. The x-ray irradiation was carried out with a mobile x-ray tube (Phillips MGC 01) using a tungsten anode at 60 kV and 15 mA. Figure 2.1 shows the experimental setup for the luminescence measurements.

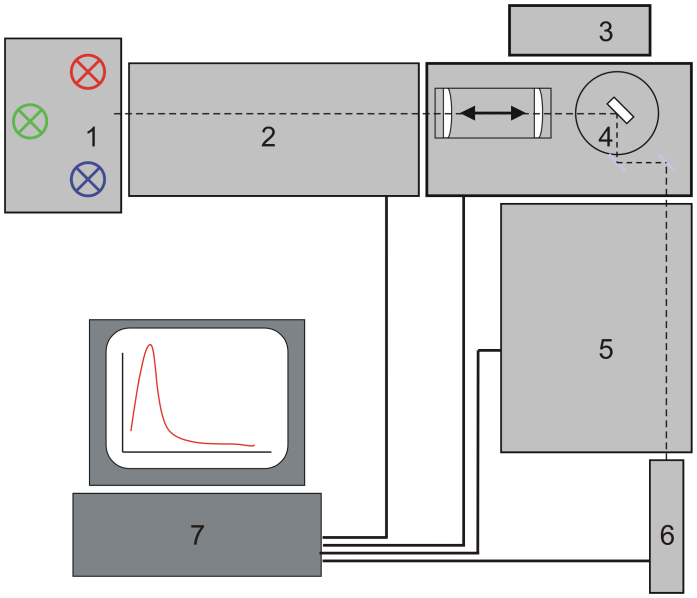

Figure 2.1: Experimental setup for luminescent measurement. Deuterium lamp, xenon lamp, and halogen lamp (1); monochromator (2); x-ray source (3); cryostat with lens system and sample chamber (4); monochromator (5); photomultiplier (6); computer (7).

1.2 Decay time measurements

Scintillation decay time measurements were performed at the Delft University of Technology. The spectra were recorded by two methods. The first is the single-photon counting technique described by Bollinger and Thomas [10]. For this method, scintillation decay time spectra were recorded at times up to 200 μs with XP2020Q PMTs, Ortec 934 constant fraction discriminators, Ortec 567 time-to-amplitude converter (TAC), and AD513A CAMAC analog-to-digital converter (ADC). To record decay time spectra at times longer than 200 μs, the multi-hit method descried by W. W. Moses [11] was used. The TAC and ADC in the single-photon counting technique were replaced by a Lecroy 4208 time-to-digital converter (TDC), which has a channel width of 1 ns. Using this method, the short decay component and its contribution to the total light yield are less accurately obtained than those using the single-photon counting technique.

1.3 γ Spectroscopy: Pulse height spectra

Pulse height spectra were obtained at the Delft University of Technology with a Hamamatsu R1791 photomultiplier tube (PMT) with a box-type dynode structure connected to a pre-amplifier and an Ortec 672 spectroscopy amplifier inside an M-Braun UNILAB dry box with a moisture content less than one part per million. The crystals were mounted directly onto the window of the PMT and covered with several Teflon layers to optimize the light collection. The photoelectron yield (LY_{phe} in photoelectrons per MeV) is obtained

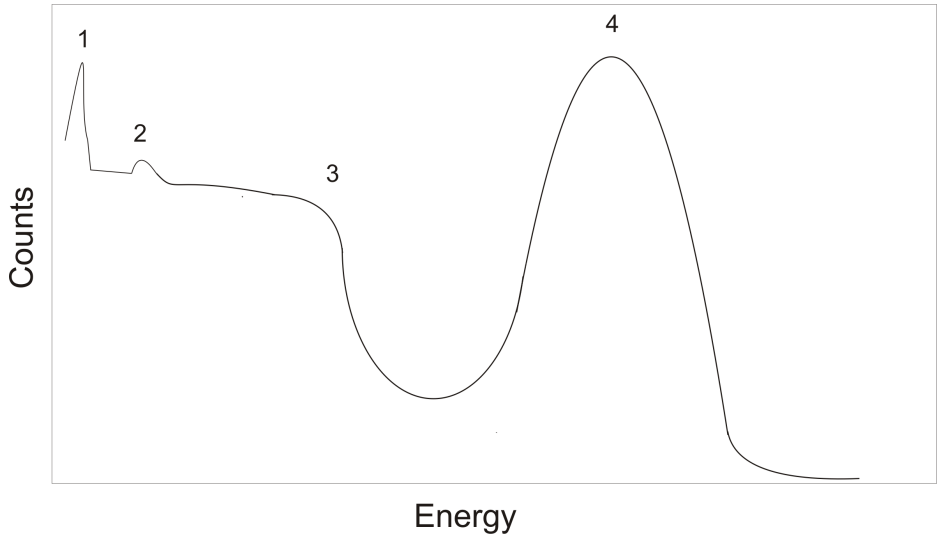

Figure 2.2: Theoretical pulse height spectra of a ^{137}Cs source. (1) Ba x-ray peak, (2) backscatter peak, (3) Compton edge, and (4) photopeak.

by comparing the peak position of the photopeak with that of the single-electron spectrum [12]. The absolute light yield, LY_{ph} in photons per MeV (ph/MeV), is derived from LY_{phe} as follows [13]:

$$LY_{ph} = (1 - R_{eff}) / (0.98 \cdot QE_{eff}) \cdot LY_{phe} \tag{2.1}$$

The effective quantum efficiency QE_{eff} of the PMT was obtained from the manufacturer, and the PMT effective reflectivity R_{eff} was measured. Both are averaged over the spectral profile of the γ-ray excited scintillation spectrum. The position and the energy resolution of the photopeak (full width at half maximum) was determined by fitting the photopeak with a Gaussian curve. Figure 2.2 shows a theoretical pulse height spectrum. The leftmost peak (1) is caused by the Ba x-rays which are emitted in the ^{137}Cs decay. The backscatter peak (2) arises from scattering of the γ-rays from the PMT and materials outside the system back into the scintillation crystal. Beside the photopeak (4) the spectrum shows the Compton continuum from the Compton edge (3) down to zero energy.

2 Electron Paramagnetic Resonance (EPR)

A brief introduction to Electron paramagnetic resonance (EPR) is given in the following text. Detailed information can be found in [14, 15].

The EPR measurements were performed with a computer-controlled, custom-built X-band EPR spectrometer. The EPR spectra were evaluated with the "Visual EPR" programme package using exact diagonalization procedures [16, 17].

EPR spectroscopy is based on the splitting of the energy levels of an electron in an exter-

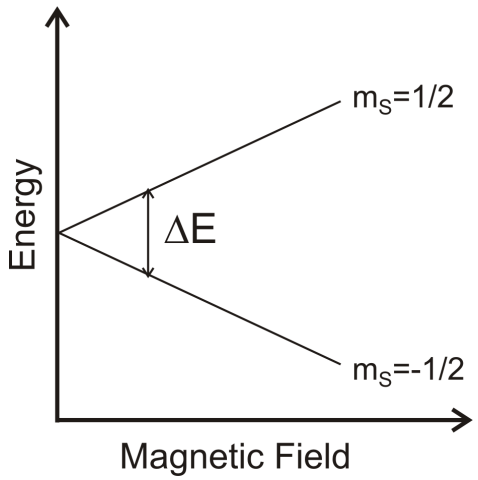

Figure 2.3: Energy difference of the magnetic quantum number m_S versus an external magnetic field.

nal magnetic field $\overrightarrow{B}$. This effect is called the Zeeman effect. The electron can only have discrete orientations. The quantum mechanical description of the electron spin yields to

$$\overrightarrow{\mu}_{spin} = g\,\overrightarrow{S}. \tag{2.2}$$

with $\overrightarrow{\mu}_{spin}$ the magnetic moment of the electron, g the g-factor and $\overrightarrow{S}$ is the spin quantum number. A free electron has two possible orientations of the spin, i.e. $m_S = +1/2$ and $m_S = -1/2$. These two spin states are energetically split by an external magnetic field (Figure 2.3). The energy difference is is given by:

$$\Delta E = g_e \mu_B B_0 \tag{2.3}$$

with g_e the g-value (which is 2.0023 for the free electron), μ_B the Bohr magneton, and B_0 the external magnetic field. The spin of an electron can be changed by the use of an electromagnetic alternating field. The change of the spins requires the energy difference ΔE and additionally the change of the magnetic quantum number $\Delta m_S = \pm 1$.

The change of the spin leads to a resonant absorption which can be measured. Usually for the electromagnetic alternating field a microwave field in the range of 9-10 GHz (X-band) is used. The interaction between the spin and the orbital moment leads to a change of the g-value. The complete equation of the energy is given by the Spin Hamilton [18]:

$$\begin{aligned}\mathscr{H} &= \mathscr{H}_{EZ} + \mathscr{H}_{FS} + \mathscr{H}_{HF} + \mathscr{H}_{NZ} + \mathscr{H}_{Q} \\ &= \underbrace{\mu_B \overrightarrow{S}\,\underline{\underline{g}} B_0}_{\text{electron Zeeman}} + \underbrace{\overrightarrow{S}\,\underline{\underline{D}}\,\overrightarrow{S}}_{\text{fine structure}} + \underbrace{\overrightarrow{I}\,\underline{\underline{A}}\,\overrightarrow{S}}_{\text{hyperfine}} + \underbrace{g_n \mu_n \overrightarrow{I} B_0}_{\text{nuclear Zeeman}} + \underbrace{\overrightarrow{I}\,\underline{\underline{Q}}\,\overrightarrow{I}}_{\text{nuclear quadrupole}}\end{aligned}$$

with $\underline{\underline{g}}$, $\underline{\underline{D}}$, $\underline{\underline{A}}$ and $\underline{\underline{Q}}$ symmetrical tensors in three-dimensional space.

In Figure 2.4 the complete splitting and the influence of the hyperfine and nuclear Zeeman tensor is shown.

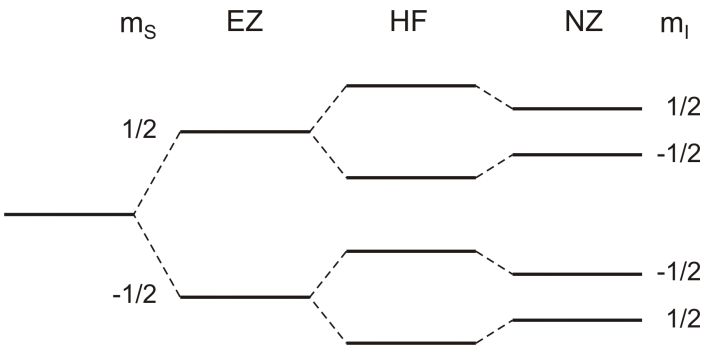

Figure 2.4: Complete spliting of the energy levels in an external magnetic field. EZ is the splitting of the electron spin, HF the splitting of the hyperfine interaction and NZ is the splitting of the nuclear Zeeman interaction. m_S and m_I are the magnetic quantum numbers of the electron and the nucleus, respectively.

3 Mössbauer Spectroscopy

Mössbauer spectroscopy is a recoil-free γ-ray spectroscopy. It is named after its inventor RUDOLF MÖSSBAUER, who received the Nobel prize for his discovery in 1961. Mössbauer spectroscopy is an important technique to obtain information on the microscopic level. The environment and the state of a nucleus can be studied. A nucleus is very sensitive to electronic and magnetic changes in its surrounding area. A brief introduction to the principles of Mössbauer-spectroscopy is given in the following section. Detailed descriptions can be found in [19, 20].

3.1 Mössbauer Effect

A nucleus in an excited state can go back to its ground state by the emission of a γ-quantum. This γ-quantum can be absorbed by an other nucleus of the same isotope. This process requires that the energy difference of the excited and ground state of the emitter and absorber nucleus match exactly.

Unfortunately, a free nucleus is subject to a recoil during the emission of a γ-quantum due to the conservation of momentum. The energy of the emitted γ-quantum is lowered by the recoil energy E_R. The recoil energy is given by:

$$E_R = \frac{E_\gamma^2}{2mc^2} \tag{2.4}$$

with m the mass of the recoil system: a free atom or a crystal. The same energy loss occurs once again during the absorption. The energy loss of the γ-quantum is $2E_R$ in total.

Because of these energy losses an emitted γ-quantum cannot be absorbed by a second nucleus of the same isotope. The energy no longer matches the transition energy of the excited

state of the nucleus. To achieve the resonance a recoil-free emission and absorption is necessary.

In 1957 RUDOLF MÖSSBAUER discovered that recoil-free emission and absorption of the γ-quantum can take place if the emitting and absorbing nuclei are incorporated into a host lattice. The momentum is transferred to the whole lattice. Due to the relatively huge mass of the host lattice the energy transfer is very low. In a classical description m in equation 2.4 goes to infinity and with this the recoil energy E_R goes to zero. In a quantum mechanical description the possibility of a recoil-free emission or absorption lies in the quantum nature of the lattice vibrations. The γ-quantum can loose energy only to phonons. The phonon energies of the lattice vibrations are quantized in values of $\hbar\omega$, i.e. the lattice can only have the energy 0, $\hbar\omega$, $2\hbar\omega$,.... On the Debye model there is a spectrum of frequencies ω up to a maximum cut-off frequency ω_D. So if the recoil energy E_R is less than $\hbar\omega_D$ the lattice can not absorb the recoil energy, but the excitation of phonons at lower frequencies ($\omega < \omega_D$) is possible. This involves the excitation of a number of atoms together, so that the recoil energy to be absorbed is now smaller. The probability of recoilless emission on absorption is given by:

$$f = \exp(-k^2 < x^2 >) \tag{2.5}$$

where $k = E_0/\hbar c$ is the wave vector of the radiation and x^2 is the mean square deviation of an atom during the lattice oscillation. f is the so-called Debye-Waller-factor. On the Debye model $< x^2 >$ is temperature dependent. The Debye-Waller-factor gives the probability of a recoilless or absorption. f as a function of temperature is given by:

$$f(T) = \exp\left(-\frac{3E_r}{2k_B\theta_D}(1 + 4((\frac{T}{\theta_D})^2 \cdot \int_0^{T/\theta_D} \frac{x}{e^x - 1}dx))\right) \tag{2.6}$$

where E_r is the recoil energy of the Mössbauer transition (E_r for ^{151}Eu is $1.665{\cdot}10^{-3}$ eV), k_b is the Boltzmann constant and θ_D is the Debye temperature. Even at 0 K the Debye-Waller-factor is less than 1. For $T \ll \theta_D$ the following approximation applies:

$$f(T) \approx \exp\left(-\frac{3E_r}{2k_B\theta_D}(1 + \frac{2\pi^2}{3}(\frac{T}{\theta_D})^2)\right) \tag{2.7}$$

For $T \geq \frac{\theta_D}{2}$ the following approximation applies:

$$f(T) \approx \exp\left(-\frac{6E_rT}{k_B\theta_D^2}\right) \tag{2.8}$$

3.2 Mössbauer Isotope ^{151}Eu

Eu has two naturally occurring isotopes, ^{151}Eu (47.82 %) and ^{153}Eu (52.18 %). Mössbauer isotopes must have very low lying excited states and a long lifetime for the decay of the excited state. These criteria exclude some isotopes. Because of long lifetime (141 ns) and the resulting its small linewidth (4.7 neV) and the small γ-energy (14.4 eV), respectively,

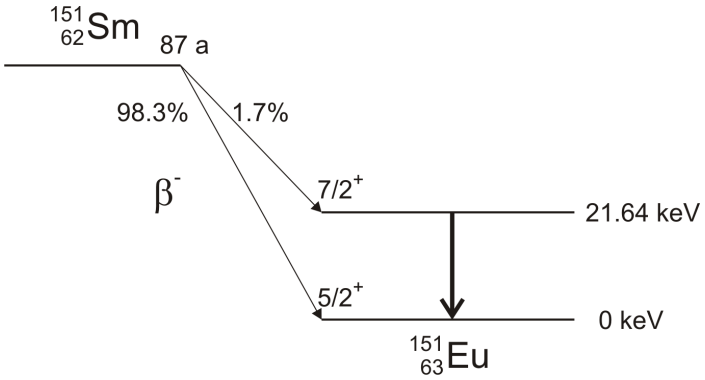

Figure 2.5: Nuclear decay scheme for ^{151}Sm and ^{151}Eu.

^{57}Fe is the most popular Mössbauer isotope. The isotope applied in this thesis is ^{151}Eu, which is the most used isotope of the rare-earth elements.

The Mössbauer source used for ^{151}Eu Mössbauer spectroscopy is ^{151}Sm. Figure 2.5 shows the decay scheme for ^{151}Sm and ^{151}Eu. The half-life of ^{151}Sm with 87 years is very long. Two different β^--decays occur in the ^{151}Sm isotope. ^{151}Sm goes with a probability of 98.3% to the ground state of ^{151}Eu. Only 1.7% of the ^{151}Sm isotope decay into the excited state of ^{151}Eu. The 21.64 keV transition from the excited to the ground state of ^{151}Eu has a lifetime of 14 ns and a resulting linewidth of 47 neV.

3.3 Hyperfine Interactions

There are three different kinds of interactions between the nucleus and the surrounding electrons that can be observed in a Mössbauer spectrum: the electric monopole, the electric quadrupole, and the magnetic dipole hyperfine interaction.

Electric monopole interaction: Isomer Shift

The isomer shift is the electric monopole interaction between the nucleus and the surrounding electron shell. The overlapping of charge density distribution of s-electrons with the nucleus causes a shift of the energy levels of the nucleus. The isomer shift is a good index for the valence state of the isotope. The isomer shift is given by:

$$S_{I.S.} = \frac{2\pi eZ}{3}(\rho_A(0) - \rho_S(0)) \cdot \Delta < r^2 > \tag{2.9}$$

where Z is the atomic number, $\rho_A(0)$ and $\rho_S(0)$ are the s-electron density at the absorber nuclei and the source nuclei, and

$$\Delta < r^2 > = < r_e^2 > - < r_g^2 >$$

is the difference between the nuclear radii of the ground and excited states.

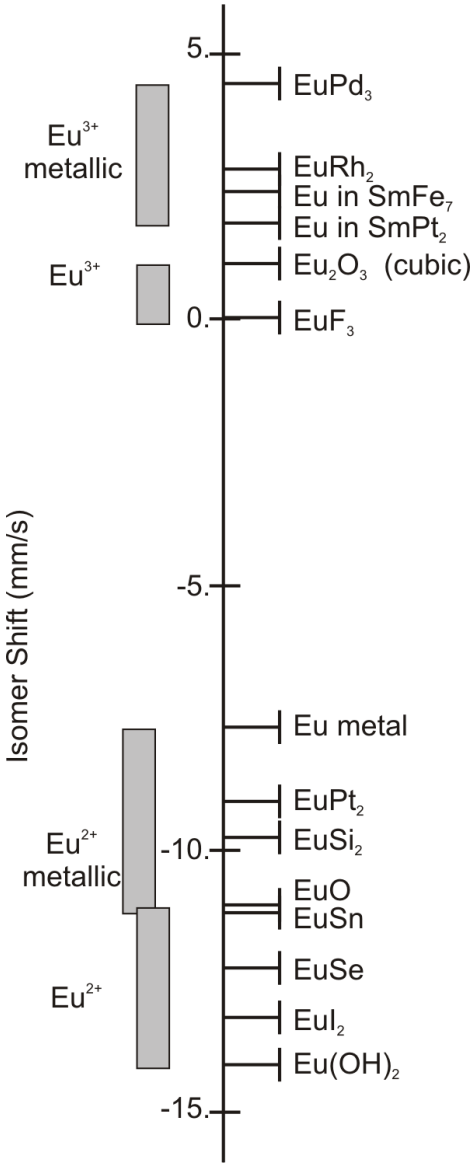

Figure 2.6: Plot of isomer shifts (adapted from [21]) for selected Eu compounds measured with the 21.64 keV resonance in ^{151}Eu. The electron density increases from bottom to top.

Eu^{3+} compounds exhibit isomer shifts between 0 and +3 mm/s, those of non-metallic Eu^{2+} compounds are between -11 and -14 mm/s (Figure 2.6). The main reason for the large difference in isomer shifts of about 12 mm/s between divalent and trivalent Eu-compounds lies in the shielding effect of the additional $4f$ electron in Eu^{2+} compounds. Other effects like ionicity or covalence are less pronounced (see Figure 2.6) but clearly resolved due to the large value of $\Delta < r^2 >= 18.5$ fm^2 [21] of the ^{151}Eu-resonance, being one the largest for the rare-earth Mössbauer resonances. The Eu^{2+}-doped samples investigates in this thesis exhibit isomer shifts around -13.5 mm/s.

Electric Quadrupole Interaction

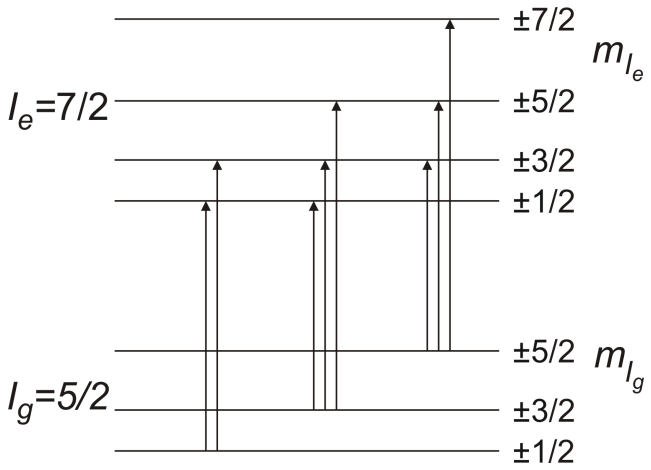

Figure 2.7: Nuclear energy levels for ^{151}Eu in presence of a quadrupole interaction. The arrows denote the allowed transitions.

Most nuclei are not spherically symmetric and have a quadrupole moment Q. For nuclear spin states lager than 1/2 in a non-cubic crystalline surrounding a quadrupole interaction is observable. When the surrounding charge density produces an electric field gradient (EFG) this interacts with the quadrupole moment which splits the nuclear levels. The ground and excited nuclear states of europium have nuclear spins of $I = \frac{5}{2}$ and $I = \frac{7}{2}$, respectively. Due to the quadrupole interaction a level is split into $(I + \frac{1}{2})$ sublevels. The nuclear state energies are given by:

$$E_{m_I} = \frac{eQV_{zz}}{4} \cdot \frac{3m_I^2 - I(I+1)}{I(2I-1)} \sqrt{1 + \frac{\eta^2}{3}} \tag{2.10}$$

where Q is the quadrupole moment of the nucleus, V_{zz} is the z-component of the EFG, and η is an asymmetry parameter given by:

$$\eta = \frac{V_{xx} - V_{yy}}{V_{zz}} \tag{2.11}$$

The quadrupole moment Q_e of the excited state is 1.34 time Q_g of the ground state. With this the transition energies ΔE_{m_I} can be calculated by:

$$\Delta E_{m_I} = \frac{eQV_{zz}}{4} \sqrt{1 + \frac{\eta^2}{3}} \left\{ \frac{1.34(3m_{I_e}^2 - I_e(I_e+1))}{I_e(2I_e-1)} - \frac{3m_{I_g}^2 - I_g(I_g+1)}{I_g(2I_g-1)} \right\} \tag{2.12}$$

Transitions with $\Delta m_I = 0, \pm 1$ are allowed. Figure 2.7 shows the nuclear energy levels of ^{151}Eu and the eight allowed magnetic dipole transitions.

Magnetic Dipole Hyperfine Interaction

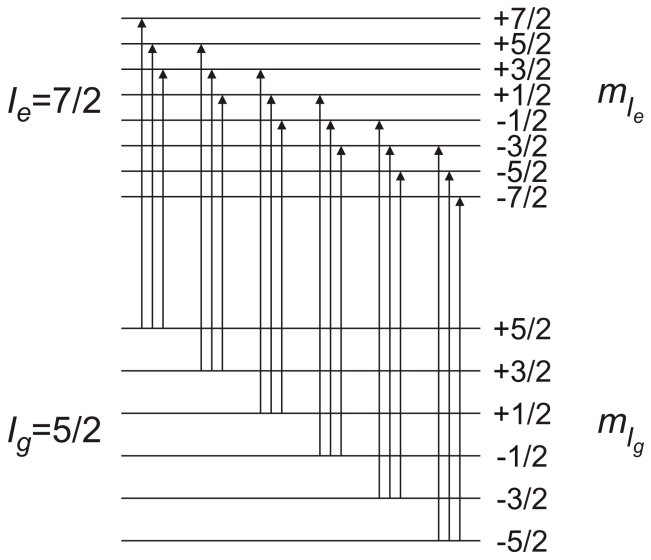

Figure 2.8: Nuclear energy levels for ^{151}Eu in presence of a magnetic hyperfine interaction. The arrows denote the allowed transitions.

If the nucleus has a magnetic dipole moment μ_I a magnetic hyperfine splitting occurs in the presence of a magnetic corefield B_c due to the atom´s own electrons, here the $4f^7$ electrons produce the B_c. The level of the nucleus is split into $2I + 1$ sublevels. The selection rule of these transition is $\Delta m_I = 0, \pm 1$. The nuclear energy levels and the eighteen transitions are shown in Fig. 2.8. The size of the splitting is an index for the magnetic field at the nucleus. The energy levels are given by:

$$E_m = -g_n \mu_n m_I B_c \tag{2.13}$$

where g_n is the nuclear g-factor and μ_n is the nuclear magneton. This effect is analog to the Zeeman-effect and is called nuclear-Zeeman-effect.

3 Barium halide scintillators for x-ray and γ-ray detections

Since the main focus in this chapter is on x- and γ-ray scintillators an overview of the requirements, properties, and applications of scintillators are given in the following section.

The radiation detection with scintillators is based on the detection of the scintillation light produced by the ionizing radiation. The ionizing radiation interacts with the scintillator material. There are three main interactions between the radiation and the material: The photoelectric effect, the Compton effect and pair production.

- During the photoelectric effect the x- or γ-ray (photon) transfers all its energy to an electron. The electron is liberated from the atom and its kinetic energy is the photon energy minus the binding energy.
- In the case of the Compton effect a photon scatters from a weakly bounded electron. A part of the energy of the photon is transferred to the electron.
- If the energy of a photon is larger than 1.022 MeV the photon can be converted into an electron-positron pair: this event is called pair production.

1 Characteristics of scintillators

Scintillators are usually characterized by the following properties: **energy resolution**, **light yield**, and **scintillation decay time**.

The energy resolution gives the relationship between the light output and the energy of the penetrating γ-quantum. Energy resolution is determined by the full width at half maximum (FWHM) divided by the centroid position of the photopeak of a pulse hight spectra. This ratio is normally given in percent. The smaller the values (corresponding to narrow peaks) the better the energy resolution.

The light yield is the fast part of the generated light after the absorption of an energetic photon (x- or γ-quantum) and is obtained from pulse height spectra. The light yield is the coef-

Crystal	density (g/cm^3)	light yield (ph/MeV)	emission wavelength λ (nm)	decay time τ(ns)	Ref.
NaI:Tl	3.67	40,000	415	230	[22, 23]
CsI:Tl	4.51	52,000	540	10^3	[24]
CWO	7.90	28,000	495	10^4	[23, 25]
BGO	7.31	8,900	480	300	[23, 26, 27]

Table 3.1: Properties of common inorganic scintillators.

ficient of conversion of ionizing radiation into light energy, it is given in photons per MeV. A fast scintillation decay time is necessary for fast timing or high count rate applications. Integrated x-ray excited luminescence spectra provide information on the integral scintillation efficiency.

The scintillation decay time is the time required for scintillation emission to decrease to $1/e$ of its maximum.

Beside these properties the effective Z (Z_{eff})is another important characteristic. The formula for Z_{eff}, the effective atomic number, is given by :

$$Z_{eff} = \sqrt[n]{f_1 \cdot (Z_1)^n + f_2 \cdot (Z_2)^n + f_3 \cdot (Z_3)^n + \dots} \tag{3.1}$$

where f_n is the fraction of the total number of electrons associated with each element (by weight of element i with atomic number Z in the chemical formula), and Z_1 is the atomic number of each element, n is a value between 2 and 4 depending on the energy of the radiation. Effective atomic number is important for predicting how x-rays interact with a substance, as certain types of x-ray interactions depend on the atomic number. Z_{eff} is similar to atomic number but is used for compounds. The effective atomic number is calculated by taking the fractional proportion of each atom in the compound and multiplying that by the atomic number of the atom.

An overview of important physical and luminescence properties of the common inorganic scintillators NaI:Tl, CsI:Tl, $CdWO_4$ (CWO), and Bi_4GeO_4(BGO) are given in Table 3.1.

2 Crystal structure

In the following chapter the scintillation properties of twelve different crystals were investigated. The crystals are listed in Table 3.2. All investigated crystals have a common crystal

Host lattice	Dopant	Doping level
$BaCl_2$	-	-
$BaCl_2$	Eu	1000 ppm
$BaCl_2$	Ce	1000 ppm
$BaCl_2$	Ce	10000 ppm
	K	10000 ppm
$BaBr_2$	-	-
$BaBr_2$	Eu	1000 ppm
$BaBr_2$	Ce	1000 ppm
$BaBr_2$	Ce	1000 ppm
	K	1000 ppm
$BaBr_2$	Ce	10000 ppm
	K	10000 ppm
BaI_2	-	-
BaI_2	Eu	1000 ppm
BaI_2	Ce	1000 ppm

Table 3.2: List of investigated crystals.

crystal	a (Å)	b (Å)	c (Å)	anion radius (Å)	density (g/cm^3)	effective Z
$BaCl_2$	7.865	4.731	9.421	1.81	3.888	49.8
$BaBr_2$	8.276	4.956	9.919	1.96	4.781	47.8
BaI_2	8.922	5.304	10.695	2.20	5.15	54.1

Table 3.3: Lattice parameters of BaX_2 [28] and anion ionic radii of the corresponding halide ion X, density [29] and effective Z [30] (for energies between 100 keV and 1 MeV).

structure. The stable phase of BaX_2 crystals at room temperature (RT) has the orthorhombic $PbCl_2$ structure characterized by the space group D_{2h}^{16} (*Pnma*) [28]. Figure 3.1 shows the crystal structure of orthorhombic BaX_2 as projections in different crystal planes.

While all three host lattices have the same crystal structure they differ in lattice parameters. The lattice parameters of the crystals are summarized in Table 3.3.

The RE dopants Eu^{2+} and Ce^{3+} are substituting for Ba^{2+} having nine halide ions as close neighbours at slightly varying distances. The lattice parameters have a direct effect on the distances between the Ba ion and the halide ions. With increasing lattice parameters the distance increases. Figure 3.2 shows the different distances between Ba and the halide ion for the three different crystals.

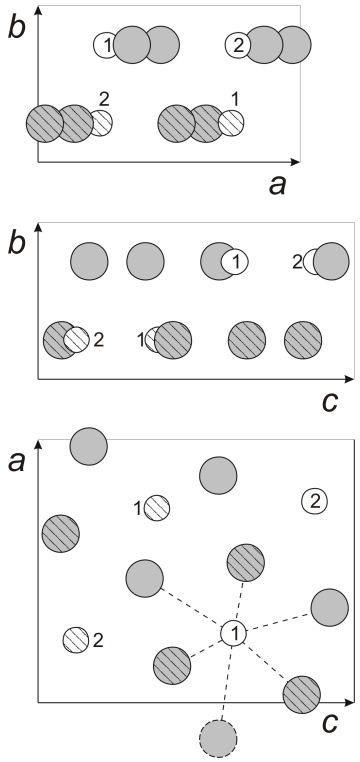

Figure 3.1: Lattice structure of the orthorhombic BaX_2 structure, from top to bottom, projected on the *ba*, *bc*, and *ac* symmetry plane. The small white circles denote the Ba^{2+} ions. The large grey circles denote the X^- ions, the hatched grey circles lie in a different mirror plane than the non-hatched ones.

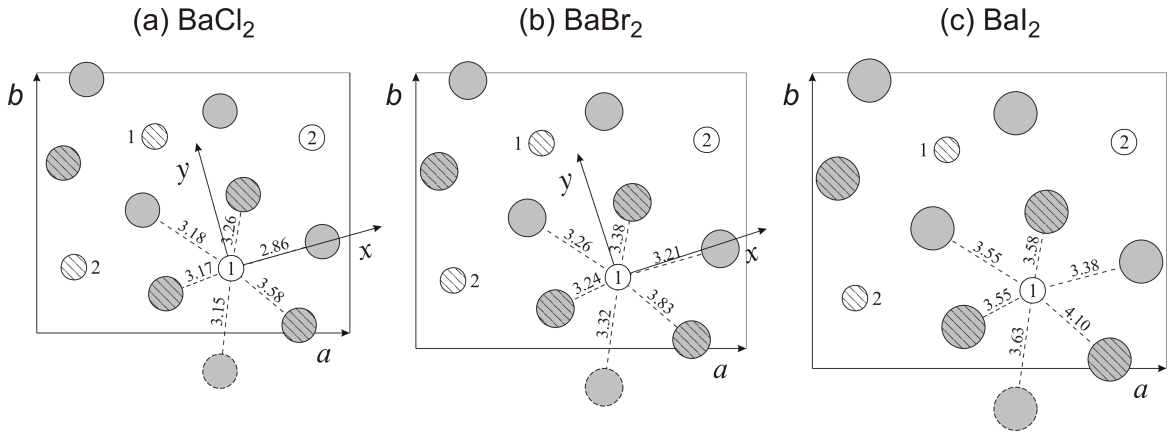

Figure 3.2: Details of the lattice structure of, from top to bottom, $BaCl_2$, $BaBr_2$ and BaI_2 as a projection on the *ac* crystal plane. The small white circles and the large grey circles denote the Ba^{2+} ions and the halide ions, respectively. The ions discerned by hatched circles lie in a different *ac*-type mirror plane than the non-hatched ones. The numbers denote the distance between the Ba ion and the corresponding halide ion in Å.

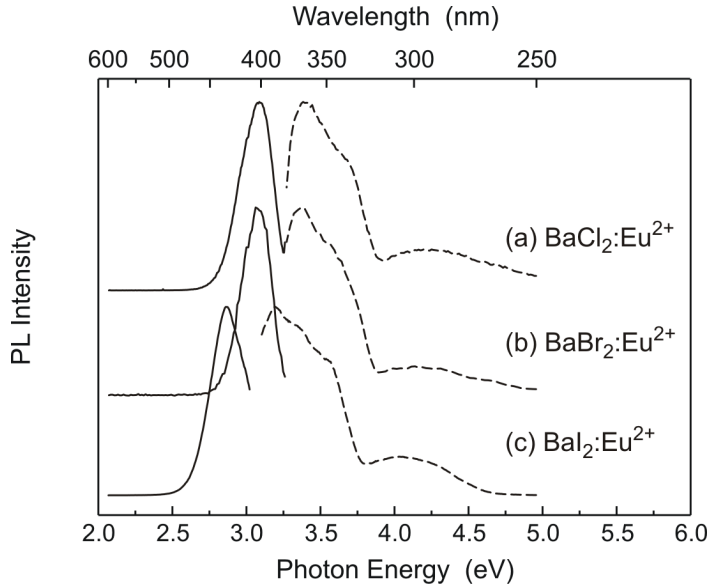

Figure 3.3: PL (solid curves) and PL excitation (dashed curves) spectra of (a) $BaCl_2$:Eu^{2+}, (b) $BaBr_2$:Eu^{2+}, and (c) BaI_2:Eu^{2+}. The PL was excited at 370 ($BaCl_2$/$BaBr_2$) and 385 nm (BaI_2); the PL excitation detected at 402 ($BaCl_2$), 404 ($BaBr_2$), and 425 nm (BaI_2).

3 Sample preparation

Single crystals of BaX_2 (X = Cl, Br, I) were grown at the Paderborn crystal growth laboratory using the Bridgman method with a quartz ampoule under an SiX_4 atmosphere from BaX_2 powder and 1000 molar ppm of EuX_2 or CeX_3, respectively. The usual technique was completed by slow cooling through the cubic-orthorhombic phase transition near 920°C ($BaCl_2$) [28] and 800°C ($BaBr_2$) [31], respectively. Prior to crystal growth the BaX_2 powder was dried in a vacuum with subsequent melting in a SiX_4 atmosphere to reduce oxygen contamination. However, the silicon treatment did not work for the BaI_2 powder.

4 Photoluminescence (PL)

Figure 3.3 shows the PL and PL excitation spectra of Eu-doped $BaCl_2$, $BaBr_2$, and BaI_2, respectively. The Eu^{2+} emission shifts from 402 nm for $BaCl_2$ to 404 nm for $BaBr_2$ and 425 nm for BaI_2. Also a shift of the excitation wavelength can be observed.

PL and PL excitation spectra of the Ce-doped barium halides are shown in Fig. 3.4. The PL curve of $BaCl_2$ and $BaBr_2$ (site A) have the typical double-band shape of Ce-luminescence. The doublet occurs as a result of the $4f^1$ ground-state splitting caused by spin-orbit coupling. For $BaBr_2$ (site B), the doublet is not resolved. This PL has been suggested to be due to oxygen contamination, e.g. to some charge-compensated Ce^{3+}-O^{2-} pairs [36]. The structure of the PL excitation spectra is formed by the split $5d^1$ excited state which has up to five levels depending on the crystal field. The doublet of $BaCl_2$ is at 349 and 373 nm with

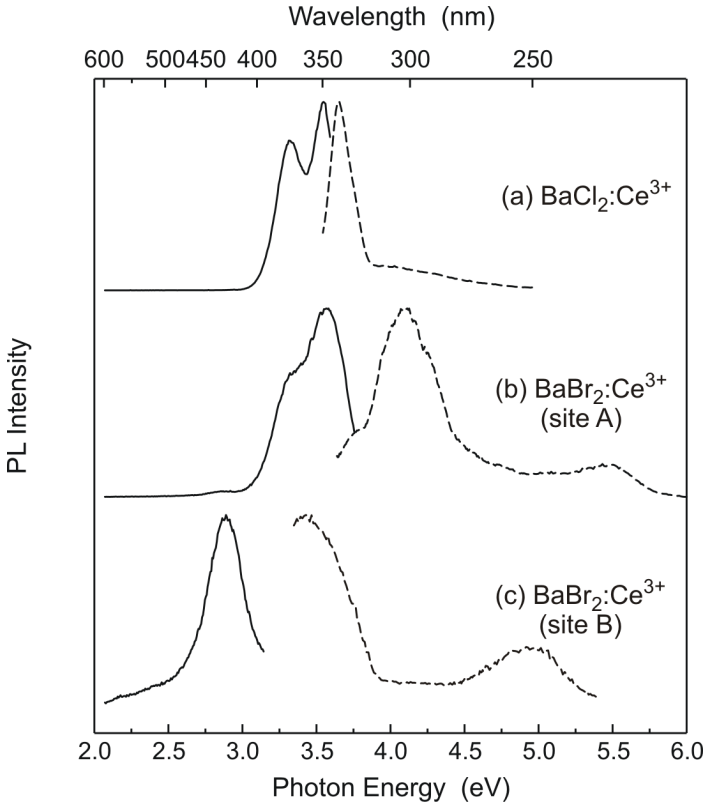

Figure 3.4: PL (solid curves) and PL excitation (dashed curves) spectra of (a) $BaCl_2$:Ce^{3+}, (b) $BaBr_2$:Ce^{3+} - site A, and $BaBr_2$:Ce^{3+} - site B. The PL was excited at 340 ($BaCl_2$), 300 ($BaBr_2$ - site A), and 350 nm ($BaBr_2$ - site B); the PL excitation detected at 373 nm ($BaCl_2$), 370 nm ($BaBr_2$ - site A), and 420 nm ($BaBr_2$ - site B).

its excitation maximum at 339 nm. In $BaBr_2$:Ce^{3+}, two different Ce sites exist. The doublet shifts to 345 and 370 nm (site A) and 420 nm (site B), respectively. The maximum of the corresponding excitation spectrum is at 300 nm (site A) and 350 nm (site B). Ce-doped BaI_2 shows no recordable PL signal. The Eu and Ce emission wavelengths are shown in Table 3.4.

dopant	host lattice	λ (nm)	Ref.
Eu^{2+}	$BaCl_2$	402	[32], [33]
	$BaBr_2$	404	[32], [33]
	BaI_2	425	[34]
Ce^{3+}	$BaCl_2$	349, 373	[35]
	$BaBr_2$ (site A)	345, 370	[36]
	$BaBe_2$ (site B)	420	[36]

Table 3.4: Emission wavelengths for UV excitation of the Eu- and Ce-luminescence in a barium halide host lattice.

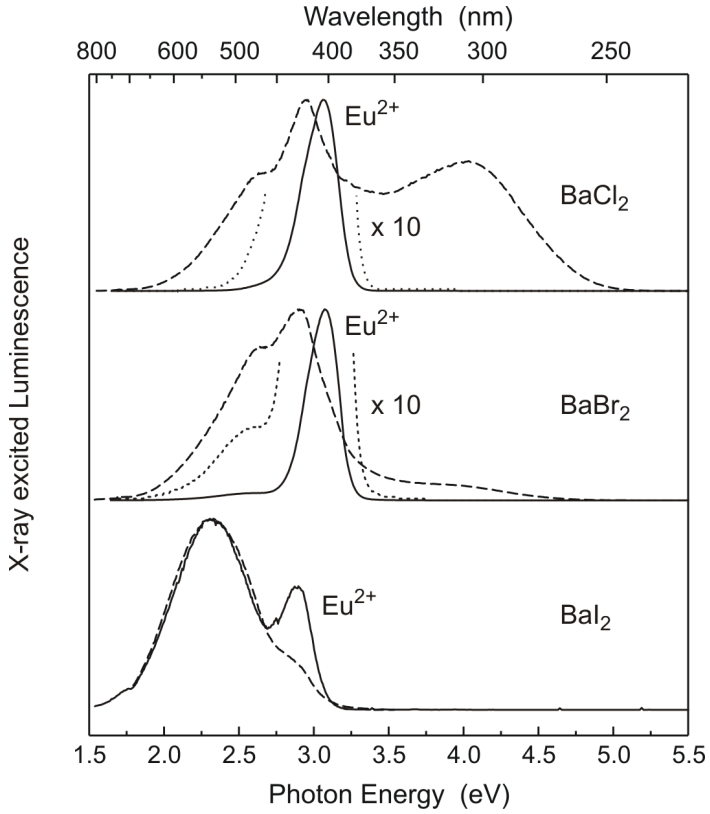

Figure 3.5: Normalized x-ray excited luminescence spectra of undoped (dashed curves) and Eu-doped (solid curves) barium halides. Parts of the spectra of the Eu-doped samples (dotted curves) are blown up x10 times as indicated. All spectra were recorded at RT.

5 X-ray excited luminescence (XL)

Figure 3.5 shows the normalized XL spectra of undoped and Eu-doped $BaCl_2$, $BaBr_2$, and BaI_2. The XL of undoped $BaCl_2$ shows a broad band at about 300 nm and a doublepeak structured band between 380 and 600 nm with maxima at 420 and 475 nm. The ultraviolet XL band at about 300 nm can only be seen in undoped $BaCl_2$ but not in any of the other samples. The XL of undoped $BaBr_2$ shows a similar double-peak structured band as found in undoped $BaCl_2$ with peak positions at 425 and 475 nm. However, the intensity ratio of the 425 to the 475 nm band has changed in favor of the longer wavelength. In undoped BaI_2 a broad XL band at about 530 nm with a small shoulder at about 430 nm can be found. The XL spectra of the Eu-doped $BaCl_2$ and $BaBr_2$ do not show any of the features described above but single bands at 402 and 404 nm, respectively. This band is due to the typical $5d$-$4f$ transition of Eu^{2+}. The 404 nm band in $BaBr_2$ shows a small shoulder at about 480 nm. The Eu^{2+} emission is further shifted to longer wavelengths in Eu-doped BaI_2, where it is seen as a small peak at about 425 nm. The XL of Eu-doped BaI_2 is dominated by the broadband at 530 nm, which also appeared in undoped BaI_2. The most intense XL peak occurred for the Eu^{2+} $5d$-$4f$ transition in $BaBr_2$ followed by $BaCl_2$. The Eu^{2+} emission in BaI_2 is very weak.

Figure 3.6 shows the normalized XL spectra of Ce-doped BaX_2(solid curves) and Ce- and K-co-doped $BaCl_2$ and $BaBr_2$ (dashed and dotted curves). The XL curves of Ce-doped $BaCl_2$ (Figure 3.6a, solid curve) and $BaBr_2$ (Figure 3.6b and c, solid curves) have the typical doublet for Ce luminescence. The double band shape is a result of the $4f$ ground state splitting, caused by the spin-orbit coupling. The doublet of $BaCl_2$ is at 349 and 373 nm. For $BaBr_2$ the doublet shifts to 345 and 370 nm. In the case of BaI_2 (Figure 3.6d, solid curve) no Ce luminescence can be observed. The increase of an additional band from Cl via Br to I can be seen. While in the $BaCl_2$ host lattice the additional luminescence bands at 420 and 480 nm can only be observed in the expanded spectrum, in $BaBr_2$ they are almost as intense as the Ce-doublet. For BaI_2 only a broad band at 550 nm can be seen. The additional bands agree with those of the corresponding undoped crystals (Figure 3.5, dashed curves). Besides the bands at 420 and 480 nm the expanded spectrum of $BaCl_2$:Ce^{3+} (0.1%) shows a peak at 305 nm. This corresponds to a band observed in undoped $BaCl_2$ and is assumed to be a self-trapped exciton (STE).

The spectrum of $BaCl_2$:Ce^{3+}, K^+ (1%) (Figure 3.6a, dashed curve) shows the same characteristic Ce-doublet as found in the sample without potassium, but slightly (less than 5 nm) shifted to longer wavelength; the linewidth is slightly smaller. In the case of $BaBr_2$ doped with 0.1% $CeBr_3$ and 0.1% KBr (Figure 3.6b, dotted curve), the ratio between the Ce-doublet and the additional luminescence bands at 420 and 480 nm has changed in favour of the Ce-doublet. The intensity of the Ce-doublet in 0.1% Ce- and 0.1% K co-doped $BaBr_2$ is almost twice that of the corresponding 0.1% Ce-doped crystal. In $BaBr_2$:Ce^{3+}, K^+ (1%) (Figure 3.6c, dashed curve) the Ce-doublet is barely resolved and shifted by more than 30 nm to 375 and 410 nm. The additional bands at 420 and 480 nm are very weak and hardly noticeable.

For a rating of the scintillation properties with regard to integral x-ray scintillation efficiency the barium halide single crystals were compared to the common scintillator $CdWO_4$. The measurements were made using the same parameters for all crystals. The area under the XL curve is calculated and compared to that of a $CdWO_4$ reference sample with a light yield of 28,000 ph/MeV [37]. The integral x-ray scintillation efficiencies are given in Table 3.5. The results of the Eu-doped samples and Ce-doped $BaCl_2$ and $BaBr_2$ have already been presented in [34]. The value for BaI_2:Eu^{2+} presented in Table 3.5 is slightly larger than in [34].

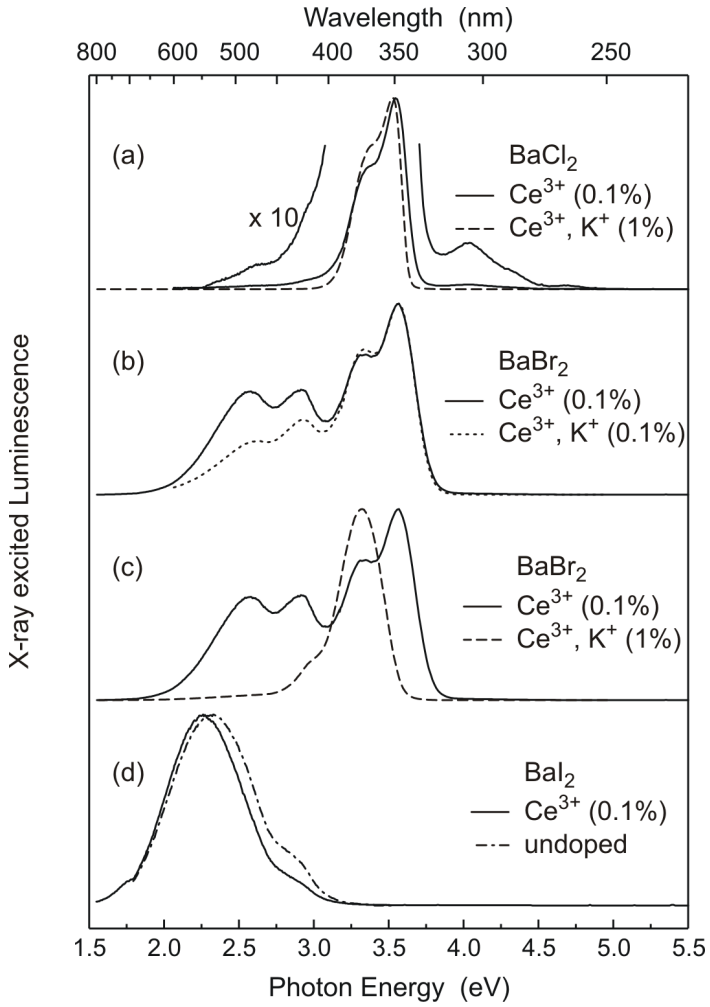

Figure 3.6: Normalized x-ray excited luminescence spectra of (a) $BaCl_2$:Ce^{3+} (0.1%) and $BaCl_2$:Ce^{3+}, K^+ (1%), (b) $BaBr_2$:Ce^{3+} (0.1%) and $BaBr_2$:Ce^{3+}, K^+ (0.1%), (c) $BaBr_2$:Ce^{3+} (0.1%) and $BaBr_2$:Ce^{3+}, K^+ (1%), and (d) BaI_2:Ce^{3+} (0.1%). Parts of the spectrum of 0.1% Ce-doped $BaCl_2$ are expanded as indicated.

Crystal	Integral x-ray scintillation efficiency with respect to $CdWO_4$ (photons/MeV)	XL-to-afterglow ratio (after 3 sec)
$BaCl_2$	4,500 $\pm$ 500	20 % at 420 nm 25 % at 475 nm
$BaCl_2$:Eu^{2+}	19,000 $\pm$ 1,900	0.2 % at 402 nm
$BaCl_2$:Ce^{3+} (0.1 %)	4,800 $\pm$ 480	2 % at 305 nm 8 % at 350 / 370 nm 5 % at 420 / 480 nm
$BaCl_2$:Ce^{3+}, K^+ (1 %)	13,000 $\pm$ 1,300	35 % at 350/ 370/ 420 nm 12 % at 480 nm
$BaBr_2$	8,700 $\pm$ 870	1 % at 425 nm 2 % at 475 nm
$BaBr_2$:Eu^{2+}	32,000 $\pm$ 3,200	10 % at 404 nm
$BaBr_2$:Ce^{3+} (0.1 %)	36,000 $\pm$ 3,600	8 % at 350 / 370 nm 0.5 % at 420 / 480 nm
$BaBr_2$:Ce^{3+}, K^+ (0.1 %)	65,000 $\pm$ 6,500	-
$BaBr_2$:Ce^{3+}, K^+ (1 %)	54,000 $\pm$ 5,400	6 % at 350 / 370 / 420 nm 2 % 480 nm
BaI_2	1,700 $\pm$ 170	$<$ 0.1 %
BaI_2:Eu^{2+}	2,000 $\pm$ 200	$<$ 0.1 %
BaI_2:Ce^{3+}	1,800 $\pm$ 180	$<$ 0.1 % @ 550 nm

Table 3.5: Integral scintillation efficiency and XL-to-afterglow ratios of undoped, Eu-doped, Ce-doped, and K co-doped barium halides. The x-ray scintillation efficiency was derived by comparing the integrated area under the XL curve of the corresponding barium halide to that of a $CdWO_4$ (28,000 photons/MeV [37]) reference sample. The XL-to-afterglow ratio was detected at the wavelengths indicated.

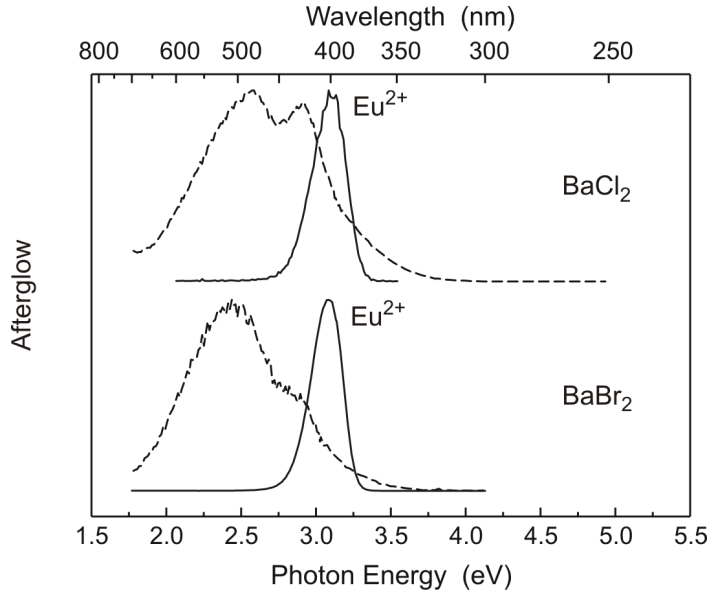

Figure 3.7: Normalized afterglow spectra of undoped and Eu-doped $BaCl_2$ and $BaBr_2$ recorded at RT.

6 Afterglow

Figure 3.7 shows the normalized afterglow spectra of undoped and Eu-doped BaX_2 (X= Cl, Br). The afterglow of undoped and Eu-doped BaI_2 was too weak to allow the recording of the spectral behavior. The afterglow spectra of the Eu-doped samples (Figure 3.7, solid curves) are almost identical to the corresponding XL spectra. The spectra are dominated by the Eu^{2+} emissions at 402 and 404 nm for $BaCl_2$ and $BaBr_2$, respectively. The afterglow spectrum of the undoped $BaCl_2$ (Figure 3.7, dashed upper curve) does not show the broad 300 nm luminescence band found in XL but the double-structured band with peaks at 420 and 475 nm. However, the intensity ratio of the 420 to the 475 nm band has changed in favor of the longer wavelength. For undoped $BaBr_2$ the situation is similar: The afterglow spectrum (Figure 3.7, lower dashed curve) shows the same double-structured band as already observed in XL, with an intensity ratio in favor of the longer wavelength. In both cases, the change in the intensity ratio is caused by the slightly higher afterglow intensity of the longer wavelength band. This finding was confirmed by measurements on the temporal behavior of the XL / afterglow intensity.

Normalized afterglow spectra of 0.1% Ce-doped $BaCl_2$ and $BaBr_2$ are shown in Figure 3.8 (solid curves); normalized afterglow spectra of 1% Ce- and 1% K co-doped samples are also shown (dashes and dotted curves). Ce-doped BaI_2 only shows a very weak afterglow which makes the recording of the spectral behavior impossible. The afterglow spectra of the 0.1% Ce-doped as well as of the 1% Ce and 1% K co-doped samples are dominated by the Ce-doublet. The 420 and 480 nm bands, which have been observed in the XL spectra, are negligible in the afterglow spectra.

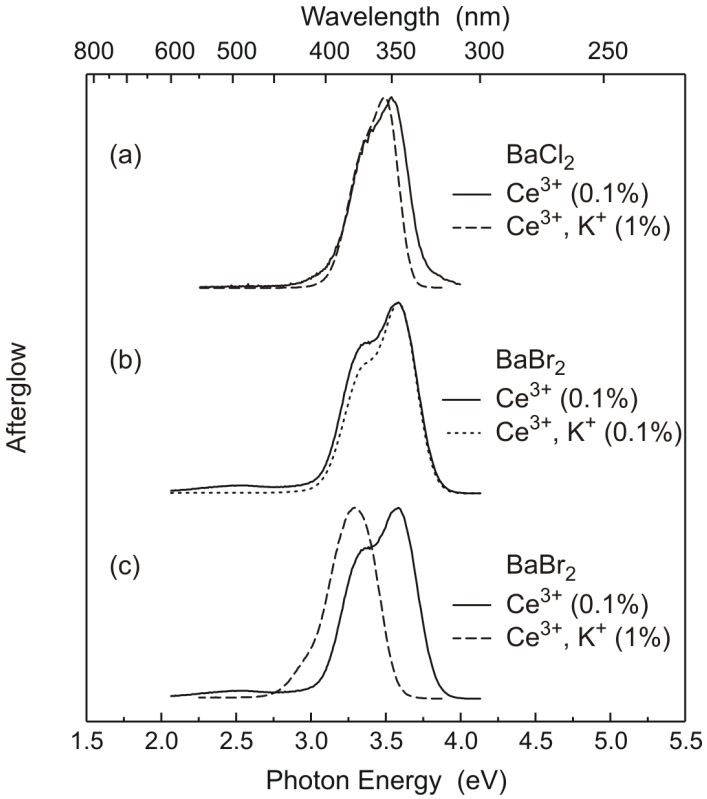

Figure 3.8: Normalized afterglow spectra of (a) $BaCl_2$:Ce^{3+} (0.1%) and $BaCl_2$:Ce^{3+}, K^+ (1%), (b) $BaBr_2$:Ce^{3+} (0.1%) and $BaBr_2$:Ce^{3+}, K^+ (0.1%), and (c) $BaBr_2$:Ce^{3+} (0.1%) and $BaBr_2$:Ce^{3+}, K^+ (1%).

Figure 3.9 shows the temporal behavior of the XL / afterglow intensity of undoped and Eu-doped barium halides after switching on for 5 min and off the x-ray excitation at RT; the resolution of these measurements was 3 sec, i.e. every 3 sec a data point was recorded. Undoped $BaCl_2$ shows an afterglow in the range from 20% (420 nm) to 25% (475 nm). The Eu^{2+} emission in $BaCl_2$ has an afterglow of about 0.2%. In contrast to $BaCl_2$, the afterglow of undoped $BaBr_2$ is less than that of the Eu-doped sample: The Eu^{2+} emission has an afterglow of 10%, while the afterglow in undoped $BaBr_2$ ranges from 1% (425 nm) to 1.5% (475 nm). Undoped and Eu-doped BaI_2 show an afterglow below 0.1%. The XL-to-afterglow ratios detected at the wavelengths indicated are listed in Tab. 3.5

Figure 3.10 shows the temporal behavior of the XL/afterglow intensity of 0.1% Ce-doped (solid curves) and 1% Ce- and 1% K co-doped $BaCl_2$ and $BaBr_2$ (dashed curves) after switching on (for 5 minutes) and off the x-ray excitation at RT; the resolution of these measurements was also 3 sec. The curves have been normalized for easier comparison. As seen in the afterglow spectra above, the afterglow is dominated by the Ce luminescence. The Ce^{3+} emission in 0.1% Ce-doped $BaCl_2$ (Figure 3.10a, solid curves) has an afterglow of about 8%, i.e. the emission intensity drops down to 8% of its value after switching off the x-ray excitation. The additional luminescence bands have an afterglow between 2% (305 nm) and 5% (420 and 480 nm). The 1% Ce- and 1% K-co-doped sample (Figure 3.10a, dashed curves) shows an afterglow of 35% for the Ce-doublet and 12% at 480 nm. The Ce^{3+}

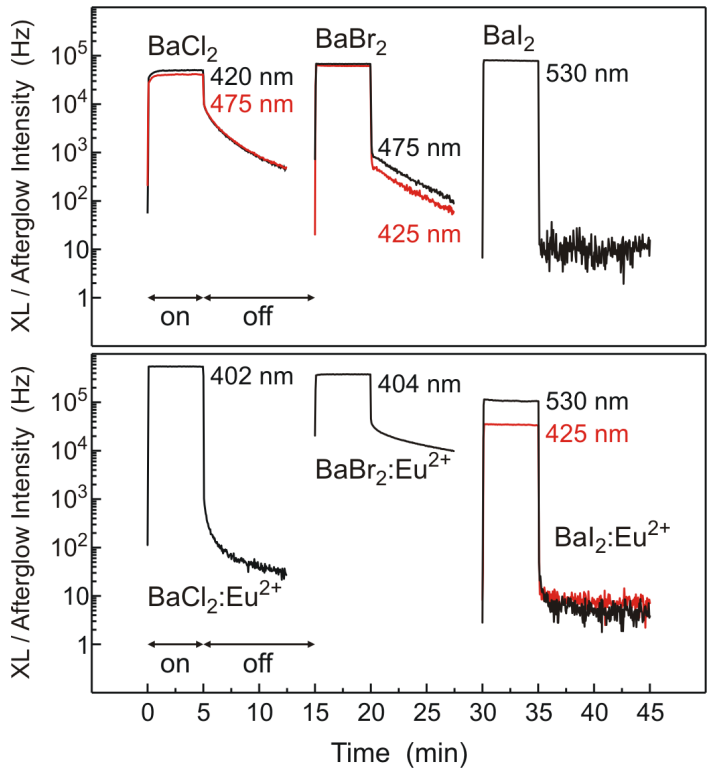

Figure 3.9: Temporal behavior of the XL/afterglow intensity of undoped and Eu-doped barium halides after switching on and off the x-ray excitation at RT; the XL/afterglow intensity was detected at the wavelength indicated.

emission in 0.1% Ce-doped $BaBr_2$ (Figure 3.10b, solid curves) has an afterglow of 8%, while the afterglow of the additional bands at 420 and 480 nm is less than 1%. The afterglow of the 1% Ce- and 1% K co-doped sample (Figure 3.10b, dashed curves) is 6% for the Ce emission and about 2% at 480 nm. Ce-doped BaI_2 shows an afterglow below 0.1%. The XL-to-afterglow ratios detected at the wavelengths indicated are listed in Table 3.5.

7 Light yield and energy resolution

γ-ray light yields and energy resolution for the undoped, Eu-doped, 0.1% Ce-doped, and 1% Ce and 1% K-co-doped $BaCl_2$ and $BaBr_2$ are derived from pulse height spectra under 662 keV γ-ray excitation of a ^{137}Cs source; the spectra of undoped and Eu-doped crystals are shown in Figure 3.11a and b. The spectra of the 0.1% Ce-doped and 1% Ce- and 1% K-co-doped crystals are shown in Figure 3.11c and d.

To determine the position of the photopeak and the energy resolution, the photopeaks were fitted by Gaussian curves. Besides the photopeak at 662 keV, the spectra show the Compton continuum from the Compton edge at about 450 keV down to zero energy. The backscatter

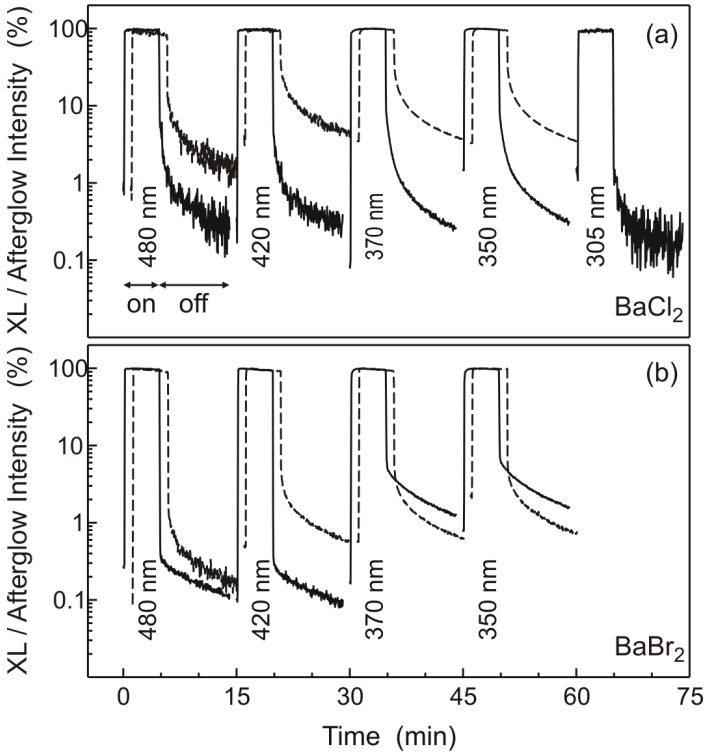

Figure 3.10: Normalized temporal behavior of the XL/afterglow intensity of (a) $BaCl_2$:Ce^{3+} (0.1%) and $BaCl_2$:Ce^{3+}, K^+ (1%) and (b) $BaBr_2$:Ce^{3+} (0.1%) and $BaBr_2$:Ce^{3+}, K^+ (1%) after switching on and off the x-ray excitation at RT. The (dashed) curves for $BaCl_2$:Ce^{3+}, K^+ (1%) and $BaBr_2$:Ce^{3+}, K^+ (1%) were horizontally displaced for clarity. The XL/afterglow intensity was detected at the wavelength indicated.

peak, which arises from scattering of the γ-rays from the photomultiplier and materials outside the system back into the scintillation crystals, is at 200 keV. The leftmost peak at 32 kV corresponds to the K_α x-rays of Ba, which are also emitted in a ^{137}Cs decay.

The unusual broadening of the photopeak in $BaBr_2$:Eu^{2+} is probably caused by inhomogeneities in the crystal. The values for the undoped, Eu-doped and 0.1% Ce-doped BaI_2 were obtained from pulse height spectra under 59.9 keV γ rays of a ^{241}Am source (the spectra are not shown); the BaI_2 crystals did not show any photopeak under a 662 keV γ-ray excitation. γ-ray light yields and energy resolution of all samples investigated are compiled in Table 3.6.

Of all the barium halides studied, undoped $BaBr_2$ and $BaCl_2$:Eu^{2+} show the highest light yield with (19,300 $\pm$ 1,950) and (19,400 $\pm$ 1,950) photons/MeV, respectively. The values were obtained with a shaping time of 10 μs. Increasing the shaping time from 0.5 to 10 μs leads to an increase in the light yield of more than 70% for undoped $BaBr_2$. This change indicates a slow scintillation component in the microsecond range. The increases in the light yield in Eu-doped $BaCl_2$ and $BaBr_2$ are 25% and 30%, respectively. For undoped $BaCl_2$, which shows the lowest yield light of all samples, only a weak increase (mean-

Crystal	Light yield (photons/MeV)		Energy resolution (%)
	0.5 μs	10 μs	
$BaCl_2$	1,500 $\pm$ 150	1,700 $\pm$ 150	17.4 $\pm$ 1.7
$BaCl_2$:Eu^{2+}	14,400 $\pm$ 1,450	19,400 $\pm$ 1,950	8.8 $\pm$ 0.9
$BaCl_2$:Ce^{3+} (0.1%)	1,500 $\pm$ 150	3,100 $\pm$ 310	14.0 $\pm$ 1.4
$BaCl_2$:Ce^{3+}, K^+ (1%)	2,000 $\pm$ 200	5,200 $\pm$ 520	16.2 $\pm$ 1.6
$BaBr_2$	5,100 $\pm$ 510	19,300 $\pm$ 1,950	5.4 $\pm$ 0.5
$BaBr_2$:Eu^{2+}	10,800 $\pm$ 1,100	15,700 $\pm$ 1,550	11.0 $\pm$ 1.1
$BaBr_2$:Ce^{3+} (0.1%)	3,700 $\pm$ 370	13,600 $\pm$ 1,350	10.0 $\pm$ 1.0
$BaBr_2$:Ce^{3+}, K^+ (1%)	5,000 $\pm$ 500	10,300 $\pm$ 1000	9.8 $\pm$ 1.0
BaI_2	1,100 $\pm$ 100	2,600 $\pm$ 250	-
BaI_2:Eu^{2+}	2,300 $\pm$ 250	3,800 $\pm$ 400	-
BaI_2:Ce^{3+}	2,600 $\pm$ 250	4,600 $\pm$ 460	-

Table 3.6: Light yield and energy resolution of the barium halides. The light yield and energy resolution values for $BaCl_2$ and $BaBr_2$ were derived from pulse height spectra (shaping time of 10 μs) under a 662 keV γ-ray excitation of a ^{137}Cs source; the values for BaI_2 were obtained from pulse height spectra under 59.9 keV γ-rays of a ^{241}Am source.

ing a fast scintillation component) is found upon increasing the shaping time from 0.5 to 10 μs. The undoped and Eu-doped BaI_2 show an increase of almost 200%. 0.1% Ce-doped $BaBr_2$ shows the highest γ-ray light yield of all Ce-doped barium halides investigated with (13,600 $\pm$ 1,350) ph/MeV. The values were obtained with a shaping time of 10 μs. Increasing the shaping time from 0.5 to 10 μs leads to an increase in the γ-ray light yield by a factor of about 3.5, which indicates the existence of a slow scintillation component in the μs range. This finding is confirmed by the scintillation decay time measurements (see below). The γ-ray light yield in $BaCl_2$ and BaI_2 - both samples showing a very low light yield - is approximately doubled by increasing the shaping time to 10 μs. Increasing the Ce-doping level to 1% (in combination with additional 1% K-co-doping) leads to a slight increase in γ-ray light yield. In $BaCl_2$ the 0.5 μs as well as the 10 μs value could be increased, whereas in $BaBr_2$ only the 0.5 μs value is found to be larger.

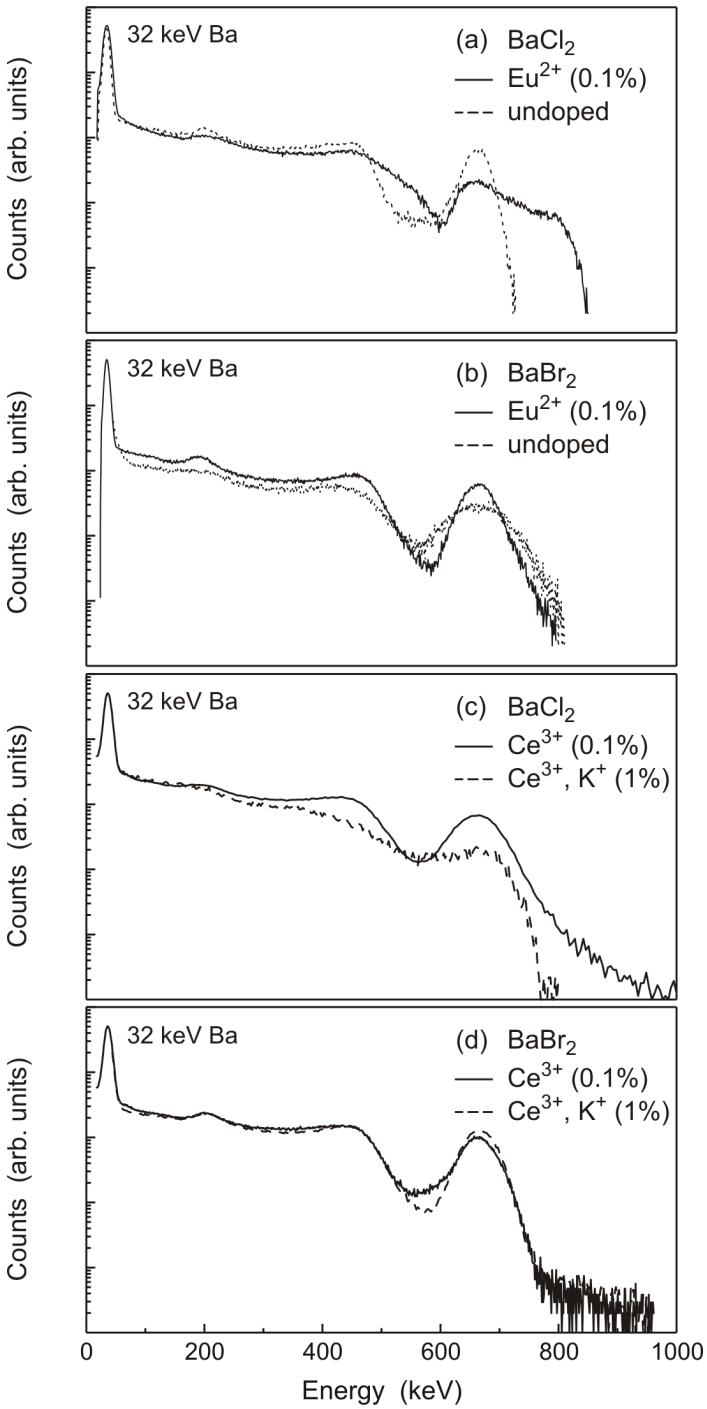

Figure 3.11: Pulse height spectra of (a) Eu-doped and undoped $BaCl_2$, (b) Eu-doped and undoped $BaBr_2$, (c) $BaCl_2$:Ce^{3+} (0.1%) and $BaCl_2$:Ce^{3+}, K^+ (1%), and (d) $BaBr_2$:Ce^{3+} (0.1%) and $BaBr2_2$:Ce^{3+}, K^+ (1%) under a 662 keV γ-ray excitation of a ^{137}Cs source. The spectra are measured with a shaping time of 10 μs at RT.

8 Scintillation decay

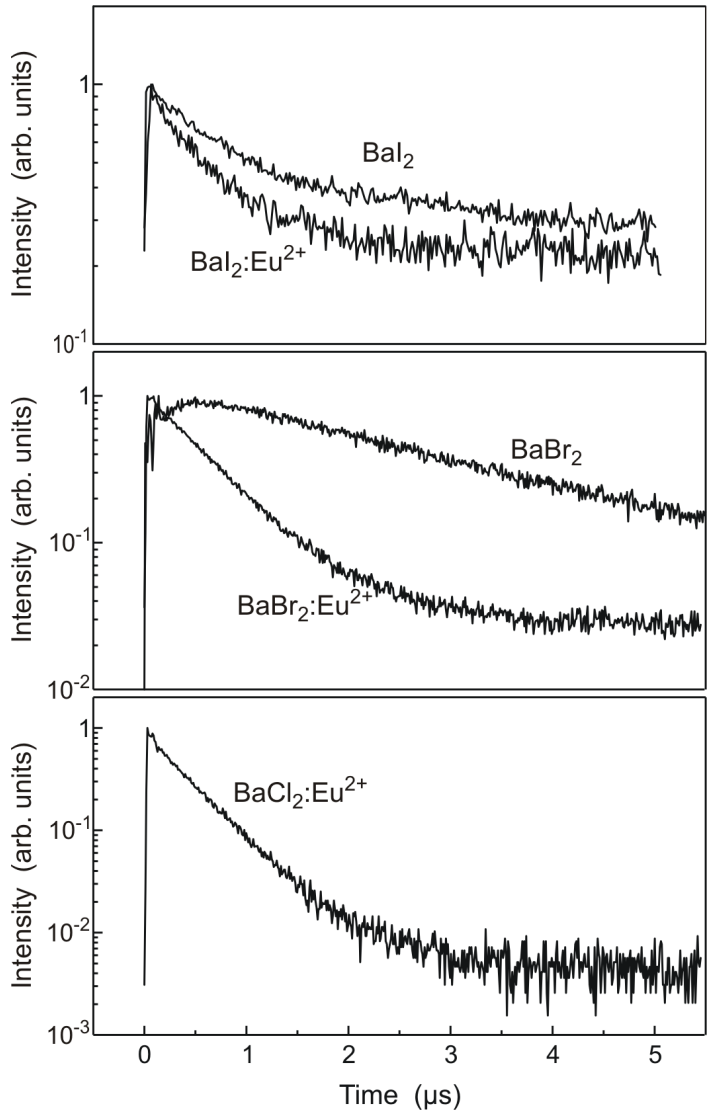

Figure 3.12: Normalized scintillation decay curves of undoped and Eu-doped barium halides under 662 keV γ-ray excitation of a ^{137}Cs source. The measurements for the $BaCl_2$ and the $BaBr_2$ crystals were carried out with the single-photon counting method; those for the BaI_2 crystals with the multi-hit method. All decay curves were recorded at RT.

In Figure 3.12 and 3.13 the scintillation decay curves are presented. All samples were measured with TDC and TAC. The results of the two methods correspond with each other within an error of 10%.

Figure 3.12 shows the scintillation decay curves of undoped and Eu-doped barium halides. The curves for $BaCl_2$ and $BaBr_2$ were measured with the single-photon counting method, whereas those for the BaI_2 samples were measured with the multi-hit method.

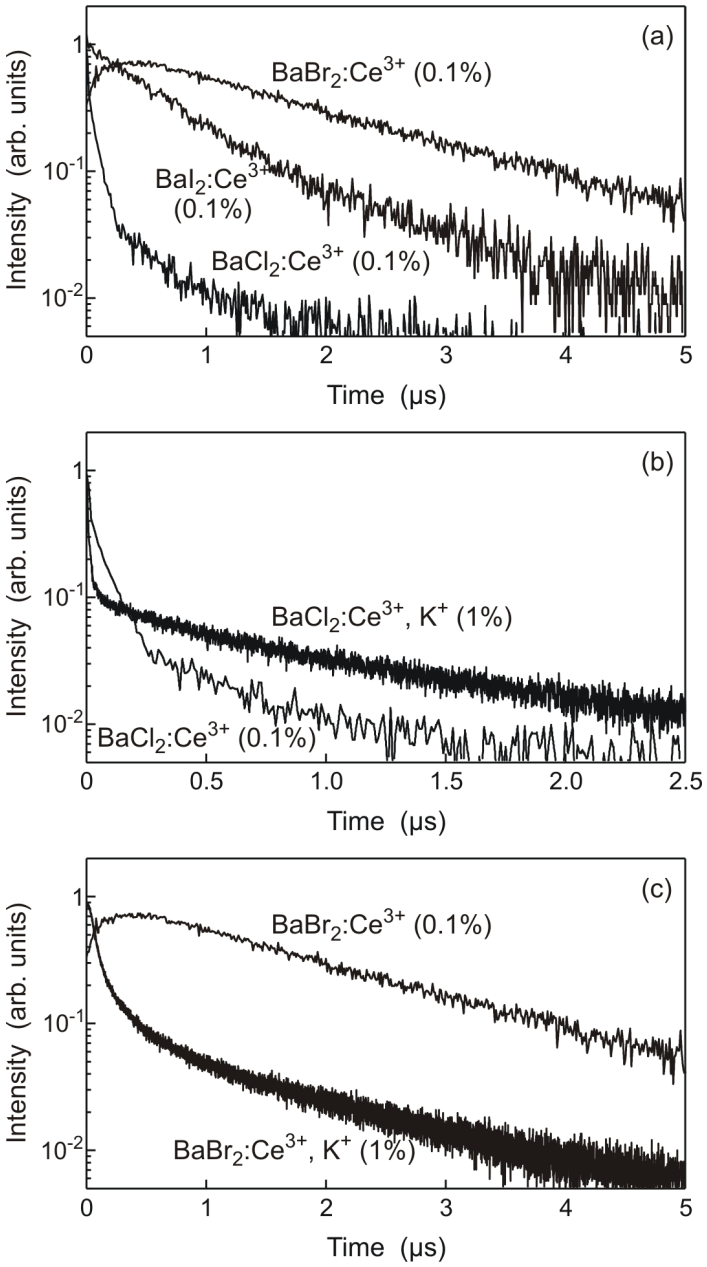

Figure 3.13: Normalized scintillation decay curves of (a) 0.1% Ce-doped $BaCl_2$, $BaBr_2$, and BaI_2, (b) $BaCl_2$:Ce^{3+} (0.1%) and $BaCl_2$:Ce^{3+}, K^+ (1%), and (c) $BaBr_2$:Ce^{3+} (0.1%) and $BaBr_2$:Ce^{3+}, K^+ (1%) under 662 keV γ-ray excitation of a ^{137}Cs source. The measurements for $BaCl_2$:Ce^{3+} (0.1%) and BaI_2:Ce^{3+} (0.1%) were carried out with the multi-hit method; those for $BaBr_2$:Ce^{3+} (0.1%), $BaCl_2$:Ce^{3+}, K^+ (1%), and $BaBr_2$:Ce^{3+}, K^+ (1%) with the single-photon counting method.

Crystal	Scintillation decay time (ns)	relative contribution to total γ-ray light yield (for a shaping time of 10 μs)
$BaCl_2$	980 ± 100	100%
$BaCl_2$:Eu^{2+}	390 ± 40	100%
$BaCl_2$:Ce^{3+} (0.1%)	14 ± 1	10%
	90 ± 9	40%
	$1{,}400 \pm 140$	50%
$BaCl_2$:Ce^{3+}, K^+ (1%)	7 ± 1	6%
	190 ± 20	11%
	$1{,}500 \pm 150$	83%
$BaBr_2$	$2{,}200 \pm 220$	100%
		τ_{rise} = (200 $\pm$ 20) ns
$BaBr_2$:Eu^{2+}	585 ± 60	100%
$BaBr_2$:Ce^{3+} (0.1%)	$1{,}700 \pm 170$	100%
		τ_{rise} = (150 $\pm$ 15) ns
$BaBr_2$:Ce^{3+}, K^+ (1%)	80 ± 8	27%
	490 ± 50	22%
	$2{,}100 \pm 210$	51%
BaI_2	610 ± 50	
	5000 (const)	
BaI_2:Eu^{2+}	510 ± 50	
	5000 (const)	
BaI_2:Ce^{3+}	590 ± 60	71%
	$2{,}200 \pm 200$	29%

Table 3.7: Scintillation decay of the barium halides. The scintillation decay measurements for the $BaCl_2$ and $BaBr_2$ crystals were carried out with the single-photon counting method, those for the BaI_2 crystals with the multihit method. For the fitting of the BaI_2 decay curves, the second component was kept constant.

The scintillation decay components are collected in the last column of Table 3.7. The decay components for Eu-doped $BaCl_2$ and $BaBr_2$ are much faster than those observed for the corresponding undoped sample, whereas both undoped and Eu-doped BaI_2 show about the same temporal behavior. The emission in BaI_2 is dominated by the 530 nm band, and its decay can be fitted by assuming two different components.

Figure 3.13a shows the scintillation decay curves of 0.1% Ce-doped $BaCl_2$, $BaBr_2$, and BaI_2. The presented curve for $BaBr_2$ was measured with the single-photon counting method whereas those for $BaCl_2$ and BaI_2 were measured with the multi-hit method. The scintillation decay components are shown in Table 3.7 together with their relative contribution to the total γ-ray light yield. In contrast to 0.1% Ce-doped $BaCl_2$ and BaI_2 the decay curve of 0.1% Ce-doped $BaBr_2$ shows an initial rise in the scintillation intensity before a slow, mono-exponential decay is observed. The normalized decay curve can be described by:

$$I(t) = \underbrace{(1 - exp(-t/\tau_{rise}))}_{I_0} \cdot exp(-t/\tau) \tag{3.2}$$

with the initial rise time τ_{rise} and the decay time τ for the mono-exponential decay. A revised analysis of the scintillation decay in undoped $BaBr_2$ showed that such an initial rise can be observed there as well. The initial rise times are listed in the last column of Table 3.7. K-co-doping of 1% Ce-doped $BaCl_2$ and $BaBr_2$ leads to significant changes in the scintillation decay (Figure 3.13b and 3.13c). The $BaCl_2$:Ce^{3+}, K^+ (1%) and $BaBr_2$:Ce^{3+}, K^+ (1%) decay curves can be fitted by assuming three components. The scintillation decay times of the K-co-doped samples as well as the relative contribution of each component to the total γ-ray light yield are given in Table 3.7.

9 Discussion

The x-ray excited Eu^{2+} emission in Eu-doped barium halides (Figure 3.5) shifts from Cl to I to longer wavelengths. For Eu-doped $BaCl_2$ and $BaBr_2$ the Eu^{2+} emission dominates the XL spectrum; the doublestructured XL band at about 450 nm observed in the undoped samples cannot be seen in Eu-doped $BaCl_2$, but it is found as a small shoulder in the case of Eu-doped $BaBr_2$ (Fig. 3.5, dotted curves). The XL band at 530 nm in undoped BaI_2 is also present in the XL spectrum of Eu-doped BaI_2 and is even more intense than the Eu-correlated emission at 425 nm. The 450 nm XL found in undoped $BaBr_2$ has previously been ascribed to F-V_K center recombination [38]. The 450 nm band in undoped $BaCl_2$ and the 530 nm band in BaI_2 might be caused by the same process. We assume that there is an energy transfer mechanism between the F-V_K pair and Eu^{2+}. This transfer is very efficient in the case of $BaCl_2$, efficient in the case of $BaBr_2$, but almost completely suppressed in the case of BaI_2. The reason for this is still unclear. At this point, we cannot say much about the scintillation mechanism in the barium halides investigated because dedicated experiments, such as decay time and light yield measurements (as a function of temperature and concentration), were not performed. The aim of this work was to explore whether the materials studied can be interesting candidates as scintillator.

The x-ray excited Ce^{3+} emission in $BaCl_2$, $BaBr_2$, and BaI_2 (Figure 3.6, solid curves) was found in $BaCl_2$ and $BaBr_2$, but it is suppressed in the BaI_2 lattice. The 550 nm band observed in Ce-doped BaI_2 is also present in the XL spectrum of undoped BaI_2. The XL spectrum of Ce-doped $BaCl_2$ is dominated by the Ce^{3+} emission with additional weak bands at 420 and 480 nm as well as at 305 nm (provisionally assigned to STE emission). These bands are completely suppressed in the K-co-doped sample. The position of the Ce^{3+} emission shifts slightly to longer wavelengths upon increasing the doping level from 0.1% to 1%. This agrees with findings by Li and Leskelä [39]: They observed a shift in the emission wavelength, in Ce-doped $BaCl_2$, from 340 to 356 nm, when the Ce doping level is increased from 0.05% to 5%. The Ce-doublet in the $BaBr_2$ spectra is still the most intense emission but additional XL bands at about 420 and 480 nm play a significant role in the spectrum. Similar bands at 420 and 480 nm have already been reported in undoped $BaBr_2$. The situation in Ce-doped $BaBr_2$, however, is more complicated. There are (at least) three different Ce sites in $BaBr_2$ [36]: (A) The so-called A-site (doublet at 349/373 nm) is attributed to Ce ions charge-compensated by a K impurity; (B) the B-site (420 nm) is assumed to be a Ce ion in the vicinity of any other impurity; (C) the C-site (330/353 nm) can only be seen at low temperatures and is attributed to an unperturbed Ce-site. This assignment by Corradi et al. [36] is in good agreement with our XL results. Upon 0.1% K-co-doping (Figure 3.6b, dotted curve) the A-site to B-site ratio changes in favour of the A-site; for a Ce and K co-doping level of 1% (Fig. 3.6c, dashed curve) the B-site has completely disappeared while the A-site is shifted to longer wavelengths. The latter result is consistent with the findings for 1% Ce- and 1% K-co-doped $BaCl_2$ (Figure 3.6a, dashed curve).

The 0.1% Ce-doped $BaBr_2$ sample shows a large contribution of host lattice emission bands at 420 and 480 nm (Figure 3.6b and 3.6c, solid curves), an initial rise in the scintillation decay curve (Figure 3.13a and 3.13c), and there is no fast decay component although there is significant contribution from Ce^{3+} emission (Table 3.7). These observations indicate that the Ce^{3+} exitation in the 0.1% Ce-doped $BaBr_2$ is delayed either due to energy migration processes from the ionization track to Ce^{3+}. Although we do not know what kind of migration process it is, it is clear that the observed scintillation decay is determined by both the Ce^{3+} $5d$ lifetime and the speed of migration/ excitation. If the latter process is much slower than the Ce^{3+} $5d$ lifetime then the scintillation decay is fully controlled by the migration/ transfer process. We assume that the defects involved in the migration processes are the same as the ones responsible for the host related emission bands at 420 and 480 nm (Figure 3.6b and 3.6c, solid curves). The 1% K-co-doping, however, causes a significant change in the scintillation behavior. The additional emission bands assigned to host lattice emission bands at 420 and 480 nm disappear (Figure 3.6c, dashed curve) and a fast decay component of 80 ns can now be found in the corresponding scintillation decay curve (Figure 3.13c). It seems that the transfer from the host related defects to the Ce ions is much enhanced by K-co-doping. The host emission is quenched by the fast transfer to Ce, which results in more intense and faster Ce scintillation decay. The decay is still controlled by the migration/transfer process, but the lifetime of this process decreases to 80 ns. The intrinsic lifetime of the Ce^{3+} $5d$ state is expected to be significantly shorter than 80 ns; we anticipate a lifetime around 20-30 ns.

The best scintillator of all investigated barium halides (with respect to light yield, scintillation decay time, and afterglow) is Eu-doped $BaCl_2$. The light yield is 19,400 photons/MeV

(Table 3.6), the scintillation decay consists of a fast component on the submicrosecond scale (about 400 ns, Table 3.6), and the afterglow is less than 0.2% (Table 3.5). Moreover, the energy resolution under the 662 keV γ-ray excitation of a ^{137}Cs source is 8.8%. Although undoped $BaBr_2$ is also a good scintillator in terms of the light yield (19,300 photons/MeV,´Table 3.6), its scintillation decay component is on the multiple microsecond scale (2200 ns, Table 3.6), which makes this system less attractive for scintillation applications. The XL-to-afterglow-ratio of undoped $BaBr_2$ is 1% - 2%; the energy resolution is 5.4% and thus slightly better than that of Eu-doped $BaCl_2$.

According to Table 3.6, the Ce-doped $BaBr_2$ samples show the highest γ-ray light yield of the Ce-doped barium halides investigated: The light yield for 1% Ce- and 1% K-co-doped $BaBr_2$ is 13,600 ph/MeV and 10,300 ph/MeV, respectively. Additional K-co-doping did not (as expected) increase the γ-ray light yield but led to an even smaller value. Interestingly, in undoped $BaBr_2$ a light yield of 19,600 ph/MeV was found; this is significantly more than the values for the corresponding Ce-doped samples. However, the K co-doping had a significant influence on the scintillation decay behavior: In 1% Ce- and 1% K-co-doped $BaBr_2$ a fast, medium, and slow decay time component could be observed, while the scintillation decay in undoped $BaBr_2$ and in 0.1% Ce-doped $BaBr_2$ consists of only one slow component and the decay occurs via an intermediate level. The K co-doping does not have a significant influence on the afterglow behavior or on the energy resolution under 662 keV γ-ray excitation of a ^{137}Cs source. Both, Ce-doped $BaCl_2$ and Ce-doped BaI_2 show a very weak γ-ray light yield (Table 3.6), which makes these systems less attractive for scintillation applications. Similar to the situation in Ce-doped $BaBr_2$, increasing the Ce-doping level as well as additional K doping did not help very much to improve the scintillation properties of Ce-doped $BaCl_2$.

At first glance, a comparison between the light yield values obtained from the pulse height spectra (Table 3.6) and the integral x-ray scintillation efficiencies obtained from the XL spectra (Table 3.5), which were compared to $CdWO_4$ (28,000 photons/MeV [37]), shows that some of the data do not agree with each other. Apart from Eu-doped $BaCl_2$ and all of the BaI_2 samples, the integral x-ray scintillation efficiency is always significantly higher than the γ-ray light yield of the corresponding crystal. An explanation for this discrepancy lies in the recording method of the data: The γ-ray light yield values derived from the pulse height spectra were recorded with a maximum shaping time of 10 μs, whereas each data point of the XL spectra was obtained after 1-2 s of integration, and was thus additionally increased by afterglow effects. The light yield values in Table 3.6 agree with those in Table 3.5 in the case of low afterglow samples, e.g., Eu-doped $BaCl_2$. Samples having an intense afterglow such as undoped $BaCl_2$, Ce-doped $BaCl_2$, Eu-doped, and Ce-doped $BaBr_2$ show in the XL spectra a much higher light yield, leading to a higher value in Table 3.5. In addition, since the scintillation decay measurements have been recorded for a shaping time of only 10 μs, very slow decay time components in the range of several micro- or even milliseconds are difficult to detect. The last column of Table 3.7 shows that the relative contribution to the total light is often dominated by such slow components. The XL light yield values for the BaI_2 samples are smaller than those of the pulse height spectra values. BaI_2 is very hygroscopic and becomes opaque while performing the XL measurements; the light yield thus decreases. For the pulse height spectra, the measurements were performed at the Uni-

versity of Delft inside an M-Braun Unilab dry box with a moisture content less than 1 ppm. Finally, one may not exclude a nonproportional response of the scintillators with energy of excitation. Usually, scintillators are less efficient at x-ray energies (10 - 50 keV) than at γ-ray energy (662 keV), and this may also contribute to differences between the integral scintillation efficiency in Table 3.5 and the γ-ray light yield in Table 3.6.

4 Ce-doped glass ceramics

It is known from prior investigations that the main problem when doping fluorozirconate (FZ) based glass ceramics with Ce is to get the Ce into the barium halide nanocrystals. Ce-doped FZ glass ceramics have already been prepared and described by [4, 9]. Unfortunately, it seems that the Ce ions do not enter the nanocrystals. The x-ray luminescence of the glass ceramics looks similar to that of undoped single crystals [4]. This indicates that nanocrystals have been created in the glass ceramic, but they are probably not doped with Ce.

The valence state of the Ce ion seems to be the problem. In the case of Eu the divalent rare-earth ion substitutes on a divalent Ba site in the nanocrystals. The Ce ion is trivalent, but has to substitute on a divalent Ba site, too. The idea is to add a monovalent ion for charge compensation. Since investigations on Ce- and K-co-doped single crystals of barium halides have shown that potassium shows no additional luminescence but increases the intensity of the Ce luminescence (Chapter 3 and [39]), K was chosen as co-dopant. Glass ceramics with different doping levels of Ce and K were prepared. Table 4.1 lists the composition of the three manufactured glasses. The name of the samples is a composition of the abbreviation ZBLAN given by the compounds of the FZ glasses and an inventory number. Each set consist of an initial sample and glass ceramics annealed for 20 minutes at 260°C, 270°C, 280°C, 285°C, and 290°C.

From investigations on ZBLAN 74, the problem with trivalent dopants is already known. The results have been published in [9]. XRD measurements have shown that due to annealing hexagonal $BaCl_2$ nanocrystals are formed in the glass. After annealing for 20 minutes at 260°C the XRD data show reflections from hexagonal $BaCl_2$. Upon annealing at higher temperatures a phase transition from hexagonal to orthorhombic $BaCl_2$ could be observed:

Sample	AlF_3	LaF_3	$BaCl_2$	BaF_2	NaCl	InF_3	ZrF_4	CeF_3	KF
ZBLAN 74	3	3.5	10	10	20	0.5	52	1	-
ZBLAN 90	3	3.5	10	10	20	0.5	51	1	1
ZBLAN 96	3	3.5	10	10	20	0.5	49	2	2

Table 4.1: Composition of the Ce- and Ce- and K-co-doped fluorochlorozirconate glasses in mole percent. The name of the samples is a composition of the abbreviation ZBLAN given by the compounds of the FZ glasses and an inventory number.

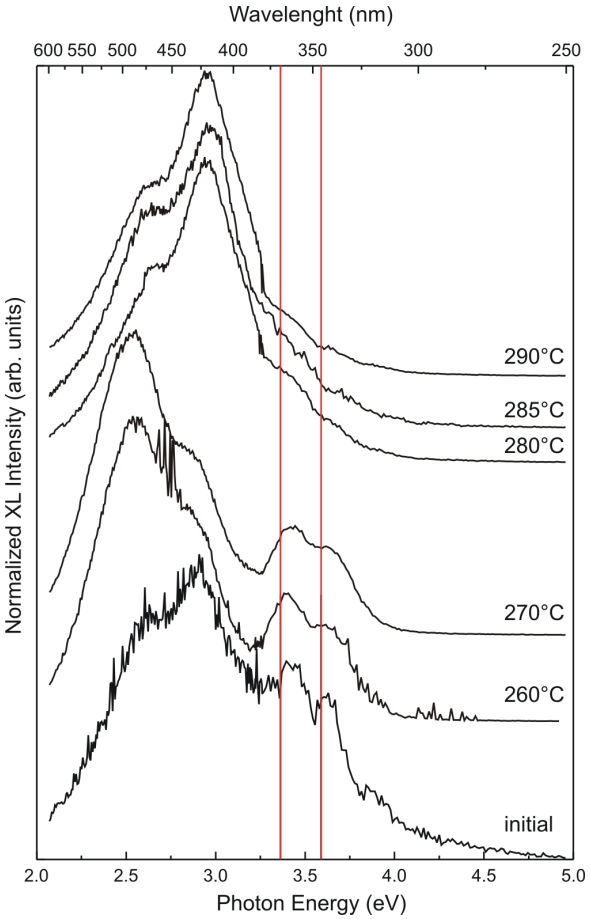

Figure 4.1: Normalized XL spectra of Ce-doped ZBLAN 74 glass ceramics. The two red lines denote the positions of the Ce doublet of a $BaCl_2$:Ce^{3+} single crystal.

At an annealing temperature of 270°C the XRD data shows a phase mixture of hexagonal and orthorhombic $BaCl_2$. The phase transition is completed after annealing for 20 minutes at 280°C, the hexagonal phase has completely disappeared in the XRD pattern. However, the appearance of an unknown third phase after annealing at 280°C can be observed. The crystallites of this phase grow with increasing annealing temperature.

1 Experimental results

Figure 4.1 shows the XL spectra (from bottom to top) of the initial glass and the glasses annealed at 260°C, 270°C, 280°C, 285°C, and 290°C. The two red lines denote the positions of the Ce doublet of a $BaCl_2$:Ce^{3+} single crystal. In all spectra of the annealed samples an emission at 420 and 480 nm can be observed which is attributed to that of undoped $BaCl_2$ single crystals, apart from the initial glass ceramics (where we have no nanocrystals). The spectra of the initial, the 260°C, and the 270°C samples of 1% Ce doped ZBLAN 74

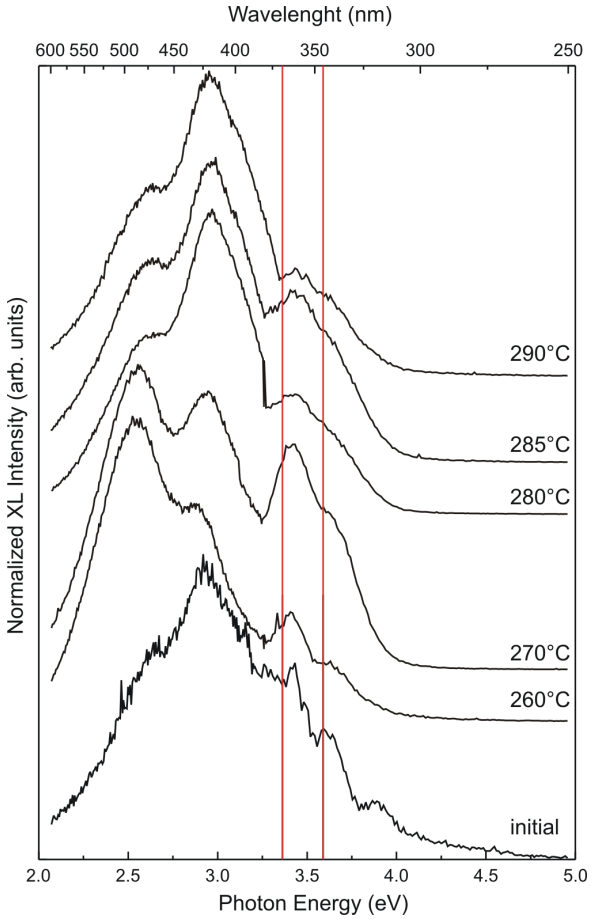

Figure 4.2: Normalized XL spectra of Ce- and K-codoped ZBLAN 90 glass ceramics. The two red lines denote the positions of the Ce doublet of a $BaCl_2$:Ce^{3+} single crystal.

(Figure 4.1) also show a luminescence which can be attributed to Ce. In the spectra of the 280°C, the 285°C, and the 290°C samples only two broad bands at 420 and 480 nm can be observed. The XL spectra reflect the phase transitions seen in the XRD patterns. The spectra can be classified into three sections: The first one is the spectrum of the initial glasses. The second one consists of the spectra of the glasses including crystallites of hexagonal $BaCl_2$, which are the glasses annealed at 260°C and 270°C. The spectra of these glasses have the same pattern and differ from the XL spectra of the other glasses. The third and last section includes the spectra of the samples annealed at 280°C, 285°C, and 290°C. The samples of this section show according to the XRD data the presence of orthorhombic $BaCl_2$ nanocrystals and the unknown "x-phase".

Figure 4.2 and 4.3 show the XL spectra (from bottom to top) of the initial glass and the glasses annealed at 260°C, 270°C, 280°C, 285°C, and 290°C of 1% Ce and K-codoped ZBLAN 90 and 2% Ce and K-codoped ZBLAN 96 glass ceramics, respectively. The two red lines denote the positions of the Ce doublet of a $BaCl_2$:Ce^{3+} single crystal. The spectra of 1% Ce- and K-co-doped ZBLAN 90 (Figure 4.2) are similar to that of the 1% Ce-doped ZBLAN 74 samples. The spectra can also be classified into three sections, which have already been de-

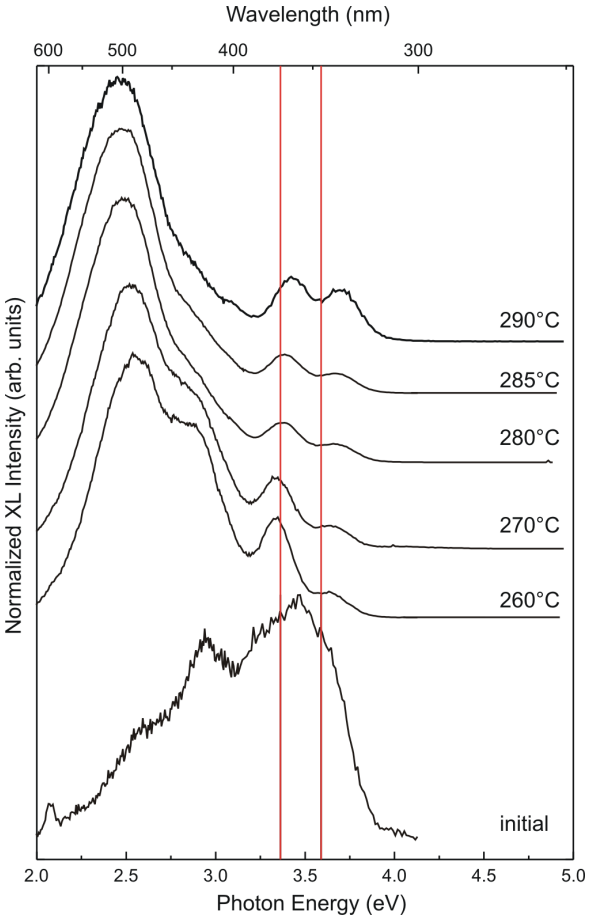

Figure 4.3: Normalized XL spectra of Ce- and K-codoped ZBLAN 96 glass ceramics. The two red lines denote the positions of the Ce doublet of a $BaCl_2$:Ce^{3+} single crystal.

scribed above. The broad bands at 420 and 480 nm can be observed in all annealed samples. While the 480 nm band is more intense in the 260°C and the 270°C samples, the intensity has changed in favor to 420 nm for the 280°C, the 285°C, and the 290°C samples. A doublet which can be attributed to Ce luminescence can be observes in all spectra, also those of the 280°C, the 285°C, and the 290°C samples.

The spectrum of the initial ZBLAN 96 (Figure 4.3) has a different shape than those of ZBLAN 74 and ZBLAN 90. The maxima of the curve are in the region of the luminescence of Ce in the glass matrix and not dominated by the luminescence at 420 and 480 nm. The 420 and 480 nm band can be found in all annealed samples and the 480 nm band is always the most intense one. A Ce luminescence can also be observes in all annealed samples and this time a double band shape can really be observed. The classification into three sections as done for the other two sample sets can not be made.

The wavelengths of the glass ceramic samples are not identical with those of the single-crystalline Ce-doped $BaCl_2$. Table 4.2 shows the wavelengths of all samples and that of undoped and Ce-doped $BaCl_2$ single crystals for comparison.

Sample	Wavelength (nm)	
$BaCl_2$	420, 480	
$BaCl_2$:Ce^{3+}		349, 373
ZBLAN 74		
as made	475, 420	360, 340, 316
260°C	485, 430	365, 340
270°C	485, 430	365, 340
280°C	475, 420	365, 335
285°C	475, 420	365, 335
290°C	475, 420	365, 335
ZBLAN 90		
as made	470, 420	360, 340, 317
260°C	485, 430	365, 340
270°C	485, 430	365, 340
280°C	475, 420	365, 340
285°C	475, 420	365, 340
290°C	475, 420	365, 340
ZBLAN 96		
as made	470, 420	358
260°C	485, 430	370, 340
270°C	485, 430	370, 340
280°C	500, 425	365, 335
285°C	500, 425	365, 335
290°C	500, 425	360, 335

Table 4.2: Emission wavelength of the glass ceramic samples and for comparison of undoped and Ce-doped $BaCl_2$ crystal.

2 Discussion

An increase in the Ce luminescence upon co-doping with K can be observed. The Ce-doublet in the spectra of the ZBLAN 90 is more intense than that of the ZBLAN 74 samples. In the spectra of the annealed ZBLAN 96 samples the Ce luminescence is more distinctive, the double band shape of Ce can be observed. Even the spectrum of the initial glass of ZBLAN 96 is dominated by Ce luminescence (of course, luminescence of Ce in the glass matrix), and looks different to that of ZBLAN 74 and ZBLAN 90. All spectra of the annealed samples are still dominated by the luminescence of undoped $BaCl_2$ nanocrystals.

It can be seen that codoping with potassium and increasing the Ce doping level can increase the Ce luminescence. Unfortunately, the wavelength of the doublet of the 280°C, the 285°C, and the 290°C samples of ZBLAN 96 do not agree exactly with the Ce luminescence found

in Ce-doped $BaCl_2$ single crystals. In chapter 3 can be seen and also Li et al. [39] reported that increasing the doping level and codoping with potassium can have an effect on the wavelength. The Ce emission is shifted to longer wavelength not to shorter ones as it can be observe in these spectra. Unfortunately, it is not clear that the Ce is in the nanocrystals. It is possible that the nanocrystals have an effect on the wavelength. An influence of particle size on the emission wavelength has been observed for different nanoparticles [40–43]. Shifts to shorter wavelengths as well as longer wavelength have been observed depending on the nanocrystal.

The change in the intensity of the broad bands at 420 and 480 nm is an effect of the phase transition from hexagonal $BaCl_2$ to orthorhombic $BaCl_2$. The phase transition can be observed in the XRD data. The phase transition of the barium chloride nanocrystals always takes place upon annealing at 280°C. This intensity change can not be observed in the spectra of ZBLAN 96. Unfortunately, we do not have any XRD data of this sample set. It is possible that the higher doping level influences the spectra of the samples and/or the phases of the nanocrystals.

5 Sm- and Mn-doped single crystals and glass ceramics

1 Motivation

The results of this chapter are based on a cooperation with Schott AG (Mainz, Germany) being funded within the project "FLUOPLEX" by the Federal Ministry of Education and Research (Bundesministerium für Bildung und Forschung - BMBF). The main intention of this project is to find a fluorescence standard. This standard can be one sample or a set of samples. The spectrum of a fluorescence standard can be used to compare or to calibrate spectra of other samples measured in non-calibrated spectrometers.

A fluorescence standard has to match some requirements: The spectrum of the standard must be reproducible and the standard must be producible in varying shape and size to fit any spectrometer. The producibility in varying shape and size leads to the idea of using a glass or a glass ceramic for the application as a fluorescence standard. Eu-doped fluorozirconate (FZ) based glass ceramics show PL and XL spectra and with this they seem to be promising candidates. Since there are a few more requirements for a fluorescence standard we need an other dopant instead of Eu. The emission spectrum of the standard should be in the visible range and it should have line and band emissions. The dopant of the glass ceramic should be divalent since we know from prior investigations (chapter 4) that there is a problem embedding trivalent ions in the nanocrystals. A rare-earth ion which fits all these requirements is Sm. As an alternative to rare-earth ions the transition ion Mn was also considered as a dopant. Both dopants have their emission wavelengths in the visible range. Since the emission of scintillators is often carried out with photodiodes a wavelength in the visible range is also interesting for scintillators. Common photodiodes are more sensitive in the visible range than in the UV. Therefore all samples were also investigated on their scintillation properties.

For the investigations four single crystals were grown: Sm-doped $BaCl_2$, Sm-doped $BaBr_2$, Mn-doped $BaCl_2$, and Mn-doped $BaBr_2$. Also a set of Sm-doped fluorobromozirconate (FBZ) glass ceramics and Mn-doped fluorochlorozirconate (FCZ) glass ceramics were investigated. A set includes an as-made glass and glass ceramics annealed for 20 minutes at 260°C, 270°C, 280°C, 285°C, and 290°C.

Sample	AlF_3	LaF_3	BaF_2	BaX_2	NaF	NaX	InF_3	YF_3	ZrF_4	SmX_2	X
ZBLAN 91	3	3.5	10	10	-	20	0.5	-	52	1	Br
ZBLAN 93	3	1.5	20	-	5	15	1	1.5	52	1	Br
ZBLAN 95	3	1.5	20	-	5	15	1	1.5	52	1	Br
ZBLAN 104	3	1.5	20	-	5	15	1	1.5	52	1	Br
ZBLAN 108	3	3.5	10	10	-	20	0.5	-	52	1	Cl
ZBLAN 114	3	1.5	20	-	5	15	1	1.5	52	1	Br

Table 5.1: Composition of Sm-doped glasses. The name of the samples is a composition of the abbreviation ZBLAN given by the compounds of the FZ glasses and an inventory number.

2 Sample Preparation

Single crystals of BaX_2 (X = Cl, Br) were grown in the Paderborn crystal growth laboratory using the Bridgman method with a quartz ampoule under SiX_4 atmosphere from BaX_2 powder and 1000 molar ppm of SmX_2 or MnX_2, respectively. The usual technique was completed by slow cooling through the cubic-orthorhombic phase transition near 920°C ($BaCl_2$) [28] and 800°C ($BaBr_2$) [31], respectively. Prior to crystal growth the BaX_2 powder was dried in a vacuum with subsequent melting in a SiX_4 atmosphere to reduce oxygen contamination.

The preparation of the FZ glass ceramics is as followed: The base composition is additionally doped with the dopant SmX_2 or MnX_2 (X = Cl, Br) and bromine or chlorine. The constituent chemicals were melted in a glass carbon crucible at 740°C in an inert atmosphere of nitrogen, then cooled down to 650°C and then poured into a brass mould which was at temperature of 200°C where it is below the glass temperature. The samples were subsequently annealed at 260°C, 270°C, 280°C, 285°C, and 290°C for 20 minutes in an inert atmosphere of nitrogen. Table 5.1 and 5.2 give an overview on Sm- and Mn-doped glasses, respectively.

During the preparation of the Sm-doped FZ glasses some problems occurred. ZBLAN 91 was immediately a ceramic because it was made with the wrong composition. The composition of FCZ glasses can not be used for FBZ glasses by replacing all chlorine compounds by bromine ones. ZBLAN 93 was immediately a ceramic, too. Usually, the FZ glasses were melted in a glassy carbon crucible at 745°C, in an inert atmosphere of nitrogen. Then the glass was poured into a mould which was at 200°C, below the glass temperature of 260°C. When changing the temperature of the mould to 150°C the Sm-doped FBZ glass stays transparent (ZBLAN 95 and 104). The glass has a redish color. The Sm-doped FCZ glass (ZBLAN 108) was transparent, but colorless. Luminescence measurements showed that no divalent, but trivalent Sm was in the glass. Unfortunately, it was not possible to reduce Sm from a trivalent to a divalent state. One part of the glass was ground and 2% LiH was added. The mixture was melted and poured out again. The glass has turned black, but no Sm^{2+} could be found. An other part of ZBLAN 108 was ground and 2% of NH_4HF_2

Sample	AlF_3	LaF_3	BaF_2	$BaCl_2$	NaCl	InF_3	ZrF_4	$MnCl_2$
ZBLAN 97	3	3.5	10	10	20	0.5	52	1
ZBLAN 99	3	3.5	10	10	20	0.5	52	1

Table 5.2: Composition of Mn-doped glasses. The name of the samples is a composition of the abbreviation ZBLAN given by the compounds of the FZ glasses and an inventory number.

was added. The mixture was melted and poured out. This time the glass stayed colorless with no change in the valence state of Sm. Since the $SmBr_2$ used for the glasses ZBLAN 91, 93, 95, and 104 was all gone a single crystal of $SmBr_2$ was grown in the Paderborner crystal grow lab. This crystal was used for ZBLAN 114. Unfortunately, the glass stays colorless, which indicates that no Sm^{2+} is in the glass. The run to reduce the samarium in a H_2-N_2 atmosphere as described in [44], did not work either.

The preparation of the Mn-doped glasses was less complicated. The first glass turned immediately into a ceramic but after increasing the temperature gradient by lowering the temperature of the brass mould to 150°C the glass stayed transparent. The Mn-doped glasses were reproducible. In contrast to Sm, Mn only exists in the divalent state. This fact may be the reason that Mn-doped glasses are easier to produce than the Sm-doped ones.

3 Experimental results

This section is split into two parts: one part shows the results of the Sm-doped samples and the other one those of the Mn-doped samples. Both parts start with the PL and XL measurements of the singles crystals followed by those of the glass ceramics and at the end some additional investigations of the samples are presented: dual energy measurements of the Sm-doped glass ceramics in combination with Eu-doped glass ceramics and EPR measurements of the Mn-doped single crystals and glass ceramics. A comparison of the scintillation efficiency of the Sm- and Mn-doped single crystals is given in the discussion.

3.1 Sm-doped samples

Samarium is an rare-earth element. It shows in luminescence line emission as well as band emission. The line emissions are transitions from the $^5D_0$ to the ^7F levels ($^7F_4$, $^7F_3$, $^7F_2$, $^7F_1$, and $^7F_0$) [45]. The band emissions are transitions from the $4f^55d$ to the $4f^6$ level [45]. Lauer et al. [46] reported the energy levels (in cm^{-1}) of Sm^{2+} in $BaCl_2$ and $BaBr_2$. The energy levels (in eV) are listed in Table 5.3. The possible transition energies from the $^5D_0$ state to the ^7F-states are also listed in Table 5.3.

	$BaCl_2$		$BaBr_2$	
Energy level	level energy	transition energy	level energy	transition energy
$^5D_1$	1.9710		1.9707	
	1.9698		1.9700	
	1.9690		1.9692	
$^5D_0$	1.8034	0	1.8035	0
$^7F_4$	0.2868	1.5166	0.2865	1.517
	0.2840	1.5194	0.2857	1.5178
	0.2822	1.5212	0.2833	1.5202
	0.2775	1.5259	0.2778	1.5257
	0.2751	1.5283	0.2757	1.5278
$^7F_3$	0.1885	1.6149		
	0.1863	1.6171		
	0.1856	1.6178	0.1846	1.6189
	0.1850	1.6184	0.1846	1.6189
	0.1847	1.6187		
	0.1825	1.6209	0.1827	1.6208
$^7F_2$	0.1079	1.6955	0.1061	1.6974
	0.1025	1.7009	0.1016	1.7019
	0.1000	1.7034	0.0998	1.7037
	0.0977	1.7057	0.0982	1.7053
	0.0971	1.7063	0.0974	1.7061
$^7F_1$	0.0424	1.761	0.0414	1.7621
	0.0359	1.7675	0.0361	1.7674
	0.0301	1.7733	0.031	1.7725
$^7F_0$	0	1.8034	0	1.8035

Table 5.3: Energy levels of Sm^{2+} in $BaCl_2$ and $BaBr_2$ reported by Lauer et al. [46] and transition energies from the $^5D_0$ state to the according ^7F-states. All values are given in eV.

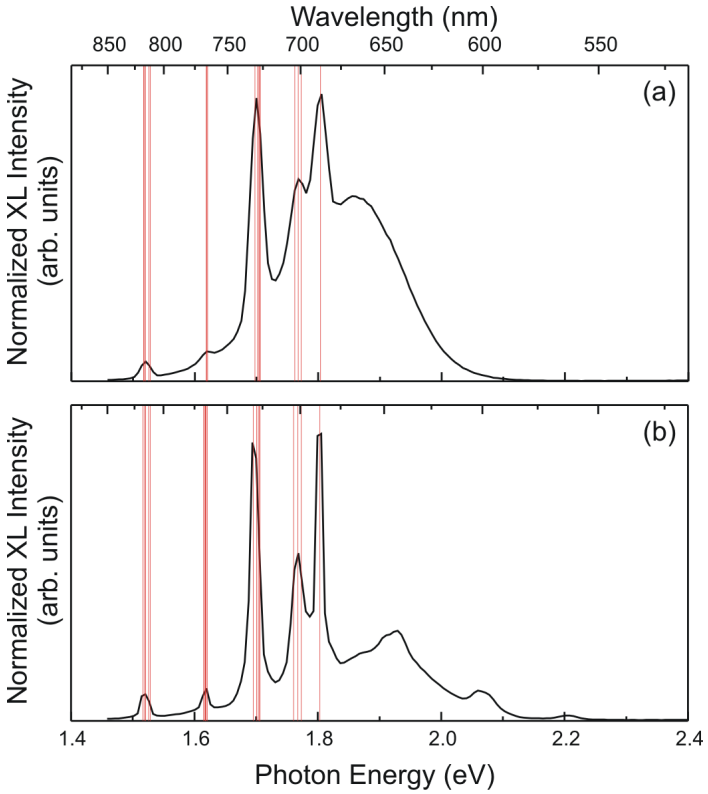

Figure 5.1: Normalized XL spectra of (a) $BaCl_2$:Sm^{2+} and (b) $BaBr_2$:Sm^{2+}. The red lines denote the calculated transition energies.

Figure 5.1a and b show the XL spectra of Sm-doped $BaCl_2$ and $BaBr_2$, respectively. The red lines denote the calculated transition energies (Table 5.3). It can be seen that the theoretical values agree well with the measured ones. Some transition energies are near by and can not be separated in the measurement. Figure 5.2a and b show the PL and PL excitation spectra of Sm-doped $BaCl_2$ and $BaBr_2$, respectively. The PL spectrum of $BaCl_2$:Sm^{2+} was excited at 545 nm and the excitation spectrum was recorded at 700 nm. The PL spectrum $BaBr_2$:Sm^{2+} was excited at 550 nm and the excitation spectrum was recorded at 700 nm. The spectra show line as well as band emissions.

Figure 5.3 shows the XL spectra of Sm-doped FBZ glass ceramics (a) and the XL spectra of Sm-doped $BaBr_2$ single crystal (b). It can be seen that the spectra are similar. The broad bands at 600 and 650 nm can not be observed in the spectrum of the single crystal. These two bands can be attributed to trivalent Sm. The Sm^{3+} emission are transitions from the $^4G_{5/2}$ level to the ground state $^6H_{5/2}$ [45]. Small changes among the spectra of the glass ceramics can be observed. The peak at 600 nm first increases from the initial sample to that annealed at 260°C and then decreases in the spectra of the sample annealed at 280°C. The peak at 650 nm decreases continuous from the initial sample to the sample annealed at 290°C. Compared to the single crystals the emission intensity is much lower. The dashed lines are a guide to the eyes to compare the line emissions of the single crystal to that of the glass ceramics.

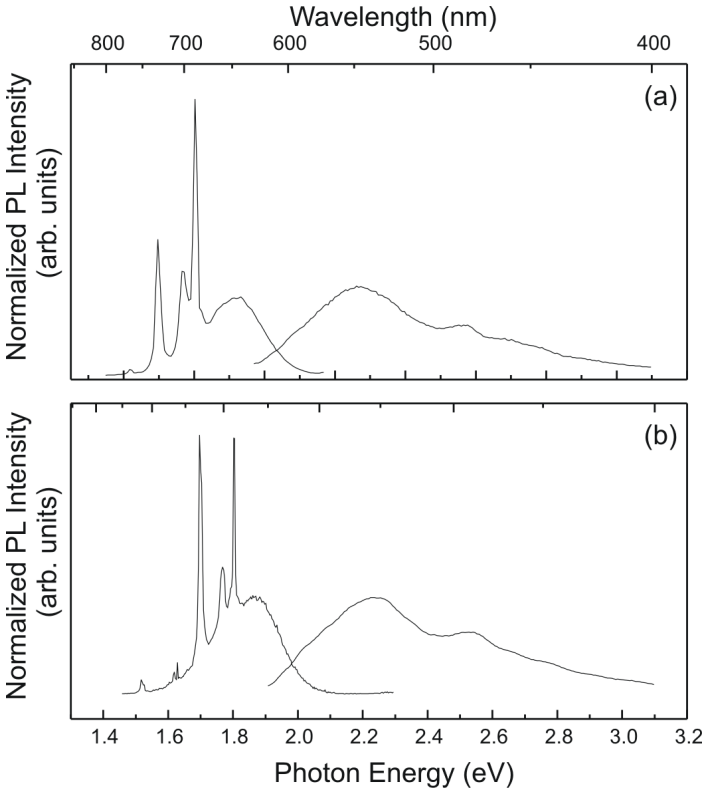

Figure 5.2: PL and PL excitation spectra of (a) $BaCl_2$:Sm^{2+} and (b) $BaBr_2$:Sm^{2+}. The PL spectrum of $BaCl_2$:Sm^{2+} was excited at 545 m and the excitation spectrum was recorded at 700 nm. The PL spectrum of $BaBr_2$:Sm^{2+} was excited at 550 nm and the excitation spectrum was recorded at 700 nm.

Figure 5.4 shows the PL and PL excitation spectra of the Sm-doped FBZ glass ceramics. All PL excitation spectra were recorded at 700 nm. The PL spectrum of the initial glass was excited at 555 nm, the spectra of the glass ceramics annealed at 260°C, 270°C, and 280°C were excited at 585 nm, and the PL spectra of the glass ceramics annealed at 285°C and 290°C were excited at 575 nm. The excitation wavelengths correspond to the maximum of the excitation spectrum of each sample.

A possible application for the Sm-doped glass ceramics can be for dual energy. Therefore a Sm-doped and an Eu-doped glass ceramics are combined. Since the Eu-doped samples are transparent and show a more intense luminescence signal than the Sm-doped sample is facing the x-ray source. Emission spectra were recorded for different x-ray energies. Figure 5.5 shows the dual energy spectra of a combination of a Sm-doped FBZ and Eu-doped FCZ glass ceramics for energies of 40, 50, and 60 kV of the x-rays. A change in the spectra can be observed. The Eu luminescence at 402 and 480 nm increases with increasing energy of the x-rays.

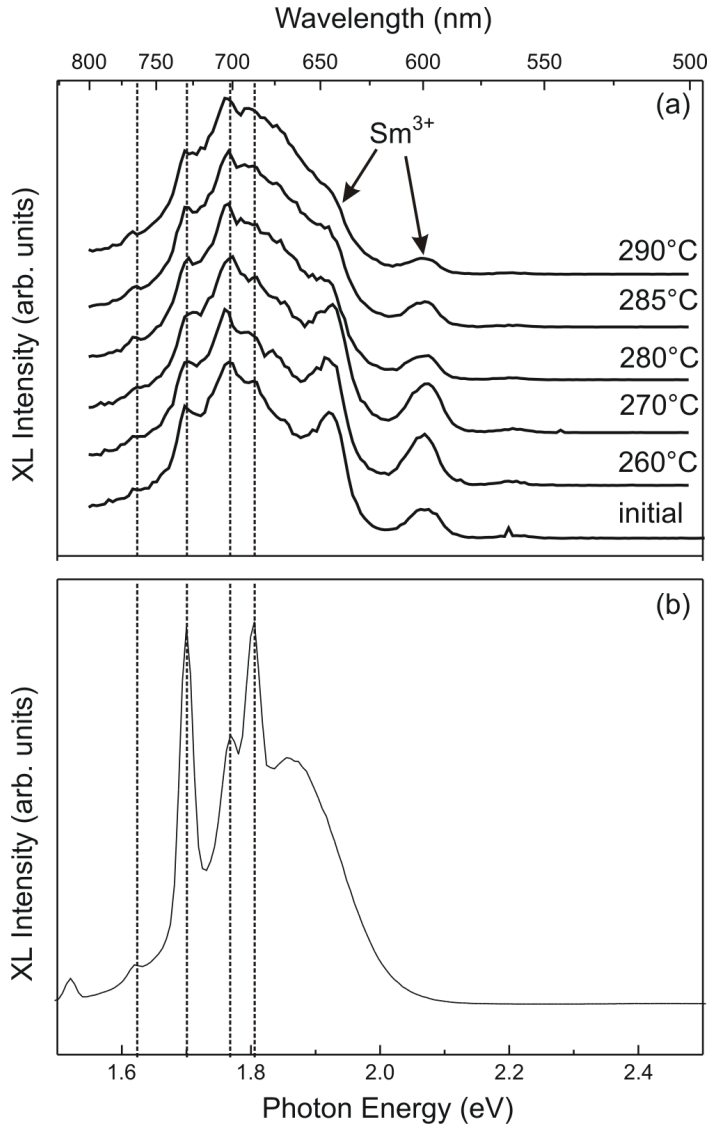

Figure 5.3: XL spectra of (a) Sm-doped FBZ glass ceramics and (b) $BaBr_2$:Sm^{2+} single crystals.

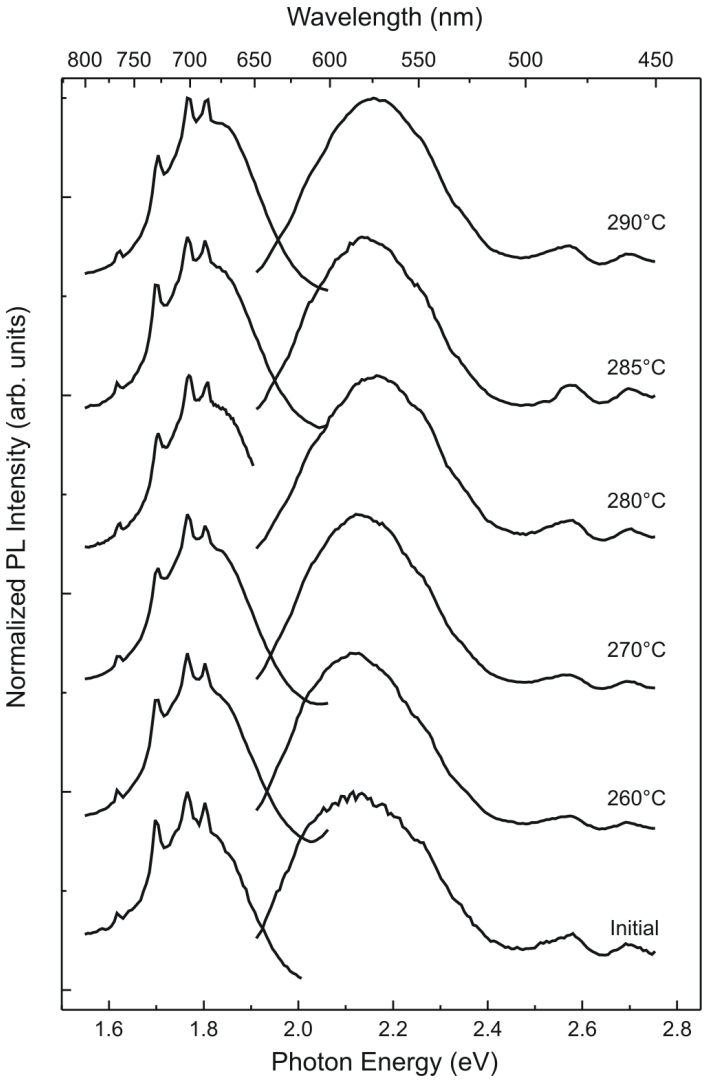

Figure 5.4: PL and Pl excitation spectra of Sm-doped FBZ glass ceramics. All PL excitation spectra were recorded at 700 nm. The PL spectrum of the initial glass was excited at 555 nm, the spectra of the glass ceramics annealed at 260°, 270°, and 280° were excited at 585 nm, and the PL spectra of the glass ceramics annealed at 285° and 290° were excited at 575 nm.

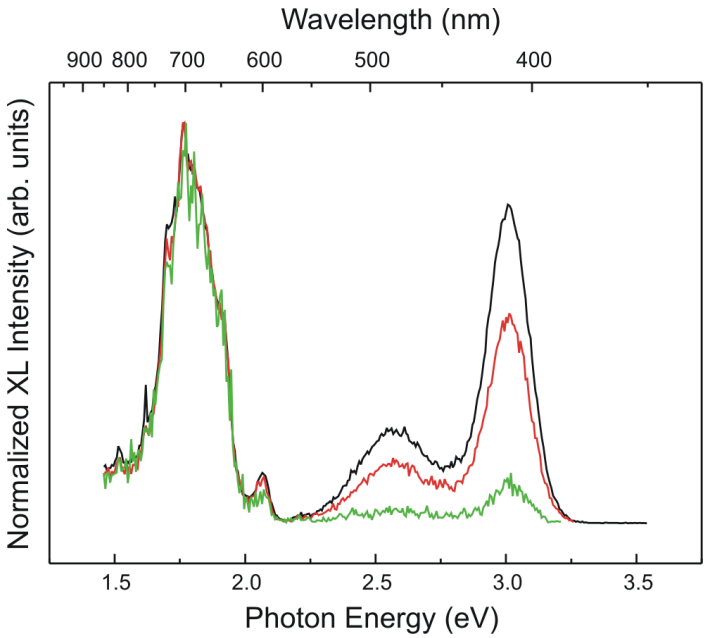

Figure 5.5: Normalized XL spectra of dual energy measurements of a combination of a Sm-doped FBZ and Eu-doped FCZ glass ceramics for x-ray energies of 40 (green curve), 50 (red curve), and 60 kV (black curve).

3.2 Mn-doped samples

Figure 5.6 show the XL spectra of Mn-doped $BaCl_2$ and $BaBr_2$. The peak around 700 nm is the Mn luminescence. The bands at 420 and 480 nm are the host lattice luminescence (Chapter 4). The spectrum of Mn-doped $BaBr_2$ shows an additional shoulder around 600 nm and is dominated by the host lattice luminescence. That of the Mn-doped $BaCl_2$ is dominated by the Mn luminescence.

The PL signal of Mn-doped crystals was to weak to record a PL or PL excitation spectrum. Fortunately, the PL and PL excitation spectra could be recorded in the laboratories of Schott AG (Mainz, Germany). Figure 5.7a and b shows the PL and PL excitation spectra of Mn-doped $BaCl_2$ and $BaBr_2$, respectively. The PL spectrum $BaCl_2$:Mn^{2+} was excited at 420 nm and the excitation spectrum was recorded at 670 nm. The PL spectrum $BaBr_2$:Mn^{2+} was excited at 425 nm and the excitation spectrum was recorded at 680 nm.

Figure 5.8 shows the XL spectra of the Mn-doped FCZ glass ceramics. All spectra show a weak shoulder around 700 nm where the Mn luminescence is expected to be. The spectra of the initial sample shows one intense peak at 623 nm and a very weak one at 415 nm. The sample annealed at 260°C shows a peak at 610 nm and to broad bands at 485 and 425 nm. The peak and the broad bands can also be observed in the spectrum of the 270°C sample.

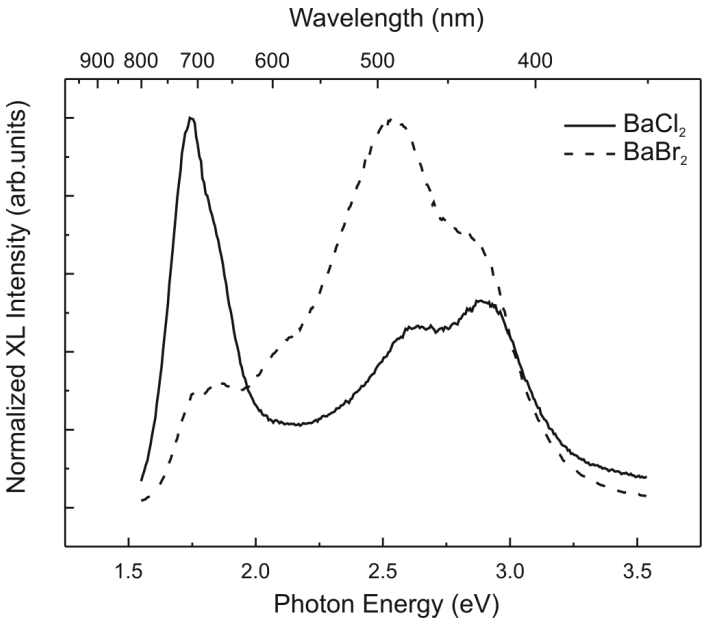

Figure 5.6: PL spectra of Mn-doped $BaCl_2$ (solid curve) and $BaBr_2$ (dashed curve).

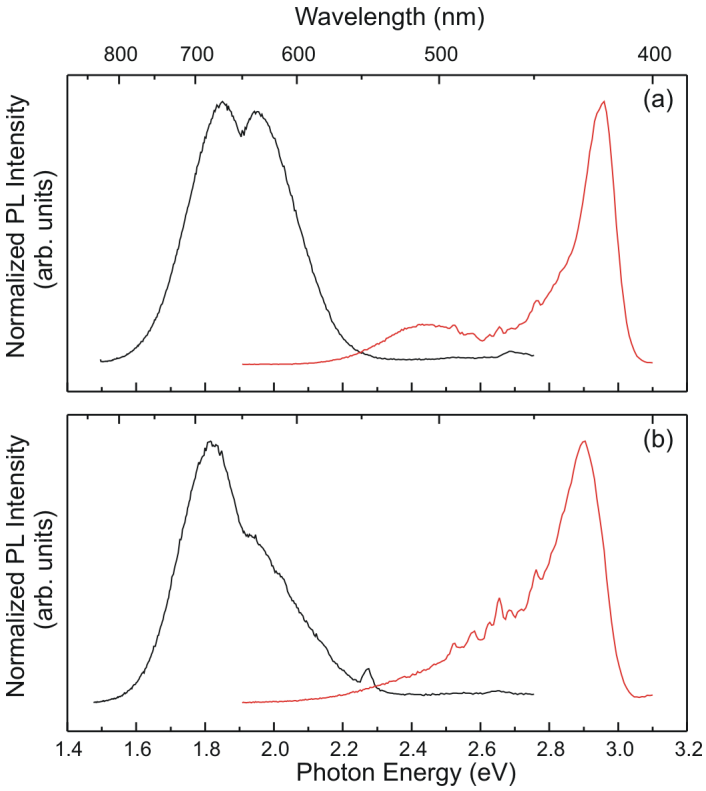

Figure 5.7: PL and PL excitation spectra of (a) Mn-doped $BaCl_2$ and (b) Mn-doped $BaCl_2$. The PL spectrum $BaCl_2$:Mn^{2+} was excited at 420 nm and the excitation spectrum was recorded at 670 nm. The PL spectrum $BaBr_2$:Mn^{2+} was excited at 425 nm and the excitation spectrum was recorded at 680 nm.

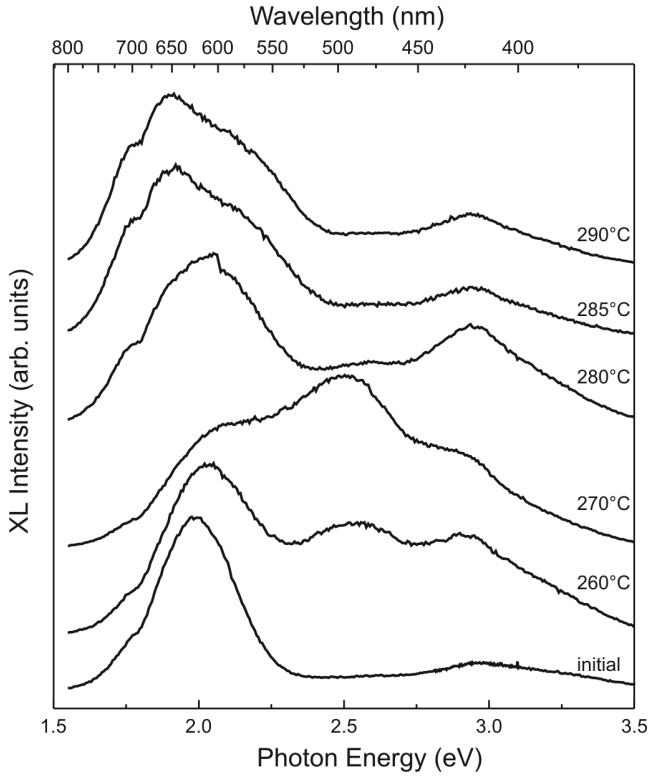

Figure 5.8: XL spectra of Mn-doped ZBLAN glass ceramics.

The intensity ratio has changed in favor to the band at 485 nm. The 280°C sample shows a broad peak at 615 nm and two weak bands at 475 and 420 nm. The spectra of the 285°C and 290°C sample are dominated by a broad band around 650 nm and have a weak band around 420 nm. The bands around 480 and 420 nm can be attributed to luminescence of undoped $BaCl_2$ crystals. Since the Mn luminescence in $BaCl_2$ single crystals is at 700 nm it is not clear what effects the luminescence in the region between 600-650 nm in the glass ceramics. Since the PL signal of the Mn-doped glasses was extremely weak no PL spectra can be shown.

With the help of EPR measurements it may be possible to distinguish between manganese ions in the glass matrix and in the nanocrystals. Divalent manganese has a ${}^6S_{5/2}$ ground state with fife unpaired electrons ($S = 5/2$). The spin Hamiltonian for a Mn^{2+} in an orthorhombic crystalline field is given by:

$$\begin{aligned}\mathscr{H} = g \cdot \mu_B \cdot \vec{S} \cdot \vec{B} \quad &+ \quad \frac{1}{3}(b_2^0\hat{O}_2^0 + b_2^2\hat{O}_2^2 + c_2^2\hat{O}_2^2) \\ &+ \quad \frac{1}{60}(b_4^0\hat{O}_4^0 + b_4^2\hat{O}_4^2 + c_4^2\hat{O}_4^2 + b_4^4\hat{O}_4^4 + c_4^4\hat{O}_4^4) \\ &+ \quad \frac{1}{1260}(b_6^0\hat{O}_6^0 + b_6^2\hat{O}_6^2 + c_6^2\hat{O}_6^2 + b_6^4\hat{O}_6^4 + c_6^4\hat{O}_6^4 + b_6^6\hat{O}_6^6 + c_6^6\hat{O}_6^6) \\ &+ \quad A \cdot \vec{S} \cdot \vec{I} \end{aligned} \tag{5.1}$$

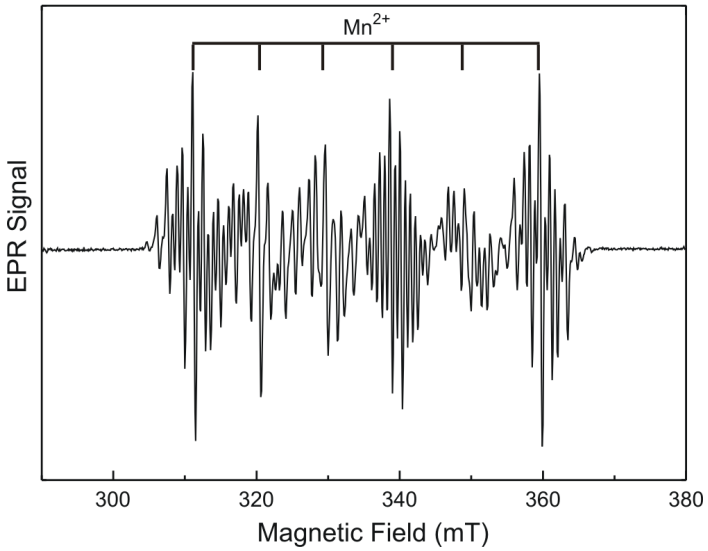

Figure 5.9: EPR spectra of Mn-doped $BaCl_2$ single crystal.

where the first term is due to the Zeeman interaction and the next three terms take into account the electric field at the Mn^{2+} site; these four terms are responsible for the fine structure in the EPR spectra. The last term is the interaction between the electron spin and the nuclear spin, which produces the hyperfine structure. Usually the Mn^{2+} spectrum is domiated by the hyperfine structure since the hyperfine interaction is bigger than the fine structure. The characteristic hyperfine structure of manganese is simple to recognize it has six nearly equidistant lines with nearly the same intensity.

Figure 5.9 shows an EPR spectrum of manganese doped $BaCl_2$ single crystal. The spectrum consists of six groups of lines according to an hyperfine splitting of 10 mT. Each group contains a number of super hyperfine lines. The hyperfine splitting indicated that we are dealing with a Mn(I) center [47]. This means that the Mn^{2+} is substituted on a Ba site. The hyperfine lines are influenced by the nine surrounding Cl atoms. Cl has two naturally occurring isotopes, ^{35}Cl (75.77 %) and ^{37}Cl (24.23 %) with $I = 3/2$.

Figure 5.10 shows the EPR spectra of the Mn-doped FCZ glass and glass ceramics. Beside the big resonance dip a structure with small dips at 309, 318, 344, and 353 mT can be observes. The structure is more intense in the initial sample and decreases from the 260° to 290° glass ceramic. The four lines denote the position of the small bands which can be observed in the initial sample. It can be seen that the structure which is caused by the Mn-doping decreases with increasing annealing temperatures. The position of the small dips changes in the samples annealed at 285°C and 290°C.

Unfortunately, with this information it is not possible to distinguish between Mn ions in the glass matrix and in the nanocrystals or to make any other conclusions.

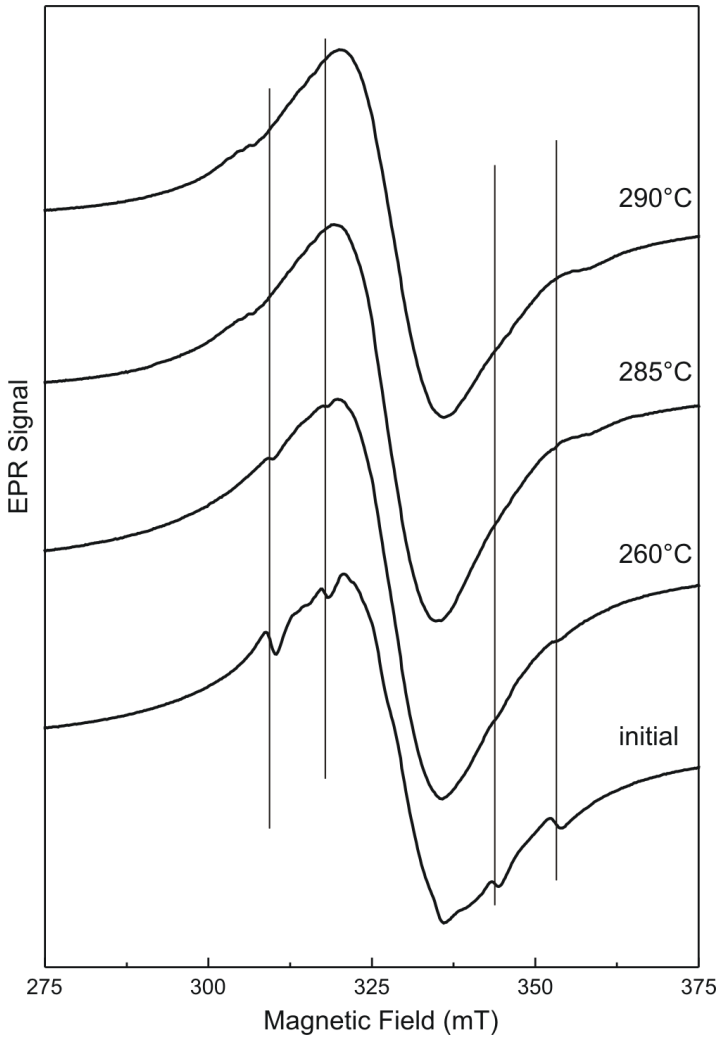

Figure 5.10: EPR spectra of initial and 290 Mn-doped Glass-ceramics.

4 Discussion

For a rating of the scintillation properties with regard to integral x-ray scintillation efficiency the four barium halide single crystals were compared to the common scintillator $CdWO_4$. The measurements were made using the same parameters for all crystals. The area under the XL curve is calculated and compared to that of a $CdWO_4$ reference sample (28,000 ph/MeV) [37]. The efficiency of $CdWO_4$ was set to 100%. Table 5.4 shows the efficiencies of the investigated crystals. The chlorine crystals show a very weak scintillation efficiency. The bromine crystals show a promising efficiency. The scintillation efficiency of the manganese doped $BaBr_2$ crystal is dominated by the host lattice luminescence.

Crystal	Integral x-ray scintillation efficiency with respect to $CdWO_4$	
	(%)	(photons/ MeV)
$CdWO_4$	100	28,000
$BaCl_2$:Sm^{2+}	9	2,540
$BaBr_2$:Sm^{2+}	222	62,200
$BaCl_2$:Mn^{2+}	10	2,800
$BaBr_2$:Mn^{2+}	114	32,100

Table 5.4: Integral x-ray scintillation efficiency with respect to $CdWO_4$ of Sm- and Mn-doped BaX_2 (X= Cl, Br) given in % and photons/ MeV. The x-ray scintillation efficiency was derived by comparing the integrated area under the XL curve of the corresponding barium halide to that of a $CdWO_4$ reference sample.

The Sm-doped glass ceramics may be good fluorescence standards. The emission spectra show both line and band emission. The single crystals are hygroscopic and therefore not good as a fluorescence standard. Unfortunately, we had problems to reproduce the glass ceramic. Only in the first sample we had divalent samarium in the glass. It was not possible to reduce the trivalent samarium. The trivalent samarium may be good for other applications, but this will not be the topic. Since the scintillation efficiency is not high enough the single use as a scintillator is not promising. The divalent samarium in combination with Eu-doped glasses can be used for dual energy applications. The XL spectra change with different x-ray energies. The Eu luminescence increases regarding to the Sm luminescence with increasing x-ray energy.

The manganese doped samples show a weak scintillation signal, also the PL signal was extremely weak. The PL spectra show no line emission, which makes the samples not very useful as a fluorescence standards. The Mn doped $BaBr_2$ with 32,100 pho/MeV has a good x-ray scintillation efficiency. The XL spectrum is dominated by the host lattice luminescence. The x-ray scintillation efficiency of an undoped $BaBr_2$ crystal is with 8,700 photons/MeV much lower. It seem that the manganese doping has an effect on the x-ray intensity and/or the afterglow.

6 Electron Paramagnetic Resonance on Eu-doped BaX_2

EPR measurements on Eu-doped $BaCl_2$ and Eu-doped $BaBr_2$ have already been carried out by Wever and den Hartog [7] and Schweizer et al. [8], respectively. Both EPR spectra show similar features: for a general direction of the magnetic field the Eu^{2+} spectrum essentially consists of two sets of seven fine structure lines (Figure 6.1). Each of these lines has a hyperfine splitting of approximately 12 lines. Eu^{2+} has an $S = 7/2$ ground state and two stable isotopes: ^{151}Eu with $I = 5/2$ and 47.82% abundance and ^{153}Eu with $I = 5/2$ and 52.18% abundance. Each Eu isotope thus gives rise to a hyperfine structure of 6 lines; since the two nuclear g factors differ significantly so do the hyperfine interactions ($g_n(^{151}\mathrm{Eu}) = 1.389$, $g_n(^{153}\mathrm{Eu}) = 0.6134$), and consequently the two sextets are clearly resolved.

Wever and den Hartog [7] and Schweizer et al. [8] used different coordinate systems. While Wever and den Hartog [7] chooses the space group *Pbnm* for the unit cell (lattice parameters of $BaCl_2$: $a = 9.333$ Å, $b = 7.823$ Å, and $c = 4.705$ Å), Schweizer et al. [8] chooses the space group *Pnma* (lattice parameters of $BaBr_2$: $a = 8.276$ Å, $b = 4.956$ Å, and $c = 9.919$ Å). The c-axis of Schweizer et al. corresponds to the a-axis of Wever and den Hartog.

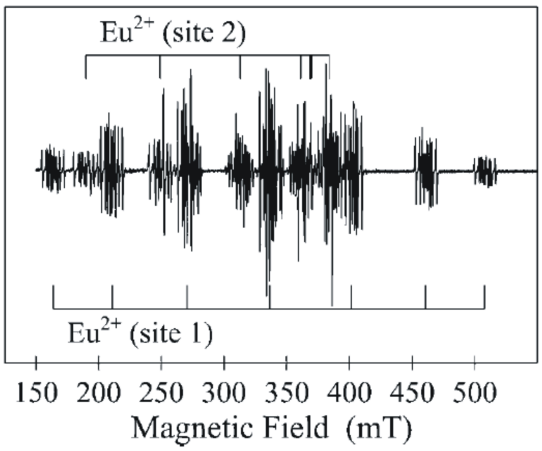

Figure 6.1: EPR spectrum of Eu^{2+} in a $BaBr_2$ single crystal for a general direction of the magnetic field B in the ac plane making an angle of 13° with the c direction, recorded at 20 K in X-band (9.37 GHz). The spectrum is taken from [8].

host lattice	g	b_2^{0*}	b_2^{2*}	b_2^{0*}/b_2^{2*}	φ_0	^{151}A	reference
$BaCl_2$	–	33	-467	-0.0707	15.5°	-	[7]
$BaBr_2$	1.990	-57.3	518.1	-0.1106	18°	-31.0	[8]

Table 6.1: Parameter values b_2^{0*}, b_2^{2*}, and A for Eu^{2+} in $BaCl_2$ and $BaBr_2$. The values are given in units of 10^{-4} cm^{-1}. The principal axis z of the fine structure tensor D is along the crystal c-axis. The angle φ_0 is measured between the $x(y)$-axis of the D tensor and the crystal $a(b)$-axis.

As shown by the analysis the Eu^{2+} centre in $BaCl_2$ and $BaBr_2$ single crystals has C_S symmetry. The ground state of Eu^{2+} is a pure S-state ($L = 0$) with an isotropic g value very close to the g_e value of the free electron. The spin Hamiltonian of this symmetry is given by:

$$\begin{aligned}\mathscr{H} = g \cdot \mu_B \cdot \vec{S} \cdot \vec{B} \quad &+ \quad \frac{1}{3}(b_2^0\hat{O}_2^0 + b_2^2\hat{O}_2^2 + c_2^2\hat{O}_2^2) \\ &+ \quad \frac{1}{60}(b_4^0\hat{O}_4^0 + b_4^2\hat{O}_4^2 + c_4^2\hat{O}_4^2 + b_4^4\hat{O}_4^4 + c_4^4\hat{O}_4^4) \\ &+ \quad \frac{1}{1260}(b_6^0\hat{O}_6^0 + b_6^2\hat{O}_6^2 + c_6^2\hat{O}_6^2 + b_6^4\hat{O}_6^4 + c_6^4\hat{O}_6^4 + b_6^6\hat{O}_6^6 + c_6^6\hat{O}_6^6) \\ &+ \quad A \cdot \vec{S} \cdot \vec{I} \end{aligned} \tag{6.1}$$

where g is the isotropic g value, A the isotropic hyperfine constant of the ^{151}Eu or the ^{153}Eu isotope, the $\hat{O}_k^q$ are the Stevens operators and the b_k^q the Stevens parameters [48]. μ_B is the Bohr magneton and $\vec{S}$ is the electron spin operator. The obtained g and A values, φ_0, and the fine-structure parameters for $BaCl_2$ and $BaBr_2$ are collected in Table 6.1.

Wever and den Hartog [7] also calculated the crystal field of $BaCl_2$. In the following section the calculation of the crystal field will be explained and the theoretical values for $BaBr_2$ and BaI_2 will be given.

1 Crystal field calculation

The crystal field parameters have been calculated on the basis of a point-ion lattice approximation. The crystal field potential at a certain origin $\vec{r}(x, y, z)$ is given by:

$$V(\vec{r}) = \frac{1}{4\pi\epsilon_0} \sum_j{}' \frac{q_j}{\left|\vec{R}'_j - \vec{r}\right|} \tag{6.2}$$

where q_j is the charge of the j-th ion in the lattice and $\overrightarrow{R}_j$ is the position of the j-th ion in the lattice.

The lattice summation is expanded into a series of spherical harmonics $Y_l^m(\vartheta, \varphi)$. Considering only second degree contributions $Y_2^m (m = -2, 0, +2)$ the crystal field in the neighbourhood of the origin can be expressed by:

$$V_2(\vec{r}') = c_2^{0\prime}(3z'^2 - r'^2) + c_2^{2\prime}(x'^2 - y'^2) + c_2^{-2\prime}(2x'y'), \tag{6.3}$$

$$V_2(\vec{r}) = c_2^0(3z^2 - r^2) + c_2^2(x^2 - y^2) \tag{6.4}$$

where x', y', z' and x, y, z are along the crystallographic and second degree principal axes, respectively. Here z' and z are parallel and the angle between x' and x is determined by the relationship:

$$\tan(\varphi_0) = \frac{c_2^{-2\prime}}{c_2^{2\prime}}. \tag{6.5}$$

The crystal field parameter are:

$$\begin{aligned} c_2^{0\prime} &= \frac{1}{16\pi\epsilon_0} \sum_j{}' \frac{q_j}{\vec{R}_j'^5} \left(3\vec{Z}_j'^2 - \vec{R}_j'^2\right), \\ c_2^{2\prime} &= \frac{3}{16\pi\epsilon_0} \sum_j{}' \frac{q_j}{\vec{R}_j'^5} \left(\vec{X}_j'^2 - \vec{Y}_j'^2\right), \\ c_2^{-2\prime} &= \frac{3}{16\pi\epsilon_0} \sum_j{}' \frac{q_j}{\vec{R}_j'^5} \left(2\vec{X}_j'\vec{Y}_j'\right). \end{aligned} \tag{6.6}$$

Here X', Y', Z', and R' are associated with the positions of the ions in the lattice [28], which can be calculated from x-ray data on the unit cell position (Table 6.2). Figure 6.2 shows the orthorhombic BaX_2 structure projected onto the *ab* symmetry plane, the distances are listed in Table 6.3. In order to change equations for the crystal field parameters in such a way that x, y, and z are along the principle directions of the total crystal field ($c_2^{-2} \equiv 0$) a rotation about the z' axis by an angle φ_0 is carried out.

Wever and den Hartog [7] have assumed that in $BaCl_2$ the ions are located at the same position as in $PbCl_2$ except for a uniform expansion correction. For the calculations described in this work different sets of atomic positions were used (for details see Table 6.4).

In the following an example of the calculation of the lattice sum c_2^0 for $BaCl_2$ is given. The calculation was carried out using following formula:

$$c_2^0 = \frac{1}{16\pi\varepsilon_0} \Sigma_j \frac{q_j}{R_j^5}(3Z_j^2 - R_j^2) \tag{6.7}$$

Ba-X

The first interatomic distance is between a Ba ion and a Cl_I ion.

$$\begin{aligned} a_1 &= \frac{2e}{2.86^5} * (3 * 0.1209^2 - 2.86^2) \\ a_2 &= \frac{-e}{2.86^5} * (3 * 0.4130^2 - 2.86^2) \end{aligned}$$

		$BaCl_2$	$BaBr_2$	BaI_2
	a	9.421	9.919	10.695
	b	7.865	8.276	8.922
	c	4.731	4.956	5.304
Ba				
	x	0.2514	0.2447	0.2366
	y	0.2500	0.2500	0.2500
	z	0.1209	0.1149	0.1215
X_I				
	x	0.1504	0.1422	0.1393
	y	0.2500	0.2500	0.2500
	z	0.4130	0.4272	0.4265
X_{II}				
	x	0.0290	0.0284	0.0.290
	y	0.2500	0.2500	0.2500
	z	0.8392	0.8401	0.8387

Table 6.2: Lattice parameters (space group *Pbnm*) and atomic positions of $BaCl_2$, $BaBr_2$, and BaI_2 [28]. All values are given in Å.

The next interatomic distance is between a Ba ion and a Cl_{II} ion.

$$\begin{aligned} b_1 &= \frac{2e}{3.15^5} * (3 * 0.1209^2 - 3.15^2) \\ b_2 &= \frac{-e}{3.15^5} * (3 * 0.8392^2 - 3.15^2) \end{aligned}$$

The third interatomic distance is between a Ba ion and a Cl_{II} ion.

$$\begin{aligned} c_1 &= \frac{2e}{3.18^5} * (3 * 0.1209^2 - 3.18^2) \\ c_2 &= \frac{-e}{3.18^5} * (3 * 0.8392^2 - 3.18^2) \end{aligned}$$

The fourth interatomic distance is between a Ba ion and a Cl_I ion with a quantity of two.

$$\begin{aligned} d_1 &= \frac{4e}{3.17^5} * (3 * 0.1209^2 - 3.17^2) \\ d_2 &= \frac{-2e}{3.17^5} * (3 * 0.4130^2 - 3.17^2) \end{aligned}$$

The fifth interatomic distance is between a Ba ion and a Cl_I ion with a quantity of two.

$$\begin{aligned} e_1 &= \frac{4e}{3.25^5} * (3 * 0.1209^2 - 3.25^2) \\ e_2 &= \frac{-2e}{3.25^5} * (3 * 0.4130^2 - 3.25^2) \end{aligned}$$

Interaction Ba-X	No. of equiv. distances	$BaCl_2$	$BaBr_2$	BaI_2
	1	2.86	3.21	3.38
in same plane	1	3.15	3.32	3.63
	1	3.18	3.26	3.55
	2	3.17	3.24	3.55
out of plane	2	3.25	3.38	3.58
	2	3.58	3.83	4.10
X_I-X_I				
out of plane	2	3.73	3.71	3.96
X_{II}-X_{II}				
out of plane	2	3.87	4.05	4.38
X_I-X_{II}				
out of plane	2	3.64	3.89	4.16
	2	3.53	3.78	4.08
in plane	1	3.78	3.94	4.29

Table 6.3: Interatomic distances in $BaCl_2$, $BaBr_2$, and BaI_2 in Å.

The fifth interatomic distance is between a Ba ion and a Cl_{II} ion with a quantity of two.

$$\begin{aligned} f_1 &= \frac{4e}{3.58^5} * (3 * 0.1209^2 - 3.58^2) \\ f_2 &= \frac{-2e}{3.58^5} * (3 * 0.8392^2 - 3.58^2) \end{aligned}$$

$\mathbf{X_I}$-$\mathbf{X_I}$

There is only one distance between a Cl_I ion and another Cl_I ion with a quantity of two. For both ions the equations are the same, therefore a factor of two was insert.

$$g = \frac{-4e}{3.73^5} * (3 * 0.4130^2 - 3.73^2) \tag{6.8}$$

$\mathbf{X_{II}}$-$\mathbf{X_I}$

Between a Cl_{II} ion and another Cl_{II} ion there exist also two equivalent interatomic distances. For both ions the equations is the same, therefore it is multiplied by two.

$$h = \frac{-4e}{3.87^5} * (3 * 0.8392^2 - 3.87^2) \tag{6.9}$$

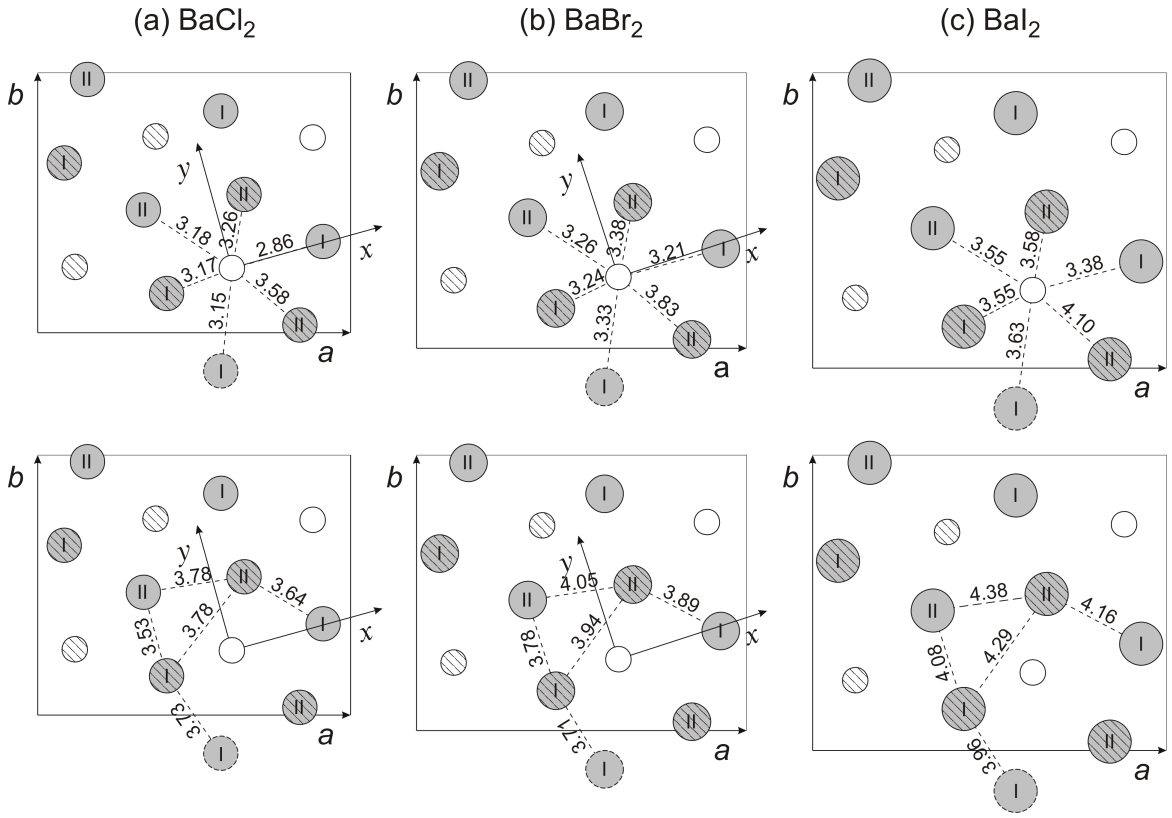

Figure 6.2: Lattice structure of orthorhombic BaX_2 projected onto the *ab* symmetry plane. The small white circles denote the Ba^{2+} ions and the large grey circles denote the X^- ions. The hatched circles lie in a different mirror plane than the non-hatched ones.

$\mathbf{X}_I$-$\mathbf{X}_{II}$

Between a Cl_I ion and a Cl_{II} ion there are three different interatomic distances. Two of them can be found twice.

$$
\begin{aligned}
i_1 &= \frac{-2e}{3.64^5} * (3 * 0.8392^2 - 3.64^2) \\
i_2 &= \frac{-2e}{3.64^5} * (3 * 0.4130^2 - 3.64^2) \\
j_1 &= \frac{-2e}{3.53^5} * (3 * 0.8392^2 - 3.53^2) \\
j_2 &= \frac{-2e}{3.53^5} * (3 * 0.4130^2 - 3.53^2) \\
k_1 &= \frac{-1e}{3.78^5} * (3 * 0.8392^2 - 3.78^2) \\
k_2 &= \frac{-1e}{3.78^5} * (3 * 0.4130^2 - 3.78^2)
\end{aligned}
$$

host lattice	c_2^0	c_2^2	c_2^0/c_2^2	φ_0	atomic positions
$BaCl_2$	7.8778	-21.3096	-0.3697	12.21°	$BaCl_2$ [28]
$BaBr_2$	3.0084	-13.9453	-0.2157	23.36°	$BaBr_2$ [28]
BaI_2	3.2510	-15.2328	-0.2134	25.91°	BaI_2 [28]
$BaCl_2$	2.8937	-9.8752	-0.2930	16.81°	
$BaBr_2$	2.6479	-8.6243	-0.3070	17.92°	$PbCl_2$ [49]
BaI_2	2.3388	-7.0984	-0.3295	19.55°	
$BaCl_2$	7.8778	-21.3096	-0.3697	12.21°	
$BaBr_2$	6.9999	-18.2636	-0.3833	12.40°	$BaCl_2$ [28]
BaI_2	5.9093	-14.5855	-0.4051	12.69°	
$BaCl_2$	3.2553	-16.1345	-0.2018	22.92°	
$BaBr_2$	3.0084	-13.9453	-0.2157	23.36°	$BaBr_2$ [28]
BaI_2	2.6903	-11.2778	-0.2386	24.01°	
$BaCl_2$	4.0380	-21.9722	-0.1838	24.95°	
$BaBr_2$	3.6899	-18.9315	-0.1949	25.33°	BaI_2 [28]
BaI_2	3.2510	-15.2328	-0.2134	25.91°	

Table 6.4: Theoretical values of c_2^0 and c_2^2 (in 10^{18} V/m^2) and φ_0 for $BaCl_2$, $BaBr_2$, and BaI_2. The unit cell constants were taken from [28], the atomic positions from the references indicated.

To get the final values the summation has to be done over all surrounding atoms. Table 6.4 shows the calculated values of c_2^0 and c_2^2 (in 10^{18} V/m^2) and φ_0 for $BaCl_2$, $BaBr_2$, and BaI_2 for different atomic positions. It can be seen that the choice of the atomic position has an influence on the calculated crystal field. With the real atomic positions (upper three rows in Table 6.4) the c_2^0/c_2^2 ratio decreases from $BaCl_2$ via $BaBr_2$ to BaI_2. The calculations with atomic positions and an uniform expansion correction yield a increasing c_2^0/c_2^2 ratio from $BaCl_2$ via $BaBr_2$ to BaI_2.

2 Preliminary EPR investigations on Eu-doped BaI_2

Figure 6.3 shows an EPR spectrum of Eu-doped BaI_2 for a general orientation of the magnetic field. The spectrum consists of two sets of seven fine structure lines each, as described in the introduction of this chapter.

Figure 6.4 shows the corresponding angular dependence of the EPR spectra. For the angular dependence the crystal was measured in three different planes (all perpendicular to each other). For each plane the crystal was rotated and measured in 5° steps. It can be seen that the intersection of the three different planes do not match. This indicates that the crystal is tilted with respect to the crystal axis planes. It was expected that BaI_2 has a

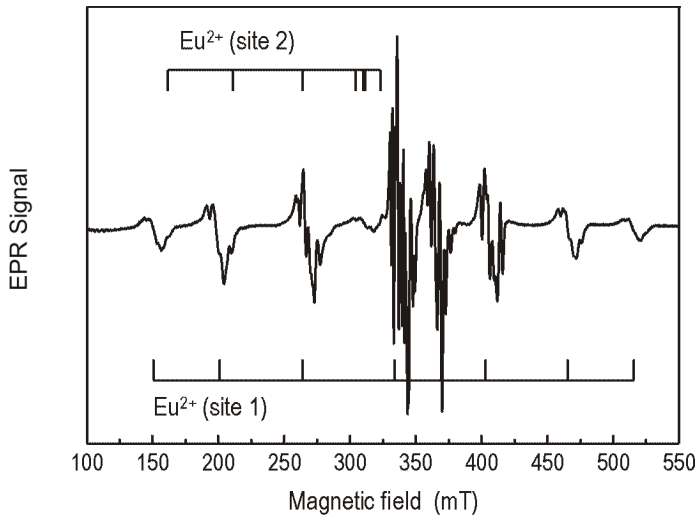

Figure 6.3: EPR spectrum of Eu^{2+} in a BaI_2 single crystal for a general direction of the magnetic field in the *ab* plane. For each plane the crystal was rotated and measured in 5° steps.

cleavage plane perpendicular to the crystallographic *c*-axis. Either the used cleavage plane is not perpendicular to any of the crystallographic axis. If the crystal is tilted in only one direction the analysis would still be possible. Since the analysis was not possible it seems that the crystal was heavily tilted. Unfortunately, the alignment of the crystal turned out to be not that easy. The crystal shows nearly no Laue reflections and is extremely hygroscopic. The Laue experiments are time-consuming: each x-ray film has to be developed and then analyzed. During this time the crystal is exposed to air. Therefore, the sample was embedded into glue to record the Laue photos. This leads to an even more decreased signal intensity of the reflections. Despite of a lot of attempts it was not possible to orientate the crystal properly. Since the alignment of the BaI_2 crystal was not possible the analysis was not possible either.

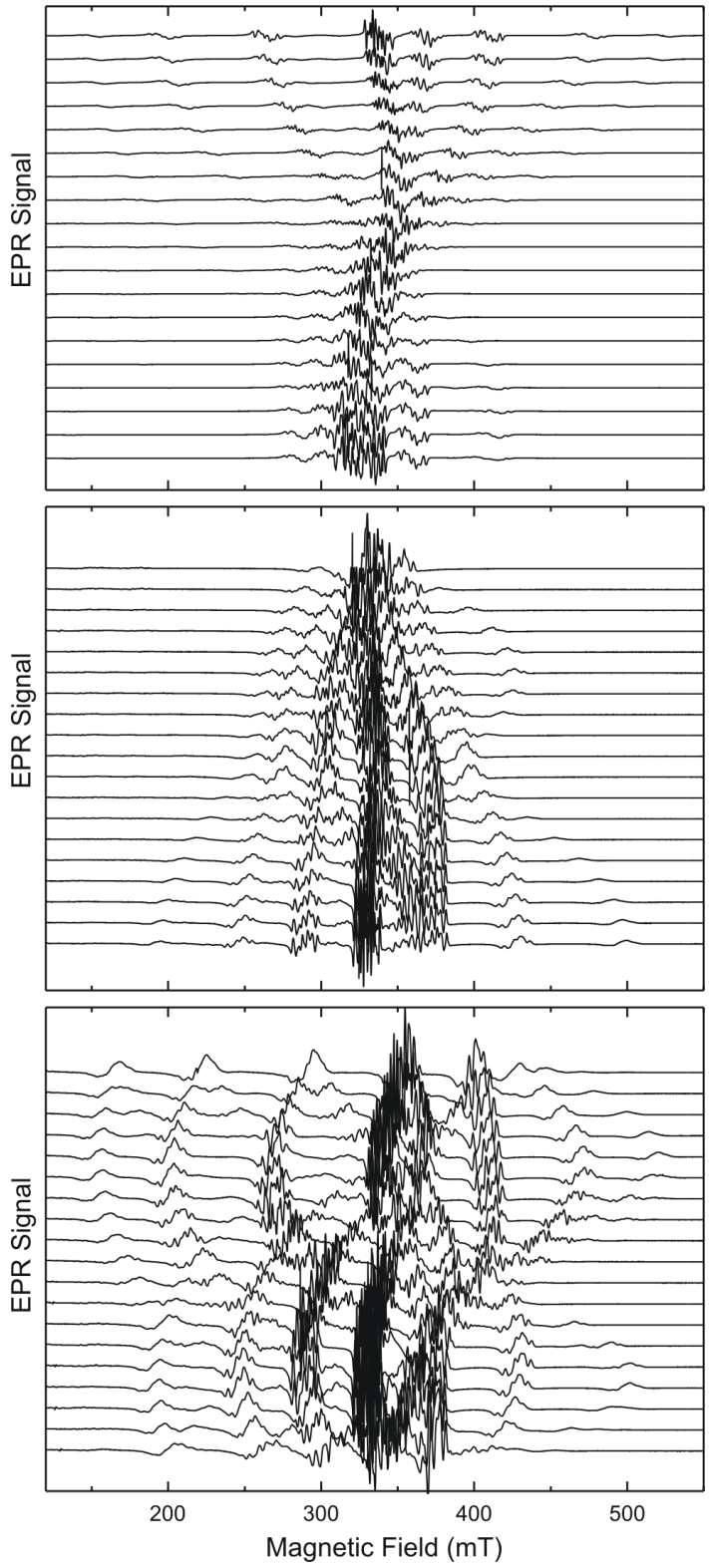

Figure 6.4: EPR angular dependence of Eu-doped BaI_2 for three different orientations.

7 ^{151}Eu-Mössbauer Spectroscopy on Eu-doped CaF_2, $BaCl_2$, and Glasses

Initially, the main focus of the Mössbauer investigations was set on the Eu-doped fluorochlorozirconate glass ceramics. The results of this investigation should help to improve the glass ceramics. The x-ray scintillation of the glass ceramics is due to Eu^{2+} ions embedded in the nanocrystals. It is known from x-ray luminescence measurements that Eu^{2+} in the glass shows no luminescence. In contrast to Eu^{2+}, Eu^{3+} ions show a weak luminescence in the glass. In the XL spectra a fraction of Eu^{3+} luminescence can be observed. This denotes that although the glass ceramics were doped with europium(II) fluoride (EuF_2) there can also be found a large fraction of Eu^{3+} in the glass. Probably, the divalent Eu is converted to trivalent Eu during the melting process. If one wants to optimize the glass ceramics it is important to optimize the Eu^{2+} / Eu^{3+} ratio in favor of the Eu^{2+}.

It is not possible to detect Eu^{3+} ions with EPR measurement. We want to be able to observe both Eu^{2+} and Eu^{3+} species plus subtle shifts between the Eu in the glass matrix and Eu in the nanocrystals. ^{151}Eu-Mössbauer spectroscopy provides an excellent method to detect and distinguish between di- and trivalent Eu. In addition the abundance ratio between the two valence states of Eu can also be determined. In order to distinguish between Eu^{2+} in the glass matrix and Eu^{2+} in the nanocrystals it is also necessary to measure Eu-doped $BaCl_2$ single crystals.

Since $BaCl_2$ is - because of its high absorption coefficient for the 21.64 keV γ-rays - not a very good host lattice for ^{151}Eu-Mössbauer spectroscopy, the first investigations were started with samples of Eu-doped CaF_2. CaF_2 is a very Mössbauer friendly host lattice with a well suited coefficient and very good to get a better understanding for Mössbauer spectra and their interpretation in these systems. Since some interesting new results were found during the measurements on Eu-doped CaF_2, these measurements and results are presented in the following.

1 Eu-doped CaF_2

In this section an overview on our investigations on Eu ions in a CaF_2 host lattice is given. CaF_2 has the fluorite structure. Figure 7.1 shows the crystal structure of CaF_2. This structure

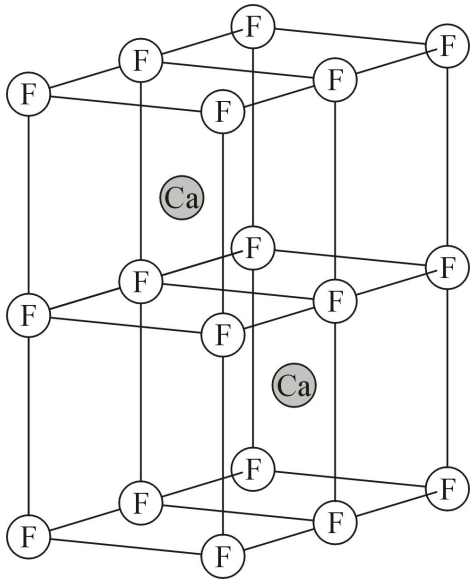

Figure 7.1: Crystal structure of CaF_2.

consist of the F ions forming a face-centered cubic (fcc) lattice while the Ca ions are placed in a simple cubic arrangement in the tetrahedral holes. Eu^{2+} ions substitute on the Ca^{2+} site. The local symmetry of the Eu^{2+} ion is cubic [50]. Two different samples of CaF_2 crystals were investigated: one doped with 2% and one with 0.1% Eu.

The core-polarization field of divalent Eu in CaF_2, calculated from the hyperfine constant is equal to (-340±1) kGauss ((-34.0 ± 0.1) T) [51]. In the presence of a magnetic hyperfine interaction the ^{151}Eu ground state is split into six levels and the excited state into eight levels. With the selection rule of the M1-transition $\Delta m_I = 0, \pm 1$, there are 18 different transitions (see Figure 7.2, upper part). Figure 7.2 (lower part) shows the idealized Mössbauer spectrum of ^{151}Eu in CaF_2 in the presence of a magnetic hyperfine field of 34 T, with an isomer shift of 0 mm/s and a reduced linewidth of 0.23 mm/s in order to resolve the absorption lines of all 18 transitions. The arrows denoting the transitions (upper part) are in a different order than those shown in Figure 2.8 to illustrate which transition (upper part) belongs to the corresponding absorption line (lower part). For the simulated spectrum the transition probabilities in Table 7.1 were used. The simulated spectrum as well as the transition probabilities show no magnetic polarization.

Dilute CaF_2:Eu^{2+} systems have previously been studied with paramagnetic resonance spectroscopy [52, 53] as well as ^{151}Eu-Mössbauer spectroscopy [54–58]. The paramagnetic splitting of Eu^{2+} in dilute crystals (0.1% Eu) has been determined at low temperature by EPR by Baker, Bleaney and Hayes [52] and the hyperfine interaction has been measured by electron nuclear double resonance (ENDOR) by Baker and Williams [53]. The first ^{151}Eu Mössbauer studies were performed later on more concentrated systems: Maletta et al. [54] and Wickmann et al. [55] studied systems with 0.5 to 10% Eu, reporting on a very anoma-

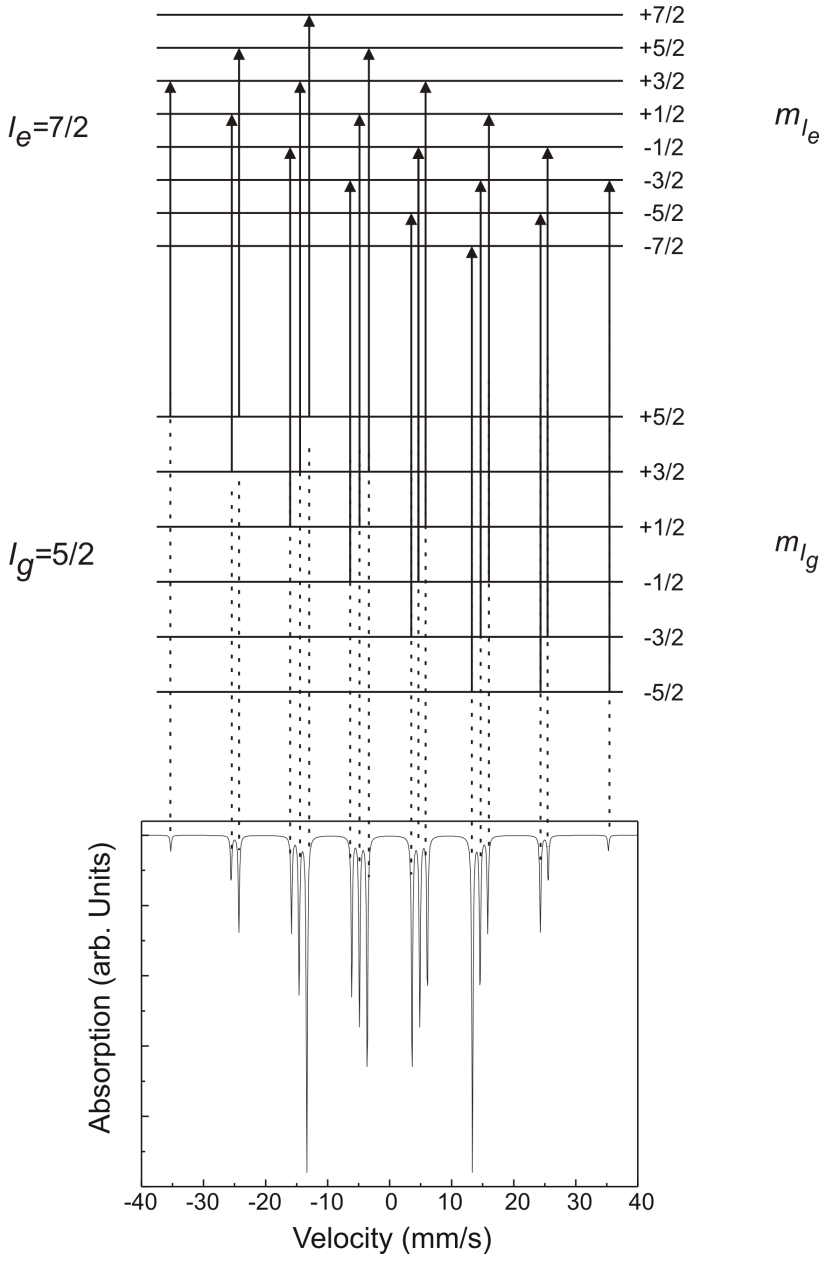

Figure 7.2: Nuclear energy levels for ^{151}Eu in the presence of a magnetic hyperfine field. The arrows denote the 18 allowed transitions with its resulting Mössbauer spectrum in the presence of a magnetic hyperfine field of 34 T, with an isomer shift of 0.0 mm/s and a reduced linewidth of 0.23 mm/s in order to resolve the absorption lines of all 18 transitions. The arrows denoting the transitions (upper part) are in a different order than those shown in Figure 2.8 to illustrate which transition (upper part) belongs to the corresponding absorption line (lower part). For the simulated spectrum the transition probabilities in Table 7.1 were used. The simulated spectrum as well as the transition probabilities show no magnetic polarization.

lous variation of the Eu^{2+} isomer shift with concentration. Lambe and Schroeer [57] and Schroeer et al. [58] extended the Mössbauer studies to lower concentration (0.1%-10%) and observed an even stronger anomalous variation of the isomer shift with Eu^{2+} concentration from -11.3 mm/s (0.1%) to approximately -13.4 mm/s (1%-10%). In addition, these authors reported on a very broad linewidth (up to 8 mm/s compared to a common experimental linewidth of around 2.5 mm/s) of the Eu^{2+} absorption lines, which they attributed to spin-spin relaxation effects of paramagnetic splitting. For very dilute crystals the electron spin relaxation times are slow enough to resolve the hyperfine interaction, as shown from the ENDOR measurements at 13 K [53]. ^{151}Eu-Mössbauer studies on such dilute Eu-doped samples are very difficult and time consuming because of the extremely low Eu-concentration.

1.1 CaF_2 doped with 0.1% Eu

Figure 7.3 show the Mössbauer spectra of CaF_2 doped with 0.1% Eu. The spectra have an asymmetric shape with two absorption bands at -11 mm/s and -24 mm/s. It was not possible to fit these spectra with a normal Mössbauer program without assuming unusual values for quadrupole interaction and/or isomer shifts. Therefore, in this thesis a possibility to fit these spectra of highly diluted samples had to be found. With the help of a special program developed in this thesis it was possible to fit the spectra in Figure 7.3. The spectra have an isomer shift of -13.4 mm/s. Since the spectrum recorded at 4 K has the best statistics of these three spectra the linewidth of about 5 mm/s was used as a fixed parameter for the fittings of the two other spectra. The theory and structure of the simulation programm is described in the following.

Since CaF_2 has a cubic crystal structure the hyperfine structure is isotropic. The Ca^{2+} and thus the unperturbed Eu^{2+} site has O_h symmetry. The spin Hamiltonian is given by [53]:

$$\begin{aligned}
\mathscr{H} &= \underbrace{g\,\mu_B\,\mathbf{B}\,.\,\mathbf{S}}_{\text{electron Zeeman}} + \underbrace{B_4^0 O_4^0 + B_6^0 O_6^0 + B_6^4 O_6^4}_{\text{crystal field}} + \underbrace{A\,\mathbf{S}\,.\,\mathbf{I}}_{\text{hyperfine}} - \underbrace{g_N\,\mu_N\,\mathbf{B}\,.\,\mathbf{I}}_{\text{nuclear Zeemann}} \qquad (7.1)\\
&= g\,\mu_B\,\mathbf{B}\,.\,\mathbf{S} + B_4(O_4^0 + 5O_4^4) + B_6(O_6^0 - 21O_6^4) + A\,\mathbf{S}\,.\,\mathbf{I} - g_N\,\mu_N\,\mathbf{B}\,.\,\mathbf{I}\\
&= g\,\mu_B\,\mathbf{B}\,.\,\mathbf{S} + \frac{1}{60}b_4(O_4^0 + 5O_4^4) + \frac{1}{1260}b_6(O_6^0 - 21O_6^4) + A\,\mathbf{S}\,.\,\mathbf{I} - g_N\,\mu_N\,\mathbf{B}\,.\,\mathbf{I}
\end{aligned}$$

where O_k^q are the Stevens operators and b_k and B_k^q the Stevens parameters. They describe the cubic crystal field. Where $B_4^0 = B_4$, $B_4^4 = 5\,B_4$, $B_6^0 = B_6$ and $B_6^4 = -21\,B_6$. The Stevens operators O_k^q for $J = 7/2$ are given in [14] and shown in appendix 1. The first term in Equation A.1 represents the electron Zeeman interaction with an external field **B**, the next one the effects of the crystal field of cubic symmetry, the third one the hyperfine interaction of the electronic spin **S** with the nuclear dipole moment **I**, and the last one the nuclear Zeeman interaction with an external field **B**.

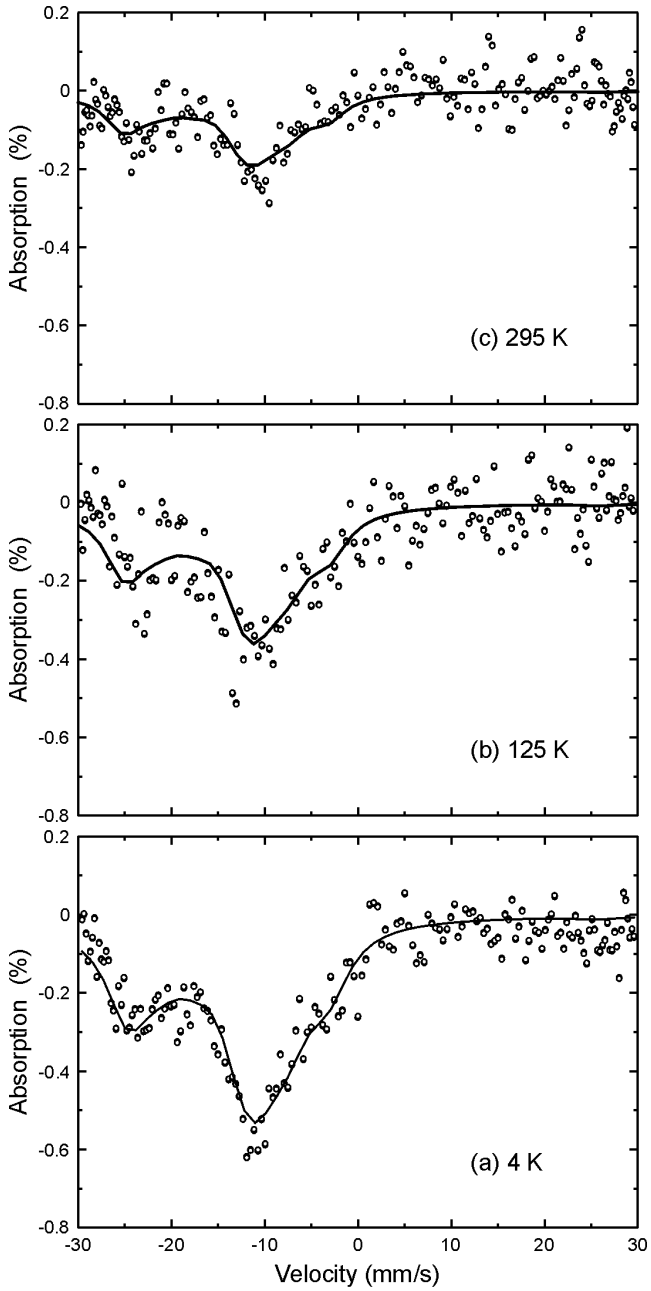

Figure 7.3: Mössbauer spectra of CaF_2:Eu^{2+} (0.1%), recorded from top to bottom at 300, 125 and 4 K.

For Eu^{2+} in CaF_2 the cubic splitting parameters are [53]:

$$b_4 = (-176.12 \pm 0.02)\text{MHz} = (-58.75 \pm 0.001) \cdot 10^4 \text{ cm}^{-1}$$
$$b_6 = (+0.78 \pm 0.2)\text{MHz} = (+0.26 \pm 0.001) \cdot 10^4 \text{ cm}^{-1}.$$

The g value is 1.9926 and the hyperfine interaction parameter A(^{151}Eu) is [53]:

$$(-102.907 \pm 0.001) \text{ MHz} = (-34.32 \pm 0.001) \cdot 10^4 \text{ cm}^{-1}.$$

With this it follows:

$$\begin{aligned} B_4^0 &= -2.94 \text{ MHz}, \\ B_4^4 &= -14.68 \text{ MHz}, \\ B_6^0 &= 0.62 \text{ kHz, and} \\ B_6^4 &= -13 \text{ kHz}. \end{aligned}$$

The nuclear g (g_N) value is 1.389 for the ground and 0.734 for the excited state. The hyperfine constant A shows a slight temperature dependency in the temperature range between 0 and 300 K. Between 0 and 100 K the value is constant $-34.25 \cdot 10^{-4}$ cm^{-1}, the value decreases from 100 to 300 K to $-34.07 \cdot 10^{-4}$ cm^{-1} [59]. The variation of less than 1% is negligible in the calculation of the energy levels. The value of A used for the calculations is that at room temperature.

To simulate the spectra, the spin Hamiltonians for the ground and excited state have to be solved. The Eu^{2+} ground state has an electron spin of $S = 7/2$ and a nuclear spin of $I = 5/2$; the excited state is a $S = 7/2$ and $I = 7/2$ spin state. The hyperfine part $A\,\mathbf{S}.\mathbf{I}$ of the Hamiltonian for the ground and the excited state is thus a $((2S+1)(2I+1) \times (2S+1)(2I+1)))$ (48×48) and (64×64) matrix, respectively. The matrix elements of the ground and excited state are given in appendix 2 and 3, respectively. The eigenvalues of the matrices are the energy levels of the states. Instead of diagonalizing the matrices, the energy levels were calculated with the help of the software package "visual EPR" [16, 17].

Figure 7.4 shows the energy levels for the ground state of $^{151}Eu^{2+}$ in CaF_2 as a function of magnetic field from 0 to 0.2 T.

In the ground state there are eight m_S states, each is magnetically split into six m_I substates and in the excited state there are eight m_S states, each splits into eight m_I substates. Nuclear transitions can only occur within the same electronic m_s state ($\Delta m_S = 0$). For the simulation of a theoretical spectrum for each m_s state the 18 nuclear transitions were calculated. Each transition has a Lorentzian line shape. Each Lorentzian is multiplied by its transition probability, which are given in Table 7.1. The transition probabilities are the square of the the Clebsch-Gordon coefficients. A detailed description of calculating the Clebsch-Gordon-coefficients is given in appendix B.

To obtain the simulated spectrum for one electronic m_S state, all 18 nuclear transitions have to be added. Figure 7.5 shows the ^{151}Eu Mössbauer spectra of Eu in CaF_2 for the different m_S states without a magnetic field. To get the complete spectrum the spectra of the eight m_S states, each with 18 transitions, have to be added together. This computation was carried out with Maple©. An example of the program is given in appendix C.

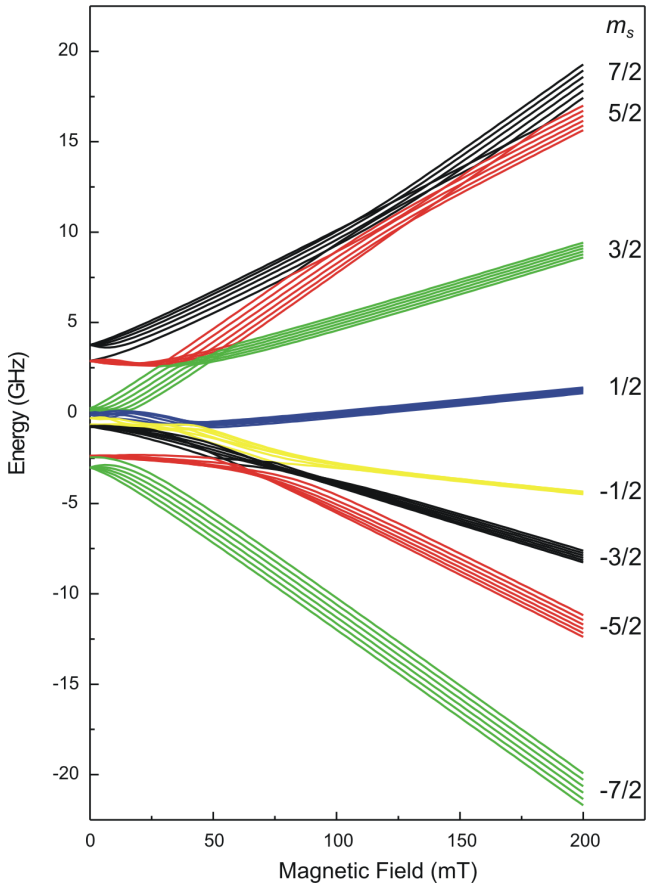

Figure 7.4: Energy levels of the ground state of $^{151}Eu^{2+}$ in CaF_2 as a function of magnetic field from 0 to 0.2 T

	m_{I_g}					
m_{I_e}	5/2	3/2	1/2	-1/2	-3/2	-5/2
7/2	55.55	0	0	0	0	0
5/2	15.87	39.68	0	0	0	0
3/2	2.65	26.45	26.45	0	0	
1/2	0	7.94	31.74	15.87	0	0
-1/2	0	0	15.87	31.74	7.94	0
-3/2	0	0	0	26.45	26.45	2.65
-5/2	0	0	0	0	39.68	15.87
-7/2	0	0	0	0	0	55.55

Table 7.1: Transition probabilities for ^{151}Eu (10^{-3}) in the presence of a magnetic field given (values taken from [51].)

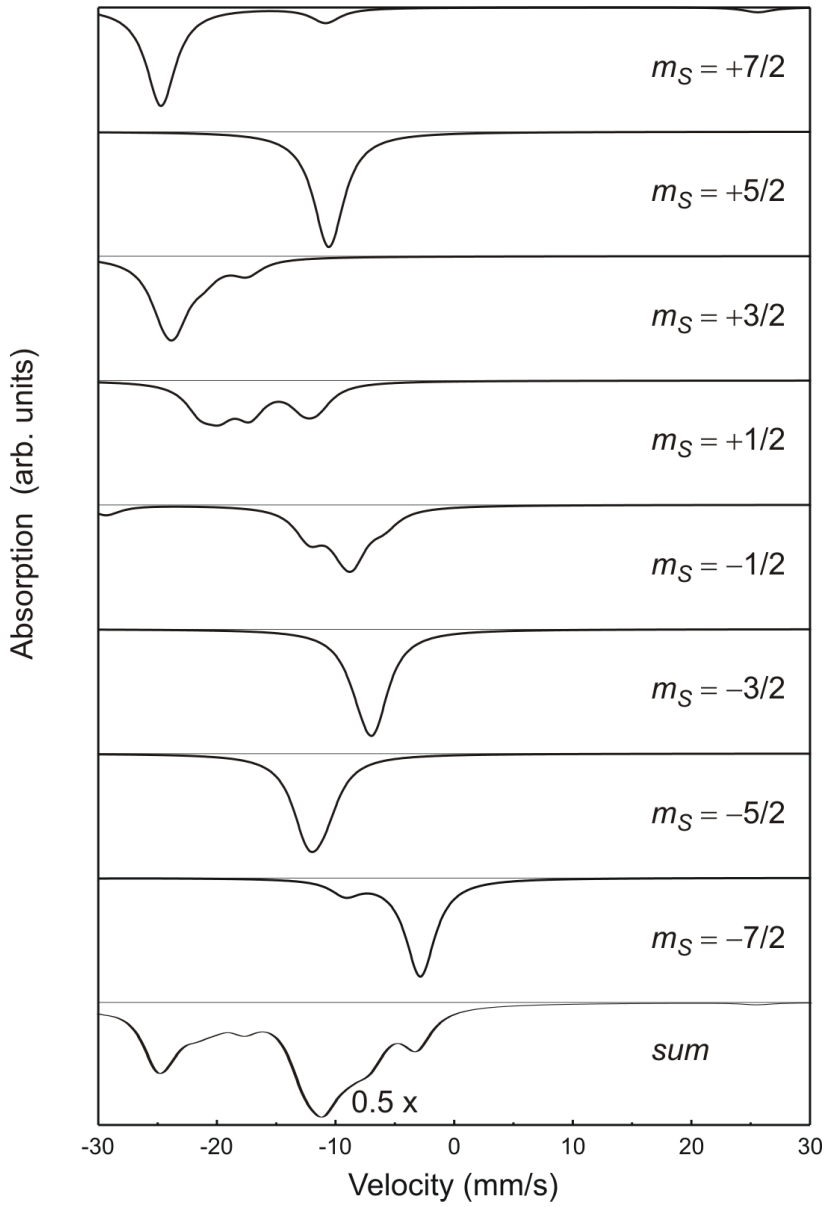

Figure 7.5: Theoretical Mössbauer spectra of ^{151}Eu in CaF_2. The calculation for the different m_S states was carried out for zero field. For the Mössbauer transitions a linewidth of 3 mm/s was used; the isomer shift was -13.5 mm/s. The lowest spectrum is the sum of all m_s subspectra.

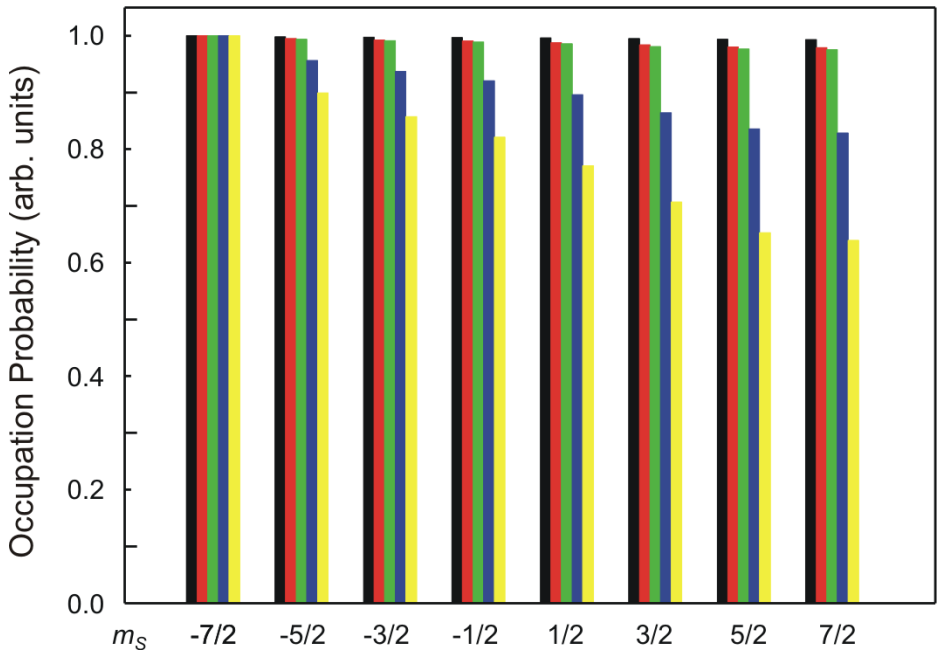

Figure 7.6: Occupation probability of the different states for different temperatures in the presence of a magnetic field with 200 mT: black 300 K, red 90 K, green 77 K, blue 10 K, and yellow 4.2 K.

For comparison with the measured spectra the calculated subspectra of the electronic m_S states have to be weighted by their occupation probability. This can be calculated with the Boltzmann distribution:

$$\frac{N}{N_0} = \exp(-\frac{\Delta E}{k_B T}) \tag{7.2}$$

where ΔE is the energy difference between the lowest level N_0 and the state N, k_B is the Bolzmann constant and T is the temperature.

Figure 7.6 shows the occupation probabilities for different temperatures in the presence of a magnetic field of 0.2 T. Especially in the presence of strong magnetic field (see section 1.4) or at low temperatures the occupation probability has to be taken into account. The simulated spectra were fitted by varying the linewidth and the isomer shift to the measured data with the help of Microcal Origin©.

After the successful description of the paramagnetic splitting in the spectra of CaF_2 doped with 0.1% Eu in Figure 7.3, the same sample was also studied in an external magnetic field of 0.2 T in order to test the applied theoretical description. Figure 7.7 exhibits the ^{151}Eu-Mössbauer spectrum of CaF_2 doped with 0.1% Eu measured at room temperature. The spectrum shows a broad structured absorption band at -13.5 mm/s and a linewidth of 4.5 mm/s, which is definitely different from the split spectra of the same samples measured without an external magnetic field (Figure 7.3).

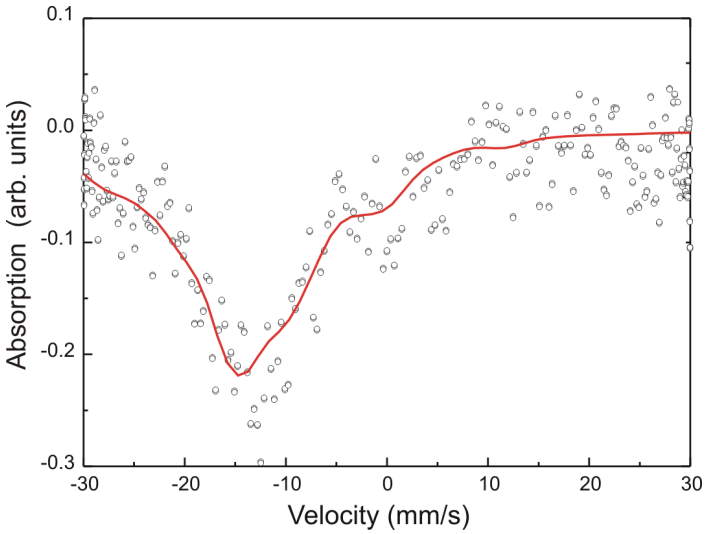

Figure 7.7: Mössbauer spectra of CaF_2:Eu^{2+} (0.1%), recorded at room temperature ein an external magnetic field of 0.2 T.

For the simulation of the experimental spectrum the energy levels of ^{151}Eu in the presence of a magnetic field of 0.2 T were calculate. It can be seen in Figure 7.4 that an external magnetic field has a strong impact on the energy levels. Analog to the simulation without a magnetic field, the theoretical spectra of the m_s states with its 18 nuclear transitions were calculated. Figure 7.8 show the simulated Mössbauer spectra of ^{151}Eu in CaF_2 for the different m_S states in a magnetic field of 0.2 T.

The eight m_S subspectra were added and weighted by their occupation probability. The simulated spectra were fitted to the experimental spectrum by varying the linewidth and the isomer shift with the help of Microcal Origin©. The resulting spectrum agrees very well with the measured data (see Figure 7.7).

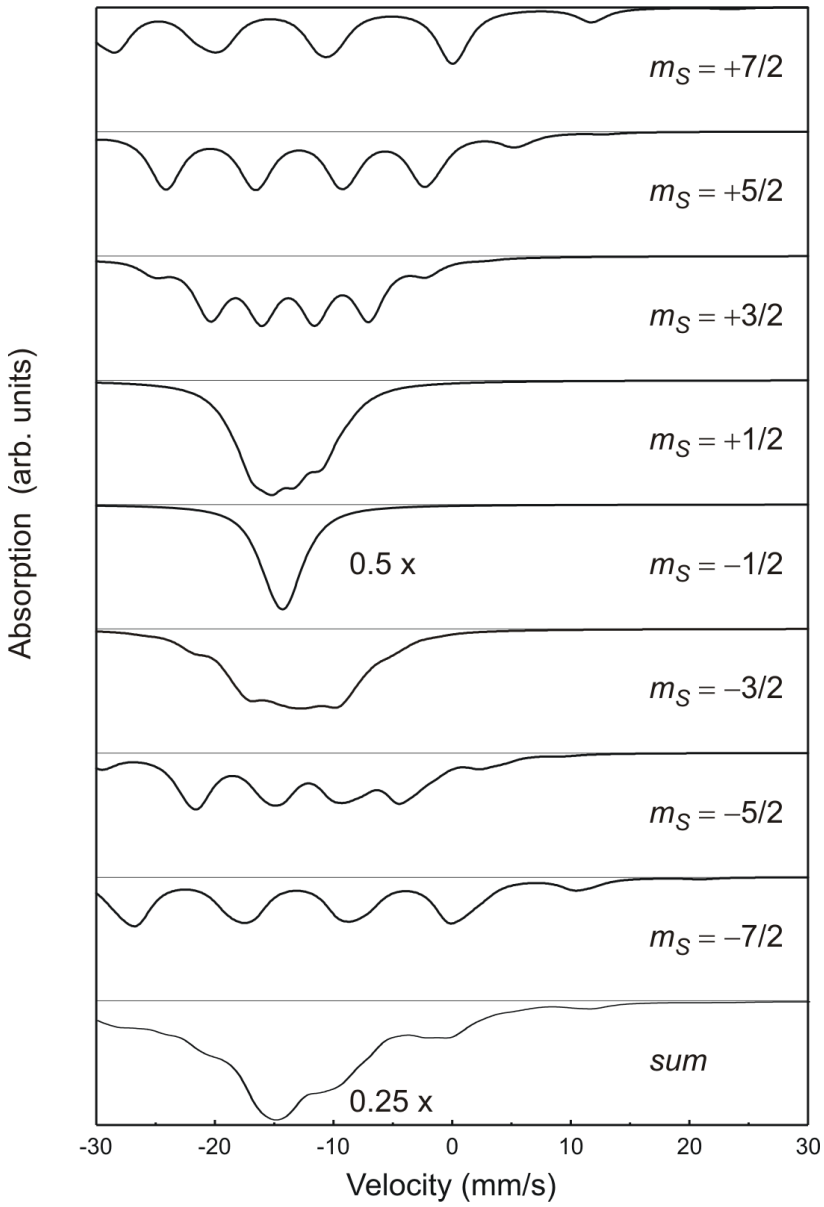

Figure 7.8: Theoretical Mössbauer spectra of ^{151}Eu in CaF_2. The calculation for the different m_S states was carried out for an external magnetic field of 0.2 T. For the Mössbauer transitions a linewidth of 3 mm/s was used; the isomer shift was -13.5 mm/s. The lowest spectrum is the sum of all m_s subspectra.

1.2 CaF_2 doped with 2% Eu

Figure 7.9 shows the ^{151}Eu Mössbauer spectra of CaF_2 doped with 2% Eu recorded at 295, 90, and 10 K. They are drastically different from those of the 0.1% Eu-doped systems of Figure 7.3 in that they exhibit only a symmetrically broadened single line at -13.4 mm/s, virtually independent of temperature. This is the same isomer shift as reported in the previous Mössbauer studies for this concentration range [53–57]. Additionally, a weak absorption dip around 0 mm/s (Eu^{3+}) can be observed. For 2% Eu concentration in CaF_2, the electron spin relaxation rates are certainly much larger than in the 0.1% Eu-doped system, where we observed resolved hyperfine splitting, but obviously not high enough to lead to a normal Mössbauer linewidth, as observed for instance in the concentrated systems EuF_2 and EuS with $FWHM_{exp}$ = 2.5 mm/s. The observed linewidth of (7.7 $\pm$ 0.1) mm/s at 10 K exhibits only a minor decrease to (7.6 $\pm$ 0.1) mm/s at 295 K.

The Mössbauer spectra show that 98% of the doped Eu ions are in the Eu^{2+} state and 2% in the Eu^{3+} state showing up at 0 mm/s. Schroeer et al. [58] observed the same small amount of Eu^{3+} in CaF_2:Eu systems with an Eu concentration of 2%. The increase of the absorption depth for the Eu^{2+} line is about 50% between 295 and 10 K.

1.3 CaF_2 doped with 2% Eu in a small magnetic field of 0.2 T

The Mössbauer spectra of CaF_2:Eu (2%) sample recorded at 295, 90, and 10 K in the presence of a magnetic field of 0.2 T is shown in Figure 7.10. With a magnetic field of only 0.2 T, applied by a permanent magnet parallel to the γ-ray direction, the spectral shape changed considerably in the Mössbauer spectra. A dominant absorption band around -13.4 mm/s with an additional shoulders on both sides can be observed. The spectra were fitted with three components. The most dominant component with a fraction of nearly 80% is that of Eu^{2+}. It has an isomer shift of -13.5 mm/s and a linewidth of 8.3 mm/s at 295 K, isomer shift of -13.3 mm/s and a linewidth of 7.8 mm/s at 90 K and isomer shift of -13.4 mm/s and a linewidth of 7.8 mm/s at 10 K. The second component is fitted with an an almost temperature independent magnetic hyperfine field of 24.8 T (295 K), 27.1 T (90 K), and 27.3 T (10 K). It was fitted in a first appoach with the same isomer shift as its corresponding Eu^{2+} curve, but a smaller linewidth of around 5 mm/s at all temperatures. The last component is that of Eu^{3+} with a fraction of 2%, adjusted with the same parameters as in the spectrum without an external magnetic field.

An additional spectrum taken of the CaF_2:Eu (2%) sample at 295 K in an external field of 0.2 T applied perpendicular to γ-ray direction exhibited exactly the same spectrum as the one measured with the parallel external field without any polarization effect. This indicates that the observed hyperfine fields B_{hf} are randomly oriented in both cases, their direction only depending on the random direction of the Eu^{2+} neighbors, as expected for a polycrystalline sample (see discussion in section 1.5).

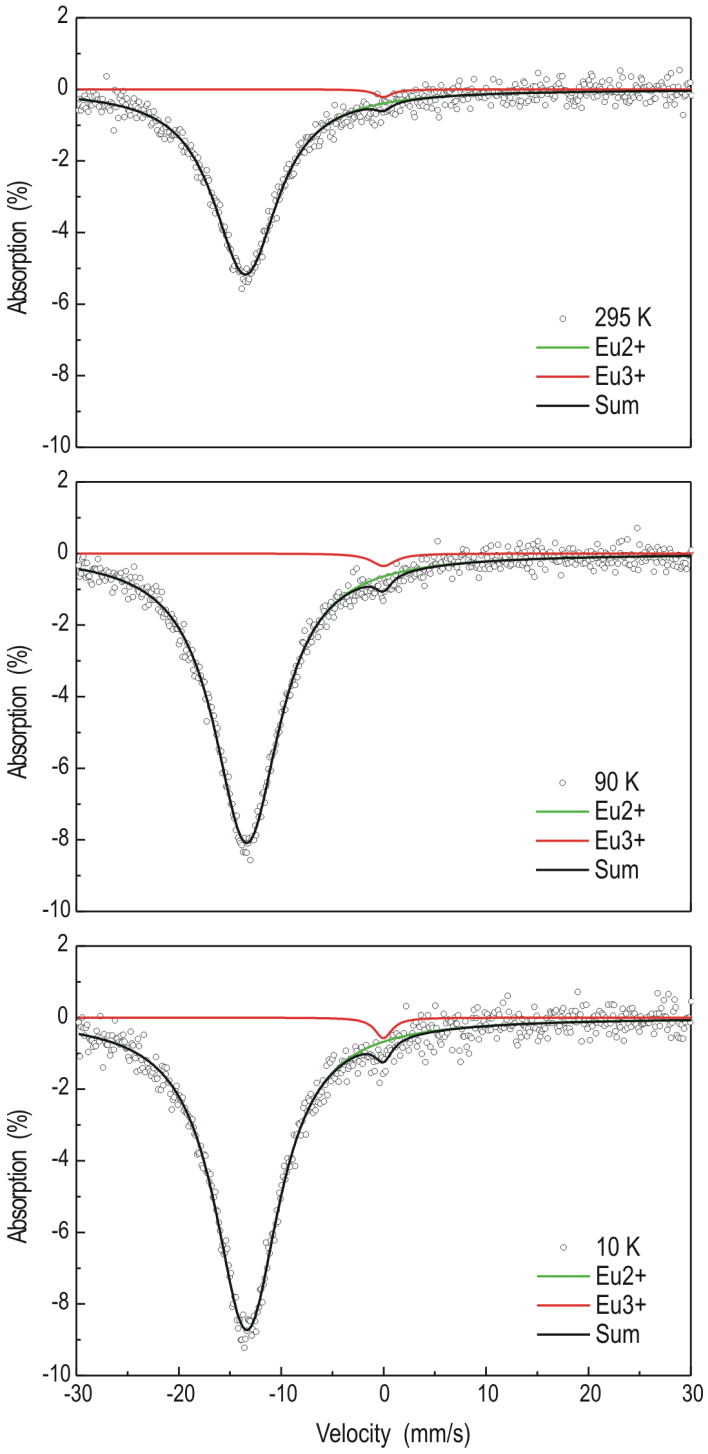

Figure 7.9: Mössbauer spectra of CaF_2:Eu^{2+} (2%), recorded at 295 K, 90 K, and 10 K.

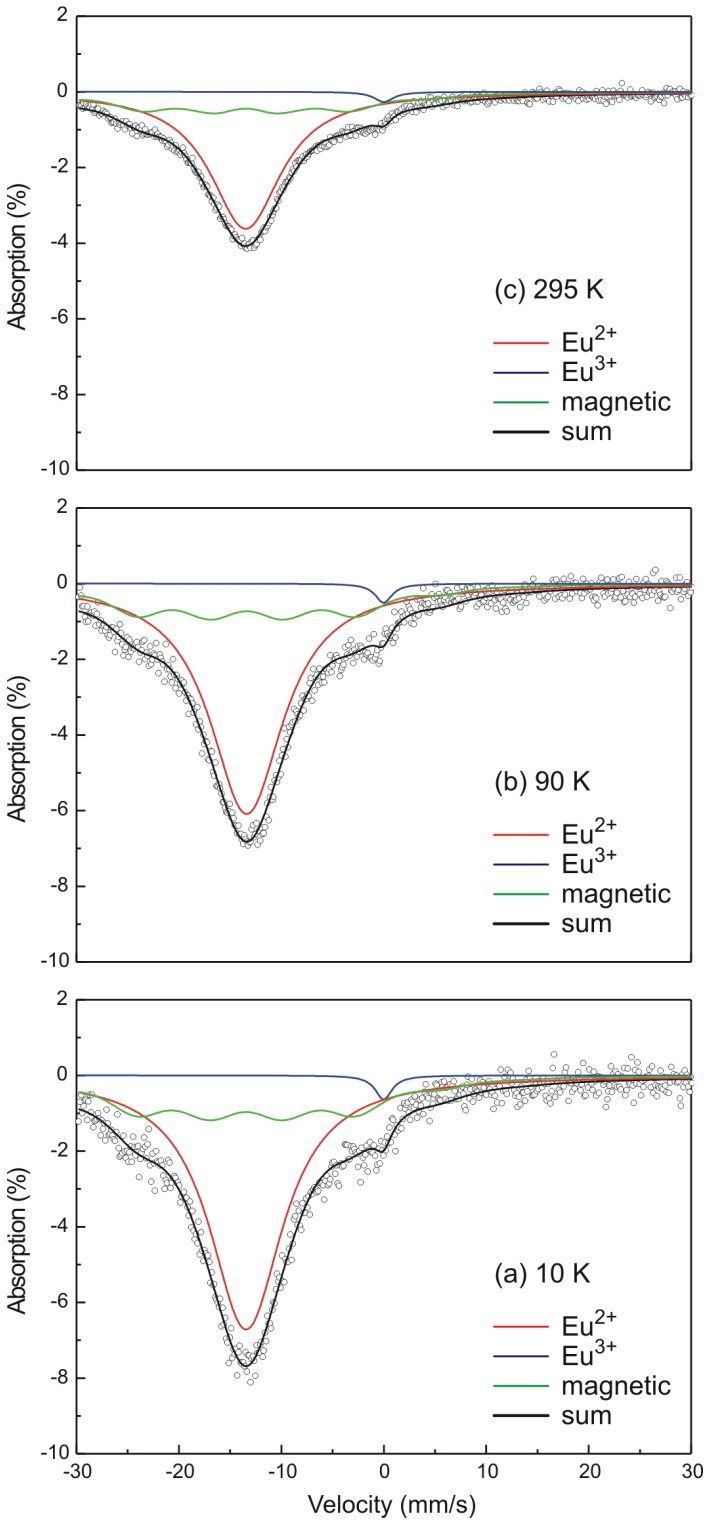

Figure 7.10: Mössbauer spectra of CaF_2:Eu^{2+} (2%), recorded at 295 K, 90 K, and 10 K in an external magnetic field of 0.2 T.

1.4 CaF_2 doped with 2% Eu in a magnetic field of 6 T

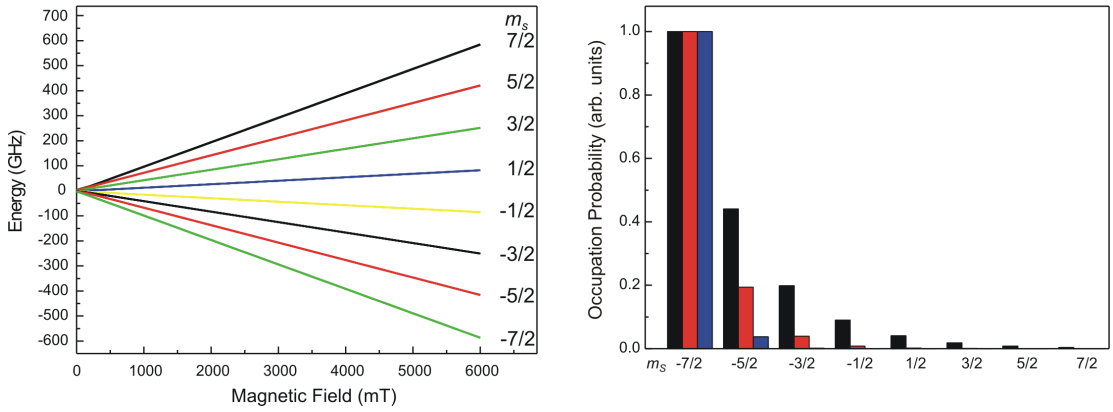

Figure 7.11: Energy levels of the ground state of $^{151}Eu^{2+}$ in CaF_2 as a function of magnetic field from 0 to 0.2 T (left side) and occupation probability of the different m_S states for different temperatures in the presence of a magnetic field with 6 T: black 10 K, red 5 K, and blue 2.5 K (right side).

Figure 7.11 shows the energy levels for the ground state of $^{151}Eu^{2+}$ in CaF_2 as a function of magnetic field from 0 to 6 T (left side) and the occupation probability of the different m_S states for different temperatures in the presence of a magnetic field with 6 T (right side).

In a large magnetic field of 6 T applied perpendicular to the γ-ray direction at low temperatures, the full hyperfine interaction is observed at 2.5 K (Figure 7.12a). This spectrum is, in a first approach, identical to that observed for magnetic ordering in a concentrated sample, fitted with an effective hyperfine field arising (beside transferred and external fields) from the $J = S = 7/2$ ground state of the ordered Eu^{2+} $4f$-moments with the 18 transitions of the $I_g = 5/2$ nuclear ground state to the $I_e = 7/2$ nuclear excited state, exhibiting now a non-broadened linewidth of (2.3 ± 0.1) mm/s. From the relative intensities of the four main lines (each consisting of three transitions) as well as from the some less intense lines at the wings (around +6 mm/s), one immediately recognizes a polarization dependence, according to the external perpendicular field, enhancing the $m_I = 0$ transitions by a factor of two. The observed effective field at the Eu nuclei, $B_{\text{eff}} = B_{\text{hf}} + B_{\text{ext}} = -27.65\ T$ which leads for an external field of 6 T to a hyperfine field of $B_{\text{hf}} = 33.65\ T$. This value of B_{hf} is close to the value 34 T reported by [51].

The ^{151}Eu-spectra of CaF_2:Eu (2%) at 5 and 10 K (Figure 7.12b and c) exhibit drastically different features, which cannot be fitted by an effective field approach as in concentrated magnetically ordered Eu^{2+} systems, because we are dealing here with partially oriented paramagnetic Eu^{2+} ions. The contributions to the spectra originate now from the m_S sublevels ($m_S = 7/2, 5/2, 3/2, 1/2, ...$) of the $S = 7/2$ $4f$-moment with drastically different hyperfine fields. They contribute to the Mössbauer spectrum according to their Boltzmann populations (solide lines in Figure 7.12).

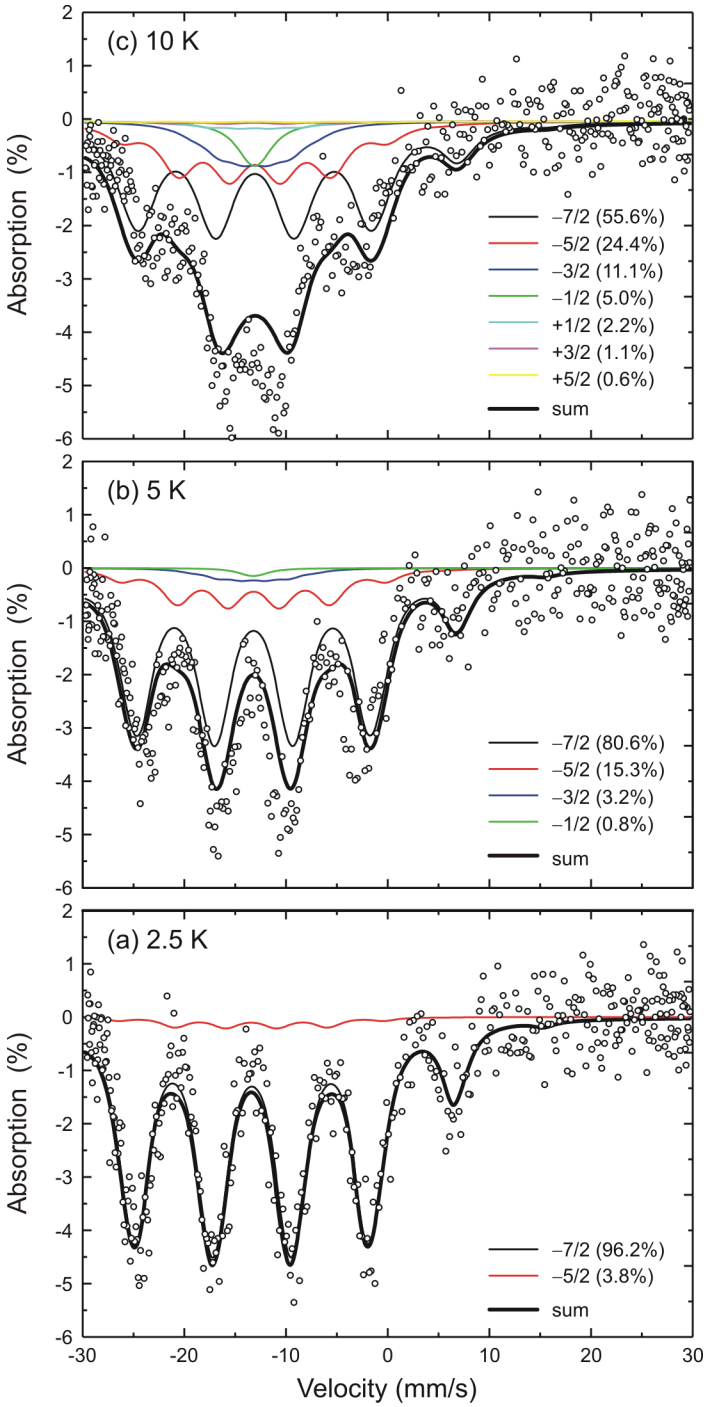

Figure 7.12: Mössbauer spectra of CaF_2:Eu^{2+} (2%) at (a) 2.5, (b) 5, and (c) 10 K in an external magnetic field of 6 T; the magnetic field direction was perpendicular to the incident γ-rays. The solid curves are fits as described in section 1.1

1.5 Discussion

doping level	Temp. (K)	ext. mag. field (T)	isomer shift (mm/s)	linewidth (mm/s)	hf field (T)	fraction %	ion
0.1%	295	-	-13.5 ± 0.2	5	-	100	Eu^{2+}
	125	-	-13.4 ± 0.2	5	-	100	Eu^{2+}
	4	-	-13.4 ± 0.2	5.3 ± 0.3	-	100	Eu^{2+}
0.1%	295	0.2	-13.5 ± 0.2	4.5	-	100	Eu^{2+}
2%	295	-	-13.5 ± 0.2	7.6 ±0.3		98	Eu^{2+}
		-	0.0	3		2	Eu^{3+}
	90	-	-13.3 ± 0.2	7.8 ±0.3		98	Eu^{2+}
		-	0.0	3		2	Eu^{3+}
	10	-	-13.3 ± 0.2	7.7 ±0.3		98	Eu^{2+}
		-	0.0	3.0 ± 0.2		2	Eu^{3+}
2%	295	0.2	-13.5 ± 0.2	8.3 ±0.3		77	Eu^{2+}
		0.2	-13.5	5.0 ±0.2	24.8	21	Eu^{2+}
		0.2	0.0	3.0		2	Eu^{3+}
	90	0.2	-13.4 ± 0.2	7.8 ±0.3		75	Eu^{2+}
		0.2	-13.4	5.2 ±0.2	27.1	23	Eu^{2+}
		0.2	0.0	3.0		2	Eu^{3+}
	10	0.2	-13.4 ± 0.2	7.8 ±0.3		75	Eu^{2+}
		0.2	-13.4	5.2 ±0.2	27.3	23	Eu^{2+}
		0.2	0.0	3.0 ± 0.2		2	Eu^{3+}
2%	10	6	-13.2 ± 0.2	3.8 ± 0.2		100	Eu^{2+}
	5	6	-13.3 ± 0.1	3.1 ± 0.2		100	Eu^{2+}
	2.5	6	-13.4 ± 0.1	2.3 ± 0.1		100	Eu^{2+}

Table 7.2: Fitting parameters of the ^{151}Eu-Mössbauer spectra of 0.1% and 2% Eu-doped CaF_2. Fixed parameters are given without error bars. The isomer shifts are relative to EuF_3.

Table 7.2 summarizes the fitting parameters as isomer shift and linewidth of the fits. The spectra of the 0.1% Eu-doped CaF_2 samples were fitted with the simulation described in section 1.1. The spectra of the 2% doped sample were fitted with common Mössbauer programs. The ^{151}Eu-Mössbauer spectra of 2% Eu-doped CaF_2 in a magnetic field of 6 T were fitted with the simulation program.

A broadened line of about 8 mm/s in Mössbauer spectrum of ^{151}Eu ions isolated in an Argon matrix at 6 K have been reported by Litterst et al. [60] and attributed to an unresolved hyperfine splitting. The spectrum was fitted considering a "free-atom", with this the magnetic hyperfine interaction is described by $A\,\mathbf{I}\,.\,\mathbf{J}$ and with this the hyperfine spectrum is completely determined by the free atom values A and J. For a perfect fit they had to assume a small axial anisotropic A_z. The present observation of a large resolved param-

agnetic hyperfine splitting with corresponding low relaxation times for the 0.1% Eu-doped CaF_2 sample even at room temperature is a completely new finding and offers immediately a new and consisted interpretation of the previously reported anomalous behavior of the Mössbauer isomer shift in the CaF_2:Eu^{2+} system.

The isomer shift of -13.4 mm/s found for the ^{151}Eu-Mössbauer spectra of 0.1% Eu-doped CaF_2 is consistent with the isomer shifts observed for more concentrated systems [54–57]. This is a first proof that a resolved paramagnetic splitting was observed. For the diluted crystals the electron spin relaxation times were slow enough to resolve the hyperfine interactions. The ^{151}Eu-Mössbauer spectrum of 0.1% Eu-doped CaF_2 in a field of 0.2 T is more symmetrical than the corresponding spectrum with out an external magnetic field. The effect of a field with $g\mu_B B > A$ is to suppress the fluctuating (off-diagonal) terms of the hyperfine interaction matrix $A\,\mathbf{S.I}$: $A(S_xI_x + S_yI_y)$. This leaves AS_zI_z and with this the hyperfine interaction becomes an effective field proportional to the magnetization of the Eu^{2+} ions.

The anomalous shifts reported by [54, 55, 57, 58] were speculatively attributed to oxygen neighbors of the Eu^{2+} ions, with a detailed model for possible O^- configurations [57, 58]. The spectra of 2% Eu sample did not show any deviation from a Lorentzian line shape. This excludes the possibility of any static quadrupole interaction, which had tentatively attributed to the observed anomalous isomer shift in these system [56, 57]. This indicates that the Eu^{2+} ions are located on regular Ca^{2+} without O^- neighbors.

Unfortunately, neither of the above-mentioned publications [54, 55, 57, 58] showed a Mössbauer spectrum of a of CaF_2:Eu st very low Eu-concentration. A possible explanation for the observed anomalous isomer shift may be that the Mössbauer spectra were recorded for velocities smaller than $\pm 20\ mm/s$. If this is the case only the dip at -11 mm/s in the 0.1% spectrum can be observed and it appears that the isomer shift increases with decreasing concentration.

For the 2% Eu-doped CaF_2 the electron spin relaxation rated are larger, but not high enough to lead to a normal Mössbauer linewidth, as observed in the concentrated systems EuF_2 and EuS with $FWHM_{exp}$=2.5 mm/s. These very broad linewidth (up to 8 mm/s) of the Eu^{2+} absorption lines have also been reported by these authors [54, 55, 57, 58], which they attributed to spin-spin relaxation effects of paramagnetic splitting.

In the ^{151}Eu-Mössbauer spectra of 2% Eu-doped CaF_2 with an external magnetic field of 0.2 T the external field suppresses the off-diagonal terms of the hyperfine interaction matrix $A\,\mathbf{S.I}$ as with the 0.1% sample. Due to the faster electron spin relaxation the spectrum is more symmetrical than that of the 0.1% sample.

Obviously, the small external field of $B_{ext} = 0.2$ T is strong enough to reduce the relaxation rate for the Eu^{2+} ions in a way that the single line exhibits an additional broadening for about 20% of the Eu^{2+} ions. This 20% can be attributed to in a first approach to those with a next Eu^{2+} neighbor.

doping level k	0.1%	2%
0	98.81	78.47
1	1.19	19.22
2	$0.65 \cdot 10^{-2}$	2.16
3	$0.22 \cdot 10^{-4}$	0.15
4	$0.49 \cdot 10^{-7}$	$0.67 \cdot 10^{-2}$
⋮	⋮	⋮

Table 7.3: Probability of exactly k Eu ions as next neighbors in %

Assuming a random distribution of the Eu ions we can calculate the probability of getting exactly k Eu ions as next neighbors is given by the probability mass function:

$$P = \binom{n}{k} z^k (1-z)^{n-k} \tag{7.3}$$

Where n is the possible number of the next neighbors (here there are 12 possible Eu^{2+}-sites as next neighbors) and z is the doping level of the CaF_2 crystal in percent. The results for both samples are given in Table 7.3. It can be seen that in the case of the 0.1% sample the probability of getting an isolated Eu ion is nearly 99%. While in the 2% sample almost 20% of the Eu ions have one Eu ion as a next neighbor.

These 20% of the Eu ions experience an additional dipolar field from the direct Eu^{2+} neighbor. The coupled Eu^{2+} spin pair has a considerable reduction in the relaxation rate by the applied field. This dipole-dipole interaction can be described as a fine structure interaction. The fine structure parameter D/h can be calculated with the assumption of two point dipoles by:

$$\frac{D}{h} = \frac{\mu_0}{4\Pi} \cdot g_e \mu_b g_e \mu_b \cdot \frac{1}{R_0^3} \approx 52.000 \cdot \frac{1}{R_0^3} [MHz] \tag{7.4}$$

where R_0 (in Å) is the distance between the two interacting dipoles [18]. In a CaF_2 host lattice the distance between two Eu ions as next neighbors can be calculated by $\sqrt{\frac{1}{2}}a$, with $a = 5.452$ Å it follows that distance between the Eu ions is 3.86 Å. With this it follows $D/h = 908$ MHz this corresponds to a dipole field of 0.032 T. This interaction is nearly nine times larger than the hyperfine interaction A with -102.9 MHz and could explain why the spectra of the 2% Eu-doped CaF_2 sample look totally different to that of the 0.1% sample.

2 Eu-doped $BaCl_2$

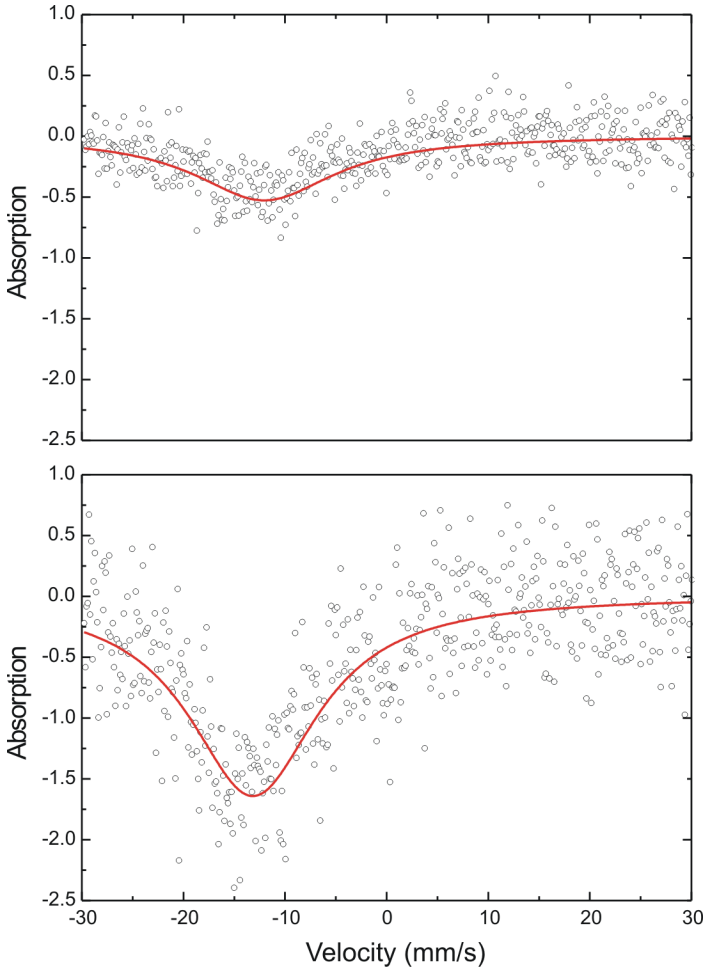

Figure 7.13: Mössbauer spectra of Eu-doped $BaCl_2$ powder recorded at 90 K (top) and 10 K (bottom).

The investigated sample was 2% Eu-doped $BaCl_2$. Eu^{2+} ions in a $BaCl_2$ host lattice substitutes for Ba^{2+}. The Eu ion has 12 possible positions for Eu ions as next neighbors. This lead to a probability that approximately 20% of the Eu ions have one Eu ion as a next neighbor. That is the same case than for the CaF_2 with 2% Eu. Therefore, the Mössbauer spectra of $BaCl_2$:Eu^{2+} were fitted with a common Mössbauer program.

Figure 7.13 shows the Mössbauer spectra of $BaCl_2$:Eu^{2+} without an applied magnetic field at 90 and 10 K. Both spectra show one single dip. They were fitted with one Lorentzian line as done for CaF_2 with 2% Eu. The isomer shift is (-13.0±0.5) mm/s and the linewidth is (17±1) mm/s at 90 K and (12±1) mm/s at 10 K.

Figure 7.14 shows the Mössbauer spectra of $BaCl_2$:Eu^{2+} with an applied magnetic field of 0.2 T at 10 K. The fitting was done analog to CaF_2 with 2% Eu. The spectrum was fitted with one Lorentzian line (72%) and one component with a hyperfine field of (30±2) T (28%).

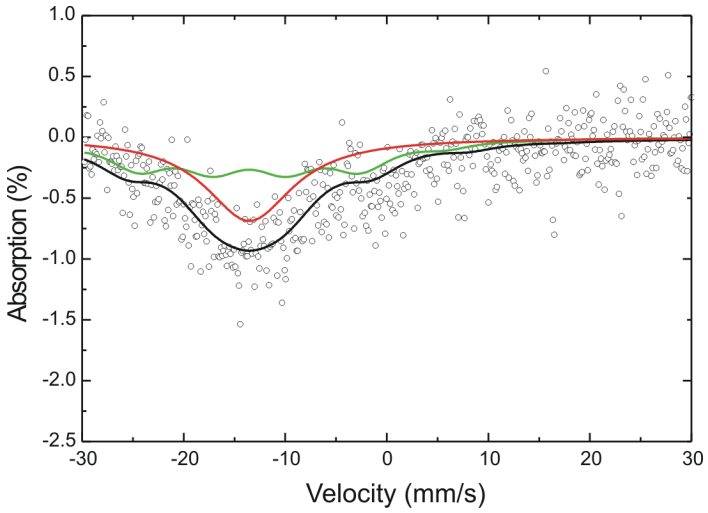

Figure 7.14: Mössbauer spectra of Eu-doped $BaCl_2$ powder recorded in the presence of a magnetic field of 0.2 T at 10 K.

Both curves have a isomer shift of (-13.5±5) mm/s. The Lorentzian line has a linewidth of (13±1) mm/s and the magnetic component a linewidth of (5.3±0.5) mm/s. For comparison $EuCl_2$ has an isomer shift of -13.16 mm/s at 77 K and -13.103 mm/s at 295 K [51].

A component of Eu^{3+} as seen in the ^{151}Eu Mössbauer spectra of CaF_2 with 2% Eu could not be unambiguously fitted to the spectra of 2% Eu-doped $BaCl_2$ sample, because of the rather low statistical accuracy. Unfortunately, it was also not possible to record a spectrum at room temperature because of the low signal. The low signal has two reasons: $BaCl_2$ has a high mass absorption coefficient (37.2 cm^2/g at 21.53 keV)[61] For comparison this is three times higher than that of CaF_2. The main cause is the weak bonding of the crystals lattice. Due to the weak bond the probability of lattice vibrations increases and with it the probability of a recoil. The crystal has a low Debye-Waller-factor which is a quantity of recoil free emissions. The Debye-Waller-factor decreases with increasing temperature. This explains why there is nearly no signal at room temperature.

3 Glass Ceramics

^{151}Eu Mössbauer investigations on Eu-doped fluorochlorozirconate glass ceramics have already been carried out by MacFarlane et al. [62]. They measure the Eu^{2+} to Eu^{3+} ratio to determine the efficacy of in situ reduction of Eu^{3+} to Eu^{2+} by a variety of chemical reductants and by bulk electrochemical reduction. In this work only the influence of the purity grade of EuF_2 on the Eu^{2+}/Eu^{3+} ratio is investigated. Hopefully, a relatively simple method of optimizing the glass ceramics can be found with this.

In this particular experiment we wanted to determine the Eu^{2+}/Eu^{3+} ratio in the differently doped fluorochlorozirconate glasses for various Eu doping concentration and to determine the Eu^{2+} concentration in the nanoparticles.

		Eu^{2+}			Eu^{3+}		
Sample	Temp. K	isomer shift mm/s	linewidth mm/s	area	isomer shift mm/s	linewidth mm/s	area
ZBLAN 75	295	-11.6	8.3 ± 1.0	3.41	-0.5	2.5 ± 0.3	11.19
	90	-11.6	8.0 ± 6.0	3.38	-0.5	2.8 ± 0.2	18.80
	10	-11.6 ± 1.0	10.0 ± 4.0	7.20	-0.5 ± 0.1	2.6 ± 0.3	21.73
ZBLAN 83	295	-14.6	19.3 ± 0.8	2.44	-0.4	2.4 ± 0.3	6.68
	10	-14.6 ± 1.0	14.0 ± 0.8	7.61	-0.4 ± 0.1	2.5 ± 0.2	13.80
N05-02-35B	295	-14.0	16.8 ± 3.3	10.37	-0.4	2.4 ± 0.6	6.40
	90	-14.0	14.8 ± 3.3	28.24	-0.4	2.3 ± 0.4	10.68
	5	-14.0 ± 0.4	14.6 ± 2.2	47.92	-0.4 ± 0.2	2.9 ± 0.2	12.55

Table 7.4: Fit parameters of the spectra in Figure 7.15 , 7.16, and 7.17. Fixed parameters are given without error bars. The area under the subspectra is given in arbitrary units.

Three different glasses doped with Eu were investigated: ZBLAN 75, ZBLAN 83, and N05-02-35B. The first two samples werde made in Paderborn. ZBLAN 83 was doped with 1% EuF_2 , ZBLAN 75 with 2% EuF_2. The last Sample (N05-02-35B) was made by an Australian group and doped with 2% EuF_2. It shows the best scintillation properties of these glasses. The main difference between this glass and those made in Paderborn is that the EuF_2 used for preparation was purer.

Figure 7.15 shows the Mössbauer spectra of ZBLAN 75 at 295, 90, and 10 K. All spectra show one dip for Eu^{2+} in the region between -13 and -12 mm/s and one for Eu^{3+} around 0 mm/s. These two peaks can also be observed in the spectra of ZBLAN 83 (Figure 7.16) recorded at room temperature and that of the N05-02-35B glass (Figure 7.17), recorded at 90 K. Table 7.4 summarized the isomer shift, linewidth and area of the subspectra of the ^{151}Eu Mössbauer spectra of Eu^{2+} and Eu^{3+} in the glass ceramics.

The area under the subspectra is an index for the corresponding Eu-concentration. If the ration of Eu^{2+}/ Eu^{3+} is determined by calculating the ration of the corresponding areas it seems that the ration varies with temperature. The Eu^{2+} and Eu^{3+} ions are differently strong bound in the glass ceramic. For the determination of the Eu^{2+}/ Eu^{3+} ratio the Debye-Waller-factor f of both ions have to be taken into account. The Debye-Waller-factor and the Debye-temperature θ_D are values for the strength of the bonding.

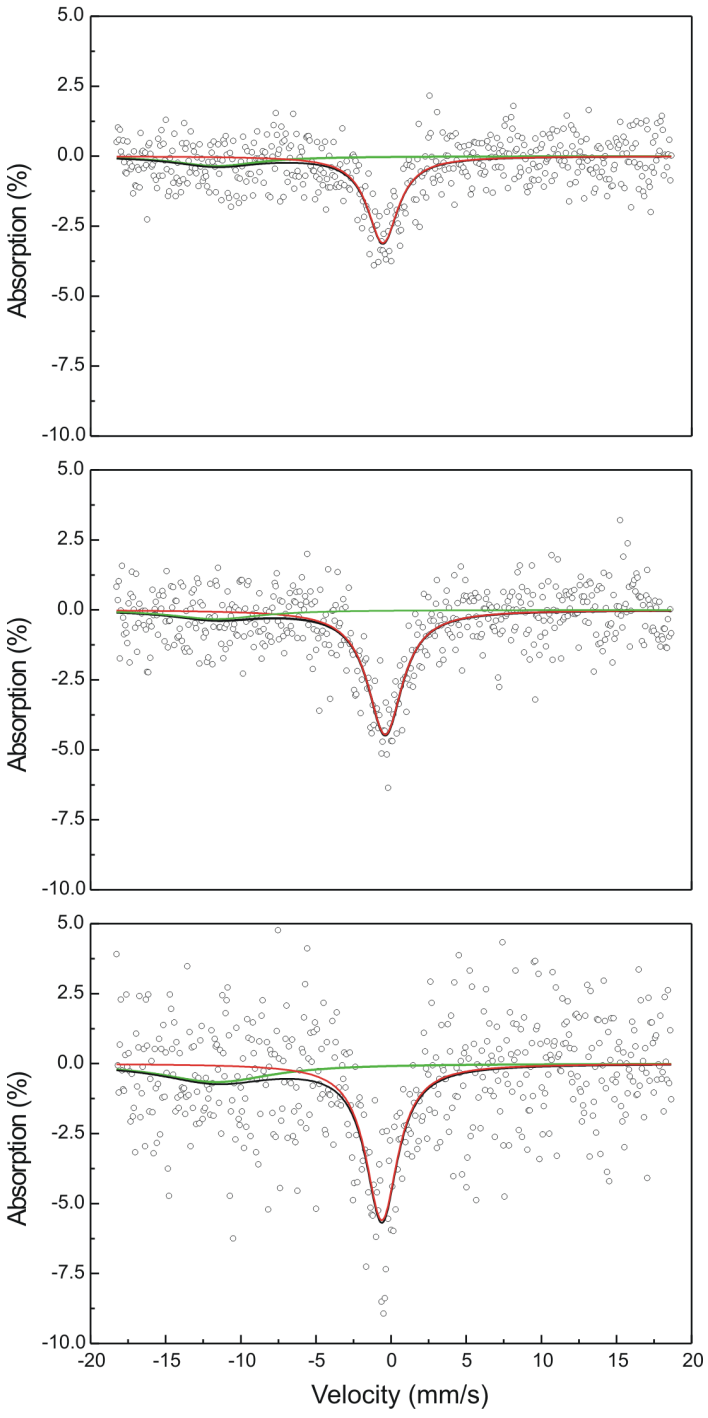

Figure 7.15: Mössbauer spectra of fluorozirconate glass ceramic ZBLAN 75 recorded from top to bottom at 295, 90, and 10K.

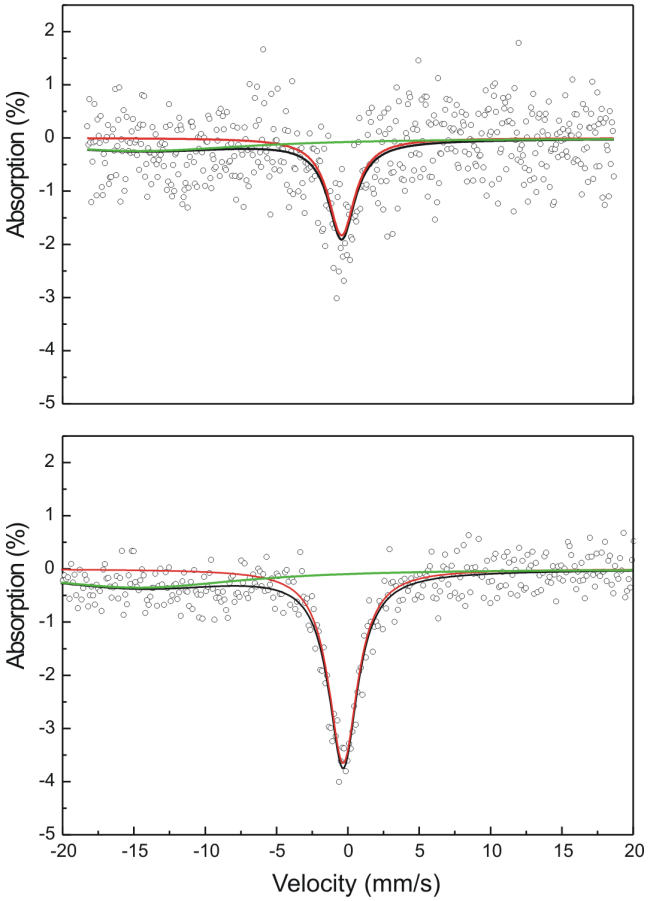

Figure 7.16: Mössbauer spectrum of fluorozirconate glass ceramic ZBLAN 83 recorded at 295 K (top) and 10 K (bottom).

The approximation for $T \geq \frac{\theta_D}{2}$

$$f(T) \approx \exp\left(-\frac{6E_r T}{k_B \theta_D^2}\right) \tag{7.5}$$

will be used in the following. To determine the Debye-temperature the areas of the subspectra have to be calculated and the natural logarithm ln(x) of the areas has to be plotted against temperature.

$$ln(f(T)) \approx -\frac{6E_r}{k_B \theta_D^2} \cdot T = mT \tag{7.6}$$

where m is the gradient of the resulting of the curve. The Debye-temperature can be calculated by:

$$\theta_D = \sqrt{-\frac{6E_r}{k_b m}} \tag{7.7}$$

$$\theta_D(^{151}\mathrm{Eu}) \approx \sqrt{-\frac{115.93}{m}}[K] \tag{7.8}$$

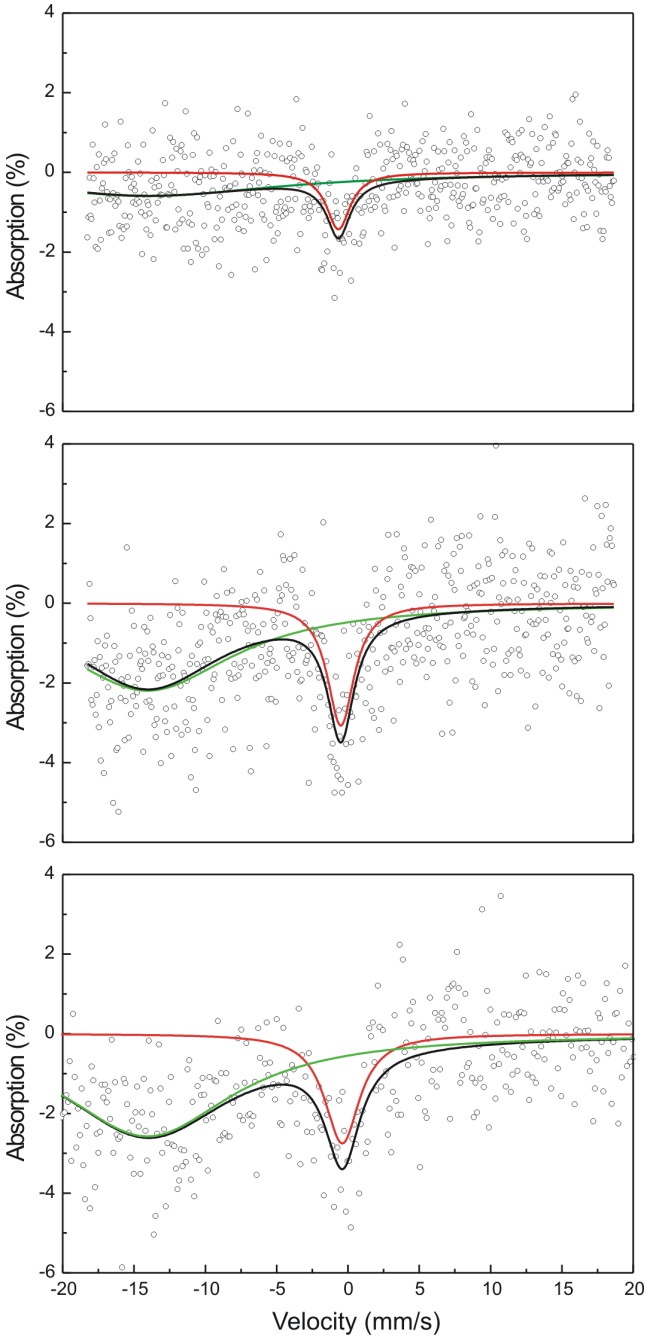

Figure 7.17: Mössbauer spectrum of fluorozirconate glass ceramic N05-02-35B recorded from top to bottom at 295, 90, and 5 K.

With the Debye-temperatures of the Eu^{2+} and Eu^{3+} ions we can calculate their Debye-Waller-factors. The Eu^{2+} / Eu^{3+} ration $R(\frac{Eu^{2+}}{Eu^{3+}})$ can be calculated by:

$$R\left(\frac{\mathrm{Eu}^{2+}}{\mathrm{Eu}^{3+}}\right) = \frac{A_{(\mathrm{Eu}^{2+})}}{A_{(\mathrm{Eu}^{3+})}} \cdot \frac{f_{(\mathrm{Eu}^{3+})}}{A_{(\mathrm{Eu}^{2+})}} \tag{7.9}$$

where $A_{(\mathrm{Eu}^{2+})}$ and $A_{(\mathrm{Eu}^{3+})}$ are the area of the corresponding subspectra and $f_{(\mathrm{Eu}^{2+})}$ and $f_{(\mathrm{Eu}^{3+})}$ are the Debye-Waller-factors of the corresponding ion.

The Debye-temperature θ_D of each of this ions is assumed to be the same for the three glasses. The Debye-temperature of Eu^{2+} was calculated from the values of the fluorozirconate glass N05-02-35B. The Eu^{2+} signal of the fluorozirconate glass ZBLAN 75 was extremely weak and with this the error bar is large. This can also be seen in the calculated area of the Eu^{2+} subspectra (Table 7.4). The value at 90 K is a little larger than that at 295 K which is unlikely. The results of N05-02-35B lead to a Debye-temperature of $\theta_D(Eu^{2+})$=154 K. The Debye-Temperature of Eu^{2+} was calculated from the values of the fluorozirconate glass N05-02-35B and ZBLAN 73. Since there a two slightly different values for the Debye-temperature of Eu^{3+} average value is calculated and an error estimation can be done. It follows a Debye-temperature of $\theta_D(\mathrm{Eu}^{3+})$=(215 $\pm$ 2) K. The values of the fluorozirconate glass ZBLAN 83 obtained from the 10 K spectra are not taken into account since this temperature does not comply the condition $T \geq \frac{\theta_D}{2}$ of the approximation.

With the Debye-temperatures we can calculate the f-factors and with this the Eu^{2+} / Eu^{3+} ration. The fluorozirconate glass ceramic ZBLAN 83 has with $R(\frac{\mathrm{Eu}^{2+}}{\mathrm{Eu}^{3+}}) = 0.65$ the lowest Eu^{2+} / Eu^{3+} ration of all investigate glass ceramics. In the case of the two other fluorozirconate glass ceramic the amount of Eu^{2+} is higher than that of Eu^{3+}. For the fluorozirconate glass ceramic ZBLAN 75 and N05-02-35B $R(\frac{\mathrm{Eu}^{2+}}{\mathrm{Eu}^{3+}}) = 1.4$ and 3.5, respectively.

4 Discussion

The ^{151}Eu Mössbauer spectra of Eu-doped $BaCl_2$ have a isomer shift of -13 mm/s and a broad linewidth of 17 mm/s (90 K) and 12 mm/s (10 K). From the Mössbauer investigation on Eu-doped CaF_2 we know that the broadening can be attributed to an unresolved hyperfine splitting. In an applied magnetic field of 0.2 mT two components can be observed on of them with an magnetic hyperfine field of 30 T.

Since the recording of a room temperature spectrum of Eu-doped $BaCl_2$ a determination of the Debye-temperature was not possible. The calculation of the Debye-temperature with equation 7.5 is only possible for $T \geq \frac{\theta_D}{2}$. The spectrum recorded at 10 K can not been taken into account. The fact that the recording of a room temperature spectrum was not possible leads to the assumption that the Debye-temperature is quite low.

These Mössbauer experiments by MacFarlane et al. [62] were recorded at room temperature. They observed an isomer shift of (-14.2$\pm$0.2) mm/s and a linewidth of (10.6$\pm$0.4) mm/s

for Eu^{2+} and an isomer shift of (-0.3±0.2) mm/s and a linewidth of (3.0±0.4) mm/s for Eu^{3+}. The observed isomer shifts for the divalent Eu of the investigated glass ceramics between -15.2 and -12.0 mm/s are in a good agreement. The linewidth values between 8.0 and 16.8 mm/s lie around the linewidth observed by MacFarlane et al. [62]. The variation of the values for the trivalent Eu is lower. The isomer shift between -0.5 and -0.4 mm/s is a little smaller than that observed by MacFarlane et al. [62]. The linewidth between 16 and 12 mm/s are in a good agreement.

The linewidth of Eu^{2+} in the fluorozirconate glasses is larger than for EuF_2 (2.98 mm/s) and Eu^{2+} in most other compounds [63]. The unusual broad linewidth of Eu^{2+} in the fluorozirconate glasses has also be observed by MacFarlane at al. [62] and Coey et al. [63]. Coey et al. [63] discuss beside other mechanisms a distribution of isomer shifts corresponding to Eu^{2+} in sites with different coordination numbers and Eu-F bond length as a possible mechanism for this broadening. For the investigated glass ceramic an additional isomer shift for Eu^{2+} in the $BaCl_2$ nanocrystals has to be added. Since the ^{151}Eu Mössbauer spectra of the Eu^{2+}-doped $BaCl_2$ also have unusual broad linewidth this may not the only mechanism. From the Mössbauer investigation on Eu-doped CaF_2 we know that the broadening can also be attributed to an unresolved hyperfine splitting.

The Eu^{2+}/ Eu^{3+} ratio by MacFarlane et al. [62] was determined by rating the areas of the single absorption lines for each valence state. Since the Mössbauer spectra were only recorded at room temperature the determination of the Debye-temperature and with this the f-factor was not possible. The calculated Eu^{2+}/ Eu^{3+} ration is a lower estimation of the Eu^{2+} fraction since the Debye-temperature of divalent Eu is lower than that of trivalent Eu. The Debye-temperatures for of Eu^{2+} and Eu^{3+} ions in the investigated glass ceramics were determined to $\theta_D^{2+} = 154$ K and $\theta_D^{3+} = 215$ K. Coey et al. [63] reported the effective Debye-temperatures for these two ions in similar fluorozirconate glass (ZrF_4-BaF_2-ThF_4): $\theta_D^{2+} = 145$ K and $\theta_D^{3+} = 261$ K.

With the two Debye-temperatures it was possible to determine the ratio between Eu^{2+} and Eu^{3+}. It can be seen that using purer EuF_2 leads to a higher concentration of Eu^{2+} in the glass. Unfortunately, it was not possible to determine between Eu^{2+} in the glass matrix and in the nanocrystals because the resolution of the spectra is not good enough.

[0]Most of the ^{151}Eu-Mössbauer spectra were recorded at the Northern Illinois University. The spectra of CaF_2 doped with 0.1% Eu were recorded at the University of Paderborn. The spectra of CaF_2 doped with 2% Eu with an external magnetic field of 6 T were recorded at the Argonne National Laboratories.

8 Conclusion

Eu-doped $BaCl_2$ was found to be the best scintillator (with respect to light yield, scintillation decay time, and afterglow) of the investigated Ce-, Eu-, and undoped barium halides. The light yield is 19,400 photons/MeV, the scintillation decay consists of a fast component on the submicrosecond scale (about 400 ns), and the afterglow is less than 0.2%. Moreover, the energy resolution under 662 keV γ-ray excitation of a ^{137}Cs source is 8.8%. Although undoped $BaBr_2$ is also a good scintillator in terms of light yield (19,300 photons/MeV), its scintillation decay component is 2.2 μs, which makes this system less attractive for scintillation applications. The XL-to-afterglow-ratio of undoped $BaBr_2$ is 1% to 2%; the energy resolution is 5.4% and thus slightly better than that of Eu-doped $BaCl_2$.

It was found that K-co-doping of Ce-doped single crystals and fluorozirconate based glass ceramics increases the Ce luminescence. Furthermore, the amount of host lattice luminescence observed in the 0.1% Ce-doped $BaBr_2$ sample decreases and the rise time in the scintillation decay curve gets faster when co-doping with K. These observations indicate that the Ce^{3+} excitation in the 0.1% Ce-doped $BaBr_2$ is delayed either due to energy migration processes from the ionization track to Ce^{3+}. Although we do not know what kind of migration process it is, it is clear that the observed scintillation decay is determined by both the Ce^{3+} $5d$ lifetime and the speed of migration/excitation. If the latter process is much slower than the Ce^{3+} $5d$ lifetime then the scintillation decay is fully controlled by the migration/transfer process. We assume that the defects involved in the migration processes are the same as the ones responsible for the host related emission bands at 420 and 480 nm. The 1% K-co-doping, however, causes a significant change in the scintillation behavior. The additional emission bands assigned to host lattice emission bands at 420 and 480 nm disappear and a fast decay component of 80 ns can now be found in the corresponding scintillation decay curve. It seems that the transfer from the host related defects to the Ce ions is much enhanced by K-co-doping. The host emission is quenched by the fast transfer to Ce, which results in more intense and faster Ce scintillation decay. The decay is still controlled by the migration/transfer process, but the lifetime of this process decreases to 80 ns. The intrinsic lifetime of the Ce^{3+} $5d$ state is expected to be significantly shorter than 80 ns; we anticipate a lifetime around 20-30 ns. An influence of the nanocrystals on the Ce emission wavelength can also be observed. The Ce doublet shifts to shorter wavelengths.

The investigated Sm- and Mn-doped singles crystals and fluorozirconate based glass ceramics turned out to be not very good scintillators. The Mn-doped samples have a very low luminescence signal upon x-ray and photo excitation. While the Mn-doped samples do not even fit the requirements of a fluorescence standard, the Sm-doped samples show

promising properties for the application as a fluorescence standard. Unfortunately, we had problems to reproduce the glass ceramics. However, we had problems in controlling the Sm charge state in the fluorozirconate based glasses. Most of the glasses containing Sm^{3+} instead of Sm^{2+} what is preferable for many applications.

The crystal field calculations show that the choice of the atomic position has an influence on the calculated crystal field. With the real atomic positions (upper three rows in Table 6.4) the c_2^0/c_2^2 ratio decreases from $BaCl_2$ via $BaBr_2$ to BaI_2. The calculations with atomic positions and an uniform expansion correction yield to an increasing c_2^0/c_2^2 ratio from $BaCl_2$ via $BaBr_2$ to BaI_2. In principle the detection of EPR spectra of Eu-doped BaI_2 is possible, but since the alignment of the Eu-doped BaI_2 single crystals was not possible the analysis was not possible either.

With the help of ^{151}Eu-Mössbauer spectroscopy it was possible to calculate the Debye-temperatures for of Eu^{2+} and Eu^{3+} ions in the investigated glass ceramics: $\theta_D^{2+} = 154$ K and $\theta_D^{3+} = 215$ K. And with this the ratio between Eu^{2+} and Eu^{3+} in the glass ceramics could be determined. The results show that the amount of Eu^{2+} can be increased by using better quality EuF_2. Unfortunately, it was not possible to distinguish between Eu^{2+} in the glass-matrix and in the $BaCl_2$ nanocrystals, because the resolution of the spectra is not good enough. The Mössbauer investigations on Eu-doped CaF_2 were primarily carried out for a better understanding of Mössbauer spectroscopy. The present observation of a large resolved paramagnetic hyperfine splitting with corresponding low relaxation times for 0.1% Eu in CaF_2 at room temperature is a new finding and offers immediately a new and consistent interpretation of the previous reported "anomalous" behavior of the Mössbauer isomer shift in the CaF_2:Eu system. A possibility to simulate Mössbauer spectra of highly diluted samples was found.

A The Stevens operators O_k^q

The spin Hamiltonian is given by [53]:

$$\begin{aligned}\mathscr{H} &= \underbrace{g\,\mu_B\,\mathbf{B}\,.\,\mathbf{S}}_{\text{electron Zeeman}} + \underbrace{B_4^0 O_4^0 + B_6^0 O_6^0 + B_6^4 O_6^4}_{\text{crystal field}} + \underbrace{A\,\mathbf{S}\,.\,\mathbf{I}}_{\text{hyperfine}} - \underbrace{g_N\,\mu_N\,\mathbf{B}\,.\,\mathbf{I}}_{\text{nuclear Zeemann}} \\ &= g\,\mu_B\,\mathbf{B}\,.\,\mathbf{S} + B_4(O_4^0 + 5O_4^4) + B_6(O_6^0 - 21O_6^4) + A\,\mathbf{S}\,.\,\mathbf{I} - g_N\,\mu_N\,\mathbf{B}\,.\,\mathbf{I} \\ &= g\,\mu_B\,\mathbf{B}\,.\,\mathbf{S} + \frac{1}{60}b_4(O_4^0 + 5O_4^4) + \frac{1}{1260}b_6(O_6^0 - 21O_6^4) + A\,\mathbf{S}\,.\,\mathbf{I} - g_N\,\mu_N\,\mathbf{B}\,.\,\mathbf{I}\end{aligned}$$

without an applied magnetic field the electron and nuclear Zeeman therm are negligible. In the following section the matrices for the Stevens operators and the hyperfine matrix of the ground and excited state are given.

1 The Stevens operators O_k^q

The following Stevens operators O_k^q for $J = 7/2$ are taken from [14].

$$O_4^0 = 60$$

m_J	$+\frac{7}{2}$	$+\frac{5}{2}$	$+\frac{3}{2}$	$+\frac{1}{2}$	$-\frac{1}{2}$	$-\frac{3}{2}$	$-\frac{5}{2}$	$-\frac{7}{2}$
$+\frac{7}{2}$	7	0	0	0	0	0	0	0
$+\frac{5}{2}$	0	−13	0	0	0	0	0	0
$+\frac{3}{2}$	0	0	−3	0	0	0	0	0
$+\frac{1}{2}$	0	0	0	9	0	0	0	0
$-\frac{1}{2}$	0	0	0	0	9	0	0	0
$-\frac{3}{2}$	0	0	0	0	0	−3	0	0
$-\frac{5}{2}$	0	0	0	0	0	0	−13	0
$-\frac{7}{2}$	0	0	0	0	0	0	0	7

$$O_4^4 = 12$$

m_J	$+\frac{7}{2}$	$+\frac{5}{2}$	$+\frac{3}{2}$	$+\frac{1}{2}$	$-\frac{1}{2}$	$-\frac{3}{2}$	$-\frac{5}{2}$	$-\frac{7}{2}$
$+\frac{7}{2}$	0	0	0	0	$\sqrt{35}$	0	0	0
$+\frac{5}{2}$	0	0	0	0	0	$5\sqrt{3}$	0	0
$+\frac{3}{2}$	0	0	0	0	0	0	$5\sqrt{3}$	0
$+\frac{1}{2}$	0	0	0	0	0	0	0	$\sqrt{35}$
$-\frac{1}{2}$	$\sqrt{35}$	0	0	0	0	0	0	0
$-\frac{3}{2}$	0	$5\sqrt{3}$	0	0	0	0	0	0
$-\frac{5}{2}$	0	0	$5\sqrt{3}$	0	0	0	0	0
$-\frac{7}{2}$	0	0	0	$\sqrt{35}$	0	0	0	0

$$O_6^0 = 1260$$

	$+\frac{7}{2}$	$+\frac{5}{2}$	$+\frac{3}{2}$	$+\frac{1}{2}$	$-\frac{1}{2}$	$-\frac{3}{2}$	$-\frac{5}{2}$	$-\frac{7}{2}$	m_J
$+\frac{7}{2}$	1	0	0	0	0	0	0	0	$+\frac{7}{2}$
$+\frac{5}{2}$	0	−5	0	0	0	0	0	0	$+\frac{5}{2}$
$+\frac{3}{2}$	0	0	9	0	0	0	0	0	$+\frac{3}{2}$
$+\frac{1}{2}$	0	0	0	−5	0	0	0	0	$+\frac{1}{2}$
$-\frac{1}{2}$	0	0	0	0	−5	0	0	0	$-\frac{1}{2}$
$-\frac{3}{2}$	0	0	0	0	0	9	0	0	$-\frac{3}{2}$
$-\frac{5}{2}$	0	0	0	0	0	0	−5	0	$-\frac{5}{2}$
$-\frac{7}{2}$	0	0	0	0	0	0	0	1	$-\frac{7}{2}$

$$O_6^4 = 60$$

	$+\frac{7}{2}$	$+\frac{5}{2}$	$+\frac{3}{2}$	$+\frac{1}{2}$	$-\frac{1}{2}$	$-\frac{3}{2}$	$-\frac{5}{2}$	$-\frac{7}{2}$	m_J
$+\frac{7}{2}$	0	0	0	0	$3\sqrt{35}$	0	0	0	$+\frac{7}{2}$
$+\frac{5}{2}$	0	0	0	0	0	$-7\sqrt{3}$	0	0	$+\frac{5}{2}$
$+\frac{3}{2}$	0	0	0	0	0	0	$-7\sqrt{3}$	0	$+\frac{3}{2}$
$+\frac{1}{2}$	0	0	0	0	0	0	0	$3\sqrt{35}$	$+\frac{1}{2}$
$-\frac{1}{2}$	$3\sqrt{35}$	0	0	0	0	0	0	0	$-\frac{1}{2}$
$-\frac{3}{2}$	0	$-7\sqrt{3}$	0	0	0	0	0	0	$-\frac{3}{2}$
$-\frac{5}{2}$	0	0	$-7\sqrt{3}$	0	0	0	0	0	$-\frac{5}{2}$
$-\frac{7}{2}$	0	0	0	$3\sqrt{35}$	0	0	0	0	$-\frac{7}{2}$

2 Hyperfine matrix of the ground state

Hence it follows for the matrix of the ground state.

$\langle m_S, m_I | \mathbf{S.I} | m'_S, m'_I \rangle =$

	$\lvert +\frac{7}{2}, m'_I \rangle$	$\lvert +\frac{5}{2}, m'_I \rangle$	$\lvert +\frac{3}{2}, m'_I \rangle$	$\lvert +\frac{1}{2}, m'_I \rangle$	$\lvert -\frac{1}{2}, m'_I \rangle$	$\lvert -\frac{3}{2}, m'_I \rangle$	$\lvert -\frac{5}{2}, m'_I \rangle$	$\lvert -\frac{7}{2}, m'_I \rangle$
$\langle +\frac{7}{2}, m_I \rvert$	A	B	0	0	0	0	0	0
$\langle +\frac{5}{2}, m_I \rvert$	C	D	E	0	0	0	0	0
$\langle +\frac{3}{2}, m_I \rvert$	0	F	G	H	0	0	0	0
$\langle +\frac{1}{2}, m_I \rvert$	0	0	J	K	L	0	0	0
$\langle -\frac{1}{2}, m_I \rvert$	0	0	0	M	N	O	0	0
$\langle -\frac{3}{2}, m_I \rvert$	0	0	0	0	P	Q	R	0
$\langle -\frac{5}{2}, m_I \rvert$	0	0	0	0	0	T	U	V
$\langle -\frac{7}{2}, m_I \rvert$	0	0	0	0	0	0	W	X

$$
\begin{array}{c}
 \\
\left\langle +\frac{7}{2},+\frac{5}{2}\right| \\
\left\langle +\frac{7}{2},+\frac{3}{2}\right| \\
\left\langle +\frac{7}{2},+\frac{1}{2}\right| \\
\left\langle +\frac{7}{2},-\frac{1}{2}\right| \\
\left\langle +\frac{7}{2},-\frac{3}{2}\right| \\
\left\langle +\frac{7}{2},-\frac{5}{2}\right|
\end{array}
\begin{array}{c}
\begin{array}{cccccc}
\left|+\frac{7}{2},+\frac{5}{2}\right\rangle & \left|+\frac{7}{2},+\frac{3}{2}\right\rangle & \left|+\frac{7}{2},+\frac{1}{2}\right\rangle & \left|+\frac{7}{2},-\frac{1}{2}\right\rangle & \left|+\frac{7}{2},-\frac{3}{2}\right\rangle & \left|+\frac{7}{2},-\frac{5}{2}\right\rangle
\end{array} \\
\left[\begin{array}{cccccc}
\frac{35}{4} & 0 & 0 & 0 & 0 & 0 \\
0 & \frac{21}{4} & 0 & 0 & 0 & 0 \\
0 & 0 & \frac{7}{4} & 0 & 0 & 0 \\
0 & 0 & 0 & -\frac{7}{4} & 0 & 0 \\
0 & 0 & 0 & 0 & -\frac{21}{4} & 0 \\
0 & 0 & 0 & 0 & 0 & -\frac{35}{4}
\end{array}\right] = A
\end{array}
$$

$$
\begin{array}{c}
 \\
\left\langle +\frac{7}{2},+\frac{5}{2}\right| \\
\left\langle +\frac{7}{2},+\frac{3}{2}\right| \\
\left\langle +\frac{7}{2},+\frac{1}{2}\right| \\
\left\langle +\frac{7}{2},-\frac{1}{2}\right| \\
\left\langle +\frac{7}{2},-\frac{3}{2}\right| \\
\left\langle +\frac{7}{2},-\frac{5}{2}\right|
\end{array}
\begin{array}{c}
\begin{array}{cccccc}
\left|+\frac{5}{2},+\frac{5}{2}\right\rangle & \left|+\frac{5}{2},+\frac{3}{2}\right\rangle & \left|+\frac{5}{2},+\frac{1}{2}\right\rangle & \left|+\frac{5}{2},-\frac{1}{2}\right\rangle & \left|+\frac{5}{2},-\frac{3}{2}\right\rangle & \left|+\frac{5}{2},-\frac{5}{2}\right\rangle
\end{array} \\
\left[\begin{array}{cccccc}
0 & 0 & 0 & 0 & 0 & 0 \\
\frac{1}{2}\sqrt{35} & 0 & 0 & 0 & 0 & 0 \\
0 & \sqrt{14} & 0 & 0 & 0 & 0 \\
0 & 0 & \frac{3}{2}\sqrt{7} & 0 & 0 & 0 \\
0 & 0 & 0 & \sqrt{14} & 0 & 0 \\
0 & 0 & 0 & 0 & \frac{1}{2}\sqrt{35} & 0
\end{array}\right] = B
\end{array}
$$

$$
\begin{array}{c}
\\
\left\langle +\frac{5}{2},+\frac{5}{2}\right| \\
\left\langle +\frac{5}{2},+\frac{3}{2}\right| \\
\left\langle +\frac{5}{2},+\frac{1}{2}\right| \\
\left\langle +\frac{5}{2},-\frac{1}{2}\right| \\
\left\langle +\frac{5}{2},-\frac{3}{2}\right| \\
\left\langle +\frac{5}{2},-\frac{5}{2}\right|
\end{array}
\begin{array}{c}
\left|+\frac{7}{2},+\frac{5}{2}\right\rangle \\
\hline
0 \\
0 \\
0 \\
0 \\
0 \\
0
\end{array}
\begin{array}{c}
\left|+\frac{7}{2},+\frac{3}{2}\right\rangle \\
\hline
\frac{1}{2}\sqrt{35} \\
0 \\
0 \\
0 \\
0 \\
0
\end{array}
\begin{array}{c}
\left|+\frac{7}{2},+\frac{1}{2}\right\rangle \\
\hline
0 \\
\sqrt{14} \\
0 \\
0 \\
0 \\
0
\end{array}
\begin{array}{c}
\left|+\frac{7}{2},-\frac{1}{2}\right\rangle \\
\hline
0 \\
0 \\
\frac{3}{2}\sqrt{7} \\
0 \\
0 \\
0
\end{array}
\begin{array}{c}
\left|+\frac{7}{2},-\frac{3}{2}\right\rangle \\
\hline
0 \\
0 \\
0 \\
\sqrt{14} \\
0 \\
0
\end{array}
\begin{array}{c}
\left|+\frac{7}{2},-\frac{5}{2}\right\rangle \\
\hline
0 \\
0 \\
0 \\
0 \\
\frac{1}{2}\sqrt{35} \\
0
\end{array}
= C
$$

$$
\begin{array}{c}
\\
\left\langle +\frac{5}{2},+\frac{5}{2}\right| \\
\left\langle +\frac{5}{2},+\frac{3}{2}\right| \\
\left\langle +\frac{5}{2},+\frac{1}{2}\right| \\
\left\langle +\frac{5}{2},-\frac{1}{2}\right| \\
\left\langle +\frac{5}{2},-\frac{3}{2}\right| \\
\left\langle +\frac{5}{2},-\frac{5}{2}\right|
\end{array}
\begin{array}{c}
\left|+\frac{5}{2},+\frac{5}{2}\right\rangle \\
\hline
\frac{25}{4} \\
0 \\
0 \\
0 \\
0 \\
0
\end{array}
\begin{array}{c}
\left|+\frac{5}{2},+\frac{3}{2}\right\rangle \\
\hline
0 \\
\frac{15}{4} \\
0 \\
0 \\
0 \\
0
\end{array}
\begin{array}{c}
\left|+\frac{5}{2},+\frac{1}{2}\right\rangle \\
\hline
0 \\
0 \\
\frac{5}{4} \\
0 \\
0 \\
0
\end{array}
\begin{array}{c}
\left|+\frac{5}{2},-\frac{1}{2}\right\rangle \\
\hline
0 \\
0 \\
0 \\
-\frac{5}{4} \\
0 \\
0
\end{array}
\begin{array}{c}
\left|+\frac{5}{2},-\frac{3}{2}\right\rangle \\
\hline
0 \\
0 \\
0 \\
0 \\
-\frac{15}{4} \\
0
\end{array}
\begin{array}{c}
\left|+\frac{5}{2},-\frac{5}{2}\right\rangle \\
\hline
0 \\
0 \\
0 \\
0 \\
0 \\
-\frac{25}{4}
\end{array}
= D
$$

$$
\begin{array}{c}
\\
\left\langle +\frac{5}{2},+\frac{5}{2}\right| \\
\left\langle +\frac{5}{2},+\frac{3}{2}\right| \\
\left\langle +\frac{5}{2},+\frac{1}{2}\right| \\
\left\langle +\frac{5}{2},-\frac{1}{2}\right| \\
\left\langle +\frac{5}{2},-\frac{3}{2}\right| \\
\left\langle +\frac{5}{2},-\frac{5}{2}\right|
\end{array}
\begin{array}{c}
\left|+\frac{3}{2},+\frac{5}{2}\right\rangle \\
\hline
0 \\
\sqrt{15} \\
0 \\
0 \\
0 \\
0
\end{array}
\begin{array}{c}
\left|+\frac{3}{2},+\frac{3}{2}\right\rangle \\
\hline
0 \\
0 \\
2\sqrt{6} \\
0 \\
0 \\
0
\end{array}
\begin{array}{c}
\left|+\frac{3}{2},+\frac{1}{2}\right\rangle \\
\hline
0 \\
0 \\
0 \\
3\sqrt{3} \\
0 \\
0
\end{array}
\begin{array}{c}
\left|+\frac{3}{2},-\frac{1}{2}\right\rangle \\
\hline
0 \\
0 \\
0 \\
0 \\
2\sqrt{6} \\
0
\end{array}
\begin{array}{c}
\left|+\frac{3}{2},-\frac{3}{2}\right\rangle \\
\hline
0 \\
0 \\
0 \\
0 \\
0 \\
\sqrt{15}
\end{array}
\begin{array}{c}
\left|+\frac{3}{2},-\frac{5}{2}\right\rangle \\
\hline
0 \\
0 \\
0 \\
0 \\
0 \\
0
\end{array}
= E
$$

$$
\begin{array}{c|cccccc}
 & \left|+\frac{5}{2},+\frac{5}{2}\right\rangle & \left|+\frac{5}{2},+\frac{3}{2}\right\rangle & \left|+\frac{5}{2},+\frac{1}{2}\right\rangle & \left|+\frac{5}{2},-\frac{1}{2}\right\rangle & \left|+\frac{5}{2},-\frac{3}{2}\right\rangle & \left|+\frac{5}{2},-\frac{5}{2}\right\rangle \\
\hline
\left\langle+\frac{3}{2},+\frac{5}{2}\right| & 0 & \sqrt{15} & 0 & 0 & 0 & 0 \\
\left\langle+\frac{5}{2},+\frac{3}{2}\right| & 0 & 0 & 2\sqrt{6} & 0 & 0 & 0 \\
\left\langle+\frac{5}{2},+\frac{1}{2}\right| & 0 & 0 & 0 & 3\sqrt{3} & 0 & 0 \\
\left\langle+\frac{3}{2},-\frac{1}{2}\right| & 0 & 0 & 0 & 0 & 2\sqrt{6} & 0 \\
\left\langle+\frac{5}{2},-\frac{3}{2}\right| & 0 & 0 & 0 & 0 & 0 & \sqrt{15} \\
\left\langle+\frac{3}{2},-\frac{5}{2}\right| & 0 & 0 & 0 & 0 & 0 & 0
\end{array}
= F
$$

$$
\begin{array}{c|cccccc}
 & \left|+\frac{3}{2},+\frac{5}{2}\right\rangle & \left|+\frac{3}{2},+\frac{3}{2}\right\rangle & \left|+\frac{3}{2},+\frac{1}{2}\right\rangle & \left|+\frac{3}{2},-\frac{1}{2}\right\rangle & \left|+\frac{3}{2},-\frac{3}{2}\right\rangle & \left|+\frac{3}{2},-\frac{5}{2}\right\rangle \\
\hline
\left\langle+\frac{3}{2},+\frac{5}{2}\right| & \frac{15}{4} & 0 & 0 & 0 & 0 & 0 \\
\left\langle+\frac{5}{2},+\frac{3}{2}\right| & 0 & \frac{9}{4} & 0 & 0 & 0 & 0 \\
\left\langle+\frac{5}{2},+\frac{1}{2}\right| & 0 & 0 & \frac{3}{4} & 0 & 0 & 0 \\
\left\langle+\frac{3}{2},-\frac{1}{2}\right| & 0 & 0 & 0 & -\frac{3}{4} & 0 & 0 \\
\left\langle+\frac{5}{2},-\frac{3}{2}\right| & 0 & 0 & 0 & 0 & -\frac{9}{4} & 0 \\
\left\langle+\frac{3}{2},-\frac{5}{2}\right| & 0 & 0 & 0 & 0 & 0 & -\frac{15}{4}
\end{array}
= G
$$

$$
\begin{array}{c|cccccc}
 & \left|+\frac{1}{2},+\frac{5}{2}\right\rangle & \left|+\frac{1}{2},+\frac{3}{2}\right\rangle & \left|+\frac{1}{2},+\frac{1}{2}\right\rangle & \left|+\frac{1}{2},-\frac{1}{2}\right\rangle & \left|+\frac{1}{2},-\frac{3}{2}\right\rangle & \left|+\frac{1}{2},-\frac{5}{2}\right\rangle \\
\hline
\left\langle+\frac{3}{2},+\frac{5}{2}\right| & 0 & 0 & 0 & 0 & 0 & 0 \\
\left\langle+\frac{5}{2},+\frac{3}{2}\right| & \frac{1}{2}\sqrt{75} & 0 & 0 & 0 & 0 & 0 \\
\left\langle+\frac{5}{2},+\frac{1}{2}\right| & 0 & \sqrt{30} & 0 & 0 & 0 & 0 \\
\left\langle+\frac{3}{2},-\frac{1}{2}\right| & 0 & 0 & \frac{3}{2}\sqrt{15} & 0 & 0 & 0 \\
\left\langle+\frac{5}{2},-\frac{3}{2}\right| & 0 & 0 & 0 & \sqrt{30} & 0 & 0 \\
\left\langle+\frac{3}{2},-\frac{5}{2}\right| & 0 & 0 & 0 & 0 & \frac{1}{2}\sqrt{75} & 0
\end{array}
= H
$$

$$
\begin{array}{c}
 \\
\langle +\frac{1}{2},+\frac{5}{2}| \\
\langle +\frac{1}{2},+\frac{3}{2}| \\
\langle +\frac{1}{2},+\frac{1}{2}| \\
\langle +\frac{1}{2},-\frac{1}{2}| \\
\langle +\frac{1}{2},-\frac{3}{2}| \\
\langle +\frac{1}{2},-\frac{5}{2}|
\end{array}
\begin{array}{c}
|+\frac{3}{2},+\frac{5}{2}\rangle \\
\left[\begin{array}{cccccc}
0 & \frac{1}{2}\sqrt{75} & 0 & 0 & 0 & 0 \\
0 & 0 & \sqrt{30} & 0 & 0 & 0 \\
0 & 0 & 0 & \frac{3}{2}\sqrt{15} & 0 & 0 \\
0 & 0 & 0 & 0 & \sqrt{30} & 0 \\
0 & 0 & 0 & 0 & 0 & \frac{1}{2}\sqrt{75} \\
0 & 0 & 0 & 0 & 0 & 0
\end{array}\right]
\end{array}
\begin{array}{c}
|+\frac{3}{2},+\frac{3}{2}\rangle \\
= J \\
|+\frac{1}{2},+\frac{5}{2}\rangle \\
\left[\begin{array}{cccccc}
\frac{5}{4} & 0 & 0 & 0 & 0 & 0 \\
0 & \frac{3}{4} & 0 & 0 & 0 & 0 \\
0 & 0 & \frac{1}{4} & 0 & 0 & 0 \\
0 & 0 & 0 & -\frac{1}{4} & 0 & 0 \\
0 & 0 & 0 & 0 & -\frac{3}{4} & 0 \\
0 & 0 & 0 & 0 & 0 & -\frac{5}{4}
\end{array}\right]
\end{array}
\begin{array}{c}
|+\frac{1}{2},+\frac{3}{2}\rangle \\
= K \\
|-\frac{1}{2},+\frac{5}{2}\rangle \\
\left[\begin{array}{cccccc}
0 & 0 & 0 & 0 & 0 & 0 \\
2\sqrt{5} & 0 & 0 & 0 & 0 & 0 \\
0 & 4\sqrt{2} & 0 & 0 & 0 & 0 \\
0 & 0 & 6 & 0 & 0 & 0 \\
0 & 0 & 0 & 4\sqrt{2} & 0 & 0 \\
0 & 0 & 0 & 0 & 2\sqrt{5} & 0
\end{array}\right]
\end{array}
\begin{array}{c}
|-\frac{1}{2},+\frac{3}{2}\rangle \\
= L \\
|+\frac{3}{2},-\frac{1}{2}\rangle \\
|+\frac{3}{2},-\frac{3}{2}\rangle \\
|+\frac{3}{2},-\frac{5}{2}\rangle \\
|+\frac{1}{2},-\frac{1}{2}\rangle \\
|+\frac{1}{2},-\frac{3}{2}\rangle \\
|+\frac{1}{2},-\frac{5}{2}\rangle \\
|-\frac{1}{2},-\frac{1}{2}\rangle \\
|-\frac{1}{2},-\frac{3}{2}\rangle \\
|-\frac{1}{2},-\frac{5}{2}\rangle
$$

$$
\begin{array}{c|cccccc}
 & |+\frac{1}{2},+\frac{5}{2}\rangle & |+\frac{1}{2},+\frac{3}{2}\rangle & |+\frac{1}{2},+\frac{1}{2}\rangle & |+\frac{1}{2},-\frac{1}{2}\rangle & |+\frac{1}{2},-\frac{3}{2}\rangle & |+\frac{1}{2},-\frac{5}{2}\rangle \\
\hline
\langle -\frac{1}{2},+\frac{5}{2}| & 0 & 2\sqrt{5} & 0 & 0 & 0 & 0 \\
\langle -\frac{1}{2},+\frac{3}{2}| & 0 & 0 & 4\sqrt{2} & 0 & 0 & 0 \\
\langle -\frac{1}{2},+\frac{1}{2}| & 0 & 0 & 0 & 6 & 0 & 0 \\
\langle -\frac{1}{2},-\frac{1}{2}| & 0 & 0 & 0 & 0 & 4\sqrt{2} & 0 \\
\langle -\frac{1}{2},-\frac{3}{2}| & 0 & 0 & 0 & 0 & 0 & 2\sqrt{5} \\
\langle -\frac{1}{2},-\frac{5}{2}| & 0 & 0 & 0 & 0 & 0 & 0
\end{array}
= M
$$

$$
\begin{array}{c|cccccc}
 & |-\frac{1}{2},+\frac{5}{2}\rangle & |-\frac{1}{2},+\frac{3}{2}\rangle & |-\frac{1}{2},+\frac{1}{2}\rangle & |-\frac{1}{2},-\frac{1}{2}\rangle & |-\frac{1}{2},-\frac{3}{2}\rangle & |-\frac{1}{2},-\frac{5}{2}\rangle \\
\hline
\langle -\frac{1}{2},+\frac{5}{2}| & -\frac{5}{4} & 0 & 0 & 0 & 0 & 0 \\
\langle -\frac{1}{2},+\frac{3}{2}| & 0 & -\frac{3}{4} & 0 & 0 & 0 & 0 \\
\langle -\frac{1}{2},+\frac{1}{2}| & 0 & 0 & -\frac{1}{4} & 0 & 0 & 0 \\
\langle -\frac{1}{2},-\frac{1}{2}| & 0 & 0 & 0 & \frac{1}{4} & 0 & 0 \\
\langle -\frac{1}{2},-\frac{3}{2}| & 0 & 0 & 0 & 0 & \frac{3}{4} & 0 \\
\langle -\frac{1}{2},-\frac{5}{2}| & 0 & 0 & 0 & 0 & 0 & \frac{5}{4}
\end{array}
= N
$$

$$
\begin{array}{c|cccccc}
 & |-\frac{3}{2},+\frac{5}{2}\rangle & |-\frac{3}{2},+\frac{3}{2}\rangle & |-\frac{3}{2},+\frac{1}{2}\rangle & |-\frac{3}{2},-\frac{1}{2}\rangle & |-\frac{3}{2},-\frac{3}{2}\rangle & |-\frac{3}{2},-\frac{5}{2}\rangle \\
\hline
\langle -\frac{1}{2},+\frac{5}{2}| & 0 & 0 & 0 & 0 & 0 & 0 \\
\langle -\frac{1}{2},+\frac{3}{2}| & \frac{1}{2}\sqrt{75} & 0 & 0 & 0 & 0 & 0 \\
\langle -\frac{1}{2},+\frac{1}{2}| & 0 & \sqrt{30} & 0 & 0 & 0 & 0 \\
\langle -\frac{1}{2},-\frac{1}{2}| & 0 & 0 & \frac{3}{2}\sqrt{15} & 0 & 0 & 0 \\
\langle -\frac{1}{2},-\frac{3}{2}| & 0 & 0 & 0 & \sqrt{30} & 0 & 0 \\
\langle -\frac{1}{2},-\frac{5}{2}| & 0 & 0 & 0 & 0 & \frac{1}{2}\sqrt{75} & 0
\end{array}
= O
$$

$$
\begin{array}{c}
\\
\left\langle -\frac{3}{2},+\frac{5}{2}\right| \\
\left\langle -\frac{3}{2},+\frac{3}{2}\right| \\
\left\langle -\frac{3}{2},+\frac{1}{2}\right| \\
\left\langle -\frac{3}{2},-\frac{1}{2}\right| \\
\left\langle -\frac{3}{2},-\frac{3}{2}\right| \\
\left\langle -\frac{3}{2},-\frac{5}{2}\right|
\end{array}
\begin{array}{c}
\begin{array}{cccccc}
\left|-\frac{1}{2},+\frac{5}{2}\right\rangle & \left|-\frac{1}{2},+\frac{3}{2}\right\rangle & \left|-\frac{1}{2},+\frac{1}{2}\right\rangle & \left|-\frac{1}{2},-\frac{1}{2}\right\rangle & \left|-\frac{1}{2},-\frac{3}{2}\right\rangle & \left|-\frac{1}{2},-\frac{5}{2}\right\rangle
\end{array} \\
\left[\begin{array}{cccccc}
0 & \frac{1}{2}\sqrt{75} & 0 & 0 & 0 & 0 \\
0 & 0 & \sqrt{30} & 0 & 0 & 0 \\
0 & 0 & 0 & \frac{3}{2}\sqrt{15} & 0 & 0 \\
0 & 0 & 0 & 0 & \sqrt{30} & 0 \\
0 & 0 & 0 & 0 & 0 & \frac{1}{2}\sqrt{75} \\
0 & 0 & 0 & 0 & 0 & 0
\end{array}\right]
\end{array}
= P
$$

$$
\begin{array}{c}
\\
\left\langle -\frac{3}{2},+\frac{5}{2}\right| \\
\left\langle -\frac{3}{2},+\frac{3}{2}\right| \\
\left\langle -\frac{3}{2},+\frac{1}{2}\right| \\
\left\langle -\frac{3}{2},-\frac{1}{2}\right| \\
\left\langle -\frac{3}{2},-\frac{3}{2}\right| \\
\left\langle -\frac{3}{2},-\frac{5}{2}\right|
\end{array}
\begin{array}{c}
\begin{array}{cccccc}
\left|-\frac{3}{2},+\frac{5}{2}\right\rangle & \left|-\frac{3}{2},+\frac{3}{2}\right\rangle & \left|-\frac{3}{2},+\frac{1}{2}\right\rangle & \left|-\frac{3}{2},-\frac{1}{2}\right\rangle & \left|-\frac{3}{2},-\frac{3}{2}\right\rangle & \left|-\frac{3}{2},-\frac{5}{2}\right\rangle
\end{array} \\
\left[\begin{array}{cccccc}
-\frac{15}{4} & 0 & 0 & 0 & 0 & 0 \\
0 & -\frac{9}{4} & 0 & 0 & 0 & 0 \\
0 & 0 & -\frac{3}{4} & 0 & 0 & 0 \\
0 & 0 & 0 & \frac{3}{4} & 0 & 0 \\
0 & 0 & 0 & 0 & \frac{9}{4} & 0 \\
0 & 0 & 0 & 0 & 0 & \frac{15}{4}
\end{array}\right]
\end{array}
= Q
$$

$$
\begin{array}{c}
\\
\left\langle -\frac{3}{2},+\frac{5}{2}\right| \\
\left\langle -\frac{3}{2},+\frac{3}{2}\right| \\
\left\langle -\frac{3}{2},+\frac{1}{2}\right| \\
\left\langle -\frac{3}{2},-\frac{1}{2}\right| \\
\left\langle -\frac{3}{2},-\frac{3}{2}\right| \\
\left\langle -\frac{3}{2},-\frac{5}{2}\right|
\end{array}
\begin{array}{c}
\begin{array}{cccccc}
\left|-\frac{5}{2},+\frac{5}{2}\right\rangle & \left|-\frac{5}{2},+\frac{3}{2}\right\rangle & \left|-\frac{5}{2},+\frac{1}{2}\right\rangle & \left|-\frac{5}{2},-\frac{1}{2}\right\rangle & \left|-\frac{5}{2},-\frac{3}{2}\right\rangle & \left|-\frac{5}{2},-\frac{5}{2}\right\rangle
\end{array} \\
\left[\begin{array}{cccccc}
0 & 0 & 0 & 0 & 0 & 0 \\
\sqrt{15} & 0 & 0 & 0 & 0 & 0 \\
0 & 2\sqrt{6} & 0 & 0 & 0 & 0 \\
0 & 0 & 3\sqrt{3} & 0 & 0 & 0 \\
0 & 0 & 0 & 2\sqrt{6} & 0 & 0 \\
0 & 0 & 0 & 0 & \sqrt{15} & 0
\end{array}\right]
\end{array}
= R
$$

$$
\begin{array}{c|cccccc}
 & \left|-\frac{3}{2},+\frac{5}{2}\right\rangle & \left|-\frac{3}{2},+\frac{3}{2}\right\rangle & \left|-\frac{3}{2},+\frac{1}{2}\right\rangle & \left|-\frac{3}{2},-\frac{1}{2}\right\rangle & \left|-\frac{3}{2},-\frac{3}{2}\right\rangle & \left|-\frac{3}{2},-\frac{5}{2}\right\rangle \\
\left\langle-\frac{5}{2},+\frac{5}{2}\right| & 0 & \sqrt{15} & 0 & 0 & 0 & 0 \\
\left\langle-\frac{5}{2},+\frac{3}{2}\right| & 0 & 0 & 2\sqrt{6} & 0 & 0 & 0 \\
\left\langle-\frac{5}{2},+\frac{1}{2}\right| & 0 & 0 & 0 & 3\sqrt{3} & 0 & 0 \\
\left\langle-\frac{5}{2},-\frac{1}{2}\right| & 0 & 0 & 0 & 0 & 2\sqrt{6} & 0 \\
\left\langle-\frac{5}{2},-\frac{3}{2}\right| & 0 & 0 & 0 & 0 & 0 & \sqrt{15} \\
\left\langle-\frac{5}{2},-\frac{5}{2}\right| & 0 & 0 & 0 & 0 & 0 & 0
\end{array}
= T
$$

$$
\begin{array}{c|cccccc}
 & \left|-\frac{5}{2},+\frac{5}{2}\right\rangle & \left|-\frac{5}{2},+\frac{3}{2}\right\rangle & \left|-\frac{5}{2},+\frac{1}{2}\right\rangle & \left|-\frac{5}{2},-\frac{1}{2}\right\rangle & \left|-\frac{5}{2},-\frac{3}{2}\right\rangle & \left|-\frac{5}{2},-\frac{5}{2}\right\rangle \\
\left\langle-\frac{5}{2},+\frac{5}{2}\right| & -\frac{25}{4} & 0 & 0 & 0 & 0 & 0 \\
\left\langle-\frac{5}{2},+\frac{3}{2}\right| & 0 & -\frac{15}{4} & 0 & 0 & 0 & 0 \\
\left\langle-\frac{5}{2},+\frac{1}{2}\right| & 0 & 0 & -\frac{5}{4} & 0 & 0 & 0 \\
\left\langle-\frac{5}{2},-\frac{1}{2}\right| & 0 & 0 & 0 & \frac{5}{4} & 0 & 0 \\
\left\langle-\frac{5}{2},-\frac{3}{2}\right| & 0 & 0 & 0 & 0 & \frac{15}{4} & 0 \\
\left\langle-\frac{5}{2},-\frac{5}{2}\right| & 0 & 0 & 0 & 0 & 0 & \frac{25}{4}
\end{array}
= U
$$

$$
\begin{array}{c|cccccc}
 & \left|-\frac{7}{2},+\frac{5}{2}\right\rangle & \left|-\frac{7}{2},+\frac{3}{2}\right\rangle & \left|-\frac{7}{2},+\frac{1}{2}\right\rangle & \left|-\frac{7}{2},-\frac{1}{2}\right\rangle & \left|-\frac{7}{2},-\frac{3}{2}\right\rangle & \left|-\frac{7}{2},-\frac{5}{2}\right\rangle \\
\left\langle-\frac{5}{2},+\frac{5}{2}\right| & 0 & 0 & 0 & 0 & 0 & 0 \\
\left\langle-\frac{5}{2},+\frac{3}{2}\right| & \frac{1}{2}\sqrt{35} & 0 & 0 & 0 & 0 & 0 \\
\left\langle-\frac{5}{2},+\frac{1}{2}\right| & 0 & \sqrt{14} & 0 & 0 & 0 & 0 \\
\left\langle-\frac{5}{2},-\frac{1}{2}\right| & 0 & 0 & \frac{3}{2}\sqrt{7} & 0 & 0 & 0 \\
\left\langle-\frac{5}{2},-\frac{3}{2}\right| & 0 & 0 & 0 & \sqrt{14} & 0 & 0 \\
\left\langle-\frac{5}{2},-\frac{5}{2}\right| & 0 & 0 & 0 & 0 & \frac{1}{2}\sqrt{35} & 0
\end{array}
= V
$$

$$
\begin{array}{c}
\\
\left\langle -\frac{7}{2},+\frac{5}{2}\right| \\
\left\langle -\frac{7}{2},+\frac{3}{2}\right| \\
\left\langle -\frac{7}{2},+\frac{1}{2}\right| \\
\left\langle -\frac{7}{2},-\frac{1}{2}\right| \\
\left\langle -\frac{7}{2},-\frac{3}{2}\right| \\
\left\langle -\frac{7}{2},-\frac{5}{2}\right|
\end{array}
\begin{array}{c}
\begin{array}{cccccc}
\left|-\frac{5}{2},+\frac{5}{2}\right\rangle & \left|-\frac{5}{2},+\frac{3}{2}\right\rangle & \left|-\frac{5}{2},+\frac{1}{2}\right\rangle & \left|-\frac{5}{2},-\frac{1}{2}\right\rangle & \left|-\frac{5}{2},-\frac{3}{2}\right\rangle & \left|-\frac{5}{2},-\frac{5}{2}\right\rangle
\end{array} \\
\left[\begin{array}{cccccc}
0 & \frac{1}{2}\sqrt{35} & 0 & 0 & 0 & 0 \\
0 & 0 & \sqrt{14} & 0 & 0 & 0 \\
0 & 0 & 0 & \frac{3}{2}\sqrt{7} & 0 & 0 \\
0 & 0 & 0 & 0 & \sqrt{14} & 0 \\
0 & 0 & 0 & 0 & 0 & \frac{1}{2}\sqrt{35} \\
0 & 0 & 0 & 0 & 0 & 0
\end{array}\right]
\end{array}
= W
$$

$$
\begin{array}{c}
\\
\left\langle -\frac{7}{2},+\frac{5}{2}\right| \\
\left\langle -\frac{7}{2},+\frac{3}{2}\right| \\
\left\langle -\frac{7}{2},+\frac{1}{2}\right| \\
\left\langle -\frac{7}{2},-\frac{1}{2}\right| \\
\left\langle -\frac{7}{2},-\frac{3}{2}\right| \\
\left\langle -\frac{7}{2},-\frac{5}{2}\right|
\end{array}
\begin{array}{c}
\begin{array}{cccccc}
\left|-\frac{7}{2},+\frac{5}{2}\right\rangle & \left|-\frac{7}{2},+\frac{3}{2}\right\rangle & \left|-\frac{7}{2},+\frac{1}{2}\right\rangle & \left|-\frac{7}{2},-\frac{1}{2}\right\rangle & \left|-\frac{7}{2},-\frac{3}{2}\right\rangle & \left|-\frac{7}{2},-\frac{5}{2}\right\rangle
\end{array} \\
\left[\begin{array}{cccccc}
-\frac{35}{4} & 0 & 0 & 0 & 0 & 0 \\
0 & -\frac{21}{4} & 0 & 0 & 0 & 0 \\
0 & 0 & -\frac{7}{4} & 0 & 0 & 0 \\
0 & 0 & 0 & \frac{7}{4} & 0 & 0 \\
0 & 0 & 0 & 0 & \frac{21}{4} & 0 \\
0 & 0 & 0 & 0 & 0 & \frac{35}{4}
\end{array}\right]
\end{array}
= X
$$

3 Hyperfine matrix of the excited state

The matrix of the excited state is given by

$$\langle m_S, m_{I^*} \,|\, \mathbf{S}.\mathbf{I}^* \,|\, m'_S, m'_{I^*} \rangle =$$

	$\lvert +\frac{7}{2}, m'_{I^*} \rangle$	$\lvert +\frac{5}{2}, m'_{I^*} \rangle$	$\lvert +\frac{3}{2}, m'_{I^*} \rangle$	$\lvert +\frac{1}{2}, m'_{I^*} \rangle$	$\lvert -\frac{1}{2}, m'_{I^*} \rangle$	$\lvert -\frac{3}{2}, m'_{I^*} \rangle$	$\lvert -\frac{5}{2}, m'_{I^*} \rangle$	$\lvert -\frac{7}{2}, m'_{I^*} \rangle$
$\langle +\frac{7}{2}, m_{I^*} \rvert$	A^*	B^*	0	0	0	0	0	0
$\langle +\frac{5}{2}, m_{I^*} \rvert$	C^*	D^*	E^*	0	0	0	0	0
$\langle +\frac{3}{2}, m_{I^*} \rvert$	0	F^*	G^*	H^*	0	0	0	0
$\langle +\frac{1}{2}, m_{I^*} \rvert$	0	0	J^*	K^*	L^*	0	0	0
$\langle -\frac{1}{2}, m_{I^*} \rvert$	0	0	0	M^*	N^*	O^*	0	0
$\langle -\frac{3}{2}, m_{I^*} \rvert$	0	0	0	0	P^*	Q^*	R^*	0
$\langle -\frac{5}{2}, m_{I^*} \rvert$	0	0	0	0	0	T^*	U^*	V^*
$\langle -\frac{7}{2}, m_{I^*} \rvert$	0	0	0	0	0	0	W^*	X^*

$$
\begin{array}{c}
\\
\langle +\frac{7}{2},+\frac{7}{2}| \\
\langle +\frac{7}{2},+\frac{5}{2}| \\
\langle +\frac{7}{2},+\frac{3}{2}| \\
\langle +\frac{7}{2},+\frac{1}{2}| \\
\langle +\frac{7}{2},-\frac{1}{2}| \\
\langle +\frac{7}{2},-\frac{3}{2}| \\
\langle +\frac{7}{2},-\frac{5}{2}| \\
\langle +\frac{7}{2},-\frac{7}{2}|
\end{array}
\begin{array}{c}
\begin{array}{cccccccc}
|+\frac{7}{2},+\frac{7}{2}\rangle & |+\frac{7}{2},+\frac{5}{2}\rangle & |+\frac{7}{2},+\frac{3}{2}\rangle & |+\frac{7}{2},+\frac{1}{2}\rangle & |+\frac{7}{2},-\frac{1}{2}\rangle & |+\frac{7}{2},-\frac{3}{2}\rangle & |+\frac{7}{2},-\frac{5}{2}\rangle & |+\frac{7}{2},-\frac{7}{2}\rangle
\end{array} \\
\left[\begin{array}{cccccccc}
\frac{49}{4} & 0 & 0 & 0 & 0 & 0 & 0 & 0 \\
0 & \frac{35}{4} & 0 & 0 & 0 & 0 & 0 & 0 \\
0 & 0 & \frac{21}{4} & 0 & 0 & 0 & 0 & 0 \\
0 & 0 & 0 & \frac{7}{4} & 0 & 0 & 0 & 0 \\
0 & 0 & 0 & 0 & -\frac{7}{4} & 0 & 0 & 0 \\
0 & 0 & 0 & 0 & 0 & -\frac{21}{4} & 0 & 0 \\
0 & 0 & 0 & 0 & 0 & 0 & -\frac{35}{4} & 0 \\
0 & 0 & 0 & 0 & 0 & 0 & 0 & -\frac{49}{4}
\end{array}\right] \\
= A^*
\end{array}
$$

$$
\begin{array}{c}
\\
\langle +\frac{7}{2},+\frac{7}{2}| \\
\langle +\frac{7}{2},+\frac{5}{2}| \\
\langle +\frac{7}{2},+\frac{3}{2}| \\
\langle +\frac{7}{2},+\frac{1}{2}| \\
\langle +\frac{7}{2},-\frac{1}{2}| \\
\langle +\frac{7}{2},-\frac{3}{2}| \\
\langle +\frac{7}{2},-\frac{5}{2}| \\
\langle +\frac{7}{2},-\frac{7}{2}|
\end{array}
\begin{array}{c}
\begin{array}{cccccccc}
|+\frac{5}{2},+\frac{7}{2}\rangle & |+\frac{5}{2},+\frac{5}{2}\rangle & |+\frac{5}{2},+\frac{3}{2}\rangle & |+\frac{5}{2},+\frac{1}{2}\rangle & |+\frac{5}{2},-\frac{1}{2}\rangle & |+\frac{5}{2},-\frac{3}{2}\rangle & |+\frac{5}{2},-\frac{5}{2}\rangle & |+\frac{5}{2},-\frac{7}{2}\rangle
\end{array} \\
\left[\begin{array}{cccccccc}
0 & 0 & 0 & 0 & 0 & 0 & 0 & 0 \\
\frac{7}{2} & 0 & 0 & 0 & 0 & 0 & 0 & 0 \\
0 & \sqrt{21} & 0 & 0 & 0 & 0 & 0 & 0 \\
0 & 0 & \frac{1}{2}\sqrt{105} & 0 & 0 & 0 & 0 & 0 \\
0 & 0 & 0 & 2\sqrt{7} & 0 & 0 & 0 & 0 \\
0 & 0 & 0 & 0 & \frac{1}{2}\sqrt{105} & 0 & 0 & 0 \\
0 & 0 & 0 & 0 & 0 & \sqrt{21} & 0 & 0 \\
0 & 0 & 0 & 0 & 0 & 0 & \frac{7}{2} & 0
\end{array}\right] \\
= B^*
\end{array}
$$

$$
\begin{array}{c}
\\
\langle +\frac{5}{2},+\frac{7}{2}| \\
\langle +\frac{5}{2},+\frac{5}{2}| \\
\langle +\frac{5}{2},+\frac{3}{2}| \\
\langle +\frac{5}{2},+\frac{1}{2}| \\
\langle +\frac{5}{2},-\frac{1}{2}| \\
\langle +\frac{5}{2},-\frac{3}{2}| \\
\langle +\frac{5}{2},-\frac{5}{2}| \\
\langle +\frac{5}{2},-\frac{7}{2}|
\end{array}
\begin{array}{c}
\begin{array}{cccccccc}
|+\frac{7}{2},+\frac{7}{2}\rangle & |+\frac{7}{2},+\frac{5}{2}\rangle & |+\frac{7}{2},+\frac{3}{2}\rangle & |+\frac{7}{2},+\frac{1}{2}\rangle & |+\frac{7}{2},-\frac{1}{2}\rangle & |+\frac{7}{2},-\frac{3}{2}\rangle & |+\frac{7}{2},-\frac{5}{2}\rangle & |+\frac{7}{2},-\frac{7}{2}\rangle
\end{array} \\
\left[\begin{array}{cccccccc}
0 & \frac{7}{2} & 0 & 0 & 0 & 0 & 0 & 0 \\
0 & 0 & \sqrt{21} & 0 & 0 & 0 & 0 & 0 \\
0 & 0 & 0 & \frac{1}{2}\sqrt{105} & 0 & 0 & 0 & 0 \\
0 & 0 & 0 & 0 & 2\sqrt{7} & 0 & 0 & 0 \\
0 & 0 & 0 & 0 & 0 & \frac{1}{2}\sqrt{105} & 0 & 0 \\
0 & 0 & 0 & 0 & 0 & 0 & \sqrt{21} & 0 \\
0 & 0 & 0 & 0 & 0 & 0 & 0 & \frac{7}{2} \\
0 & 0 & 0 & 0 & 0 & 0 & 0 & 0
\end{array}\right] \\
= C^*
\end{array}
$$

$$
\begin{array}{c}
\\
\left\langle +\frac{5}{2},+\frac{7}{2}\right| \\
\left\langle +\frac{5}{2},+\frac{5}{2}\right| \\
\left\langle +\frac{5}{2},+\frac{3}{2}\right| \\
\left\langle +\frac{5}{2},+\frac{1}{2}\right| \\
\left\langle +\frac{5}{2},-\frac{1}{2}\right| \\
\left\langle +\frac{5}{2},-\frac{3}{2}\right| \\
\left\langle +\frac{5}{2},-\frac{5}{2}\right| \\
\left\langle +\frac{5}{2},-\frac{7}{2}\right|
\end{array}
\begin{array}{c}
\left|+\frac{5}{2},+\frac{7}{2}\right\rangle \\
\hline
\frac{35}{4} \\
0 \\
0 \\
0 \\
0 \\
0 \\
0 \\
0
\end{array}
\begin{array}{c}
\left|+\frac{5}{2},+\frac{5}{2}\right\rangle \\
\hline
0 \\
\frac{25}{4} \\
0 \\
0 \\
0 \\
0 \\
0 \\
0
\end{array}
\begin{array}{c}
\left|+\frac{5}{2},+\frac{3}{2}\right\rangle \\
\hline
0 \\
0 \\
\frac{15}{4} \\
0 \\
0 \\
0 \\
0 \\
0
\end{array}
\begin{array}{c}
\left|+\frac{5}{2},+\frac{1}{2}\right\rangle \\
\hline
0 \\
0 \\
0 \\
\frac{5}{4} \\
0 \\
0 \\
0 \\
0
\end{array}
\begin{array}{c}
\left|+\frac{5}{2},-\frac{1}{2}\right\rangle \\
\hline
0 \\
0 \\
0 \\
0 \\
-\frac{5}{4} \\
0 \\
0 \\
0
\end{array}
\begin{array}{c}
\left|+\frac{5}{2},-\frac{3}{2}\right\rangle \\
\hline
0 \\
0 \\
0 \\
0 \\
0 \\
-\frac{15}{4} \\
0 \\
0
\end{array}
\begin{array}{c}
\left|+\frac{5}{2},-\frac{5}{2}\right\rangle \\
\hline
0 \\
0 \\
0 \\
0 \\
0 \\
0 \\
-\frac{25}{4} \\
0
\end{array}
\begin{array}{c}
\left|+\frac{5}{2},-\frac{7}{2}\right\rangle \\
\hline
0 \\
0 \\
0 \\
0 \\
0 \\
0 \\
0 \\
-\frac{35}{4}
\end{array}
= D^*
$$

$$
\begin{array}{c}
\\
\left\langle +\frac{5}{2},+\frac{7}{2}\right| \\
\left\langle +\frac{5}{2},+\frac{5}{2}\right| \\
\left\langle +\frac{5}{2},+\frac{3}{2}\right| \\
\left\langle +\frac{5}{2},+\frac{1}{2}\right| \\
\left\langle +\frac{5}{2},-\frac{1}{2}\right| \\
\left\langle +\frac{5}{2},-\frac{3}{2}\right| \\
\left\langle +\frac{5}{2},-\frac{5}{2}\right| \\
\left\langle +\frac{5}{2},-\frac{7}{2}\right|
\end{array}
\begin{array}{c}
\left|+\frac{3}{2},+\frac{7}{2}\right\rangle \\
\hline
0 \\
\sqrt{21} \\
0 \\
0 \\
0 \\
0 \\
0 \\
0
\end{array}
\begin{array}{c}
\left|+\frac{3}{2},+\frac{5}{2}\right\rangle \\
\hline
0 \\
0 \\
6 \\
0 \\
0 \\
0 \\
0 \\
0
\end{array}
\begin{array}{c}
\left|+\frac{3}{2},+\frac{3}{2}\right\rangle \\
\hline
0 \\
0 \\
0 \\
3\sqrt{5} \\
0 \\
0 \\
0 \\
0
\end{array}
\begin{array}{c}
\left|+\frac{3}{2},+\frac{1}{2}\right\rangle \\
\hline
0 \\
0 \\
0 \\
0 \\
4\sqrt{3} \\
0 \\
0 \\
0
\end{array}
\begin{array}{c}
\left|+\frac{3}{2},-\frac{1}{2}\right\rangle \\
\hline
0 \\
0 \\
0 \\
0 \\
0 \\
3\sqrt{5} \\
0 \\
0
\end{array}
\begin{array}{c}
\left|+\frac{3}{2},-\frac{3}{2}\right\rangle \\
\hline
0 \\
0 \\
0 \\
0 \\
0 \\
0 \\
6 \\
0
\end{array}
\begin{array}{c}
\left|+\frac{3}{2},-\frac{5}{2}\right\rangle \\
\hline
0 \\
0 \\
0 \\
0 \\
0 \\
0 \\
0 \\
\sqrt{21}
\end{array}
\begin{array}{c}
\left|+\frac{3}{2},-\frac{7}{2}\right\rangle \\
\hline
0 \\
0 \\
0 \\
0 \\
0 \\
0 \\
0 \\
0
\end{array}
= E^*
$$

$$
\begin{array}{c}
\\
\left\langle +\frac{3}{2},+\frac{7}{2}\right| \\
\left\langle +\frac{3}{2},+\frac{5}{2}\right| \\
\left\langle +\frac{3}{2},+\frac{3}{2}\right| \\
\left\langle +\frac{3}{2},+\frac{1}{2}\right| \\
\left\langle +\frac{3}{2},-\frac{1}{2}\right| \\
\left\langle +\frac{3}{2},-\frac{3}{2}\right| \\
\left\langle +\frac{3}{2},-\frac{5}{2}\right| \\
\left\langle +\frac{3}{2},-\frac{7}{2}\right|
\end{array}
\begin{array}{c}
\left|+\frac{5}{2},+\frac{7}{2}\right\rangle \\
\hline
0 \\
\sqrt{21} \\
0 \\
0 \\
0 \\
0 \\
0 \\
0
\end{array}
\begin{array}{c}
\left|+\frac{5}{2},+\frac{5}{2}\right\rangle \\
\hline
\sqrt{21} \\
0 \\
6 \\
0 \\
0 \\
0 \\
0 \\
0
\end{array}
\begin{array}{c}
\left|+\frac{5}{2},+\frac{3}{2}\right\rangle \\
\hline
0 \\
6 \\
0 \\
0 \\
0 \\
0 \\
0 \\
0
\end{array}
\begin{array}{c}
\left|+\frac{5}{2},+\frac{1}{2}\right\rangle \\
\hline
0 \\
0 \\
3\sqrt{5} \\
0 \\
0 \\
0 \\
0 \\
0
\end{array}
\begin{array}{c}
\left|+\frac{5}{2},-\frac{1}{2}\right\rangle \\
\hline
0 \\
0 \\
0 \\
4\sqrt{3} \\
0 \\
0 \\
0 \\
0
\end{array}
\begin{array}{c}
\left|+\frac{5}{2},-\frac{3}{2}\right\rangle \\
\hline
0 \\
0 \\
0 \\
0 \\
3\sqrt{5} \\
0 \\
0 \\
0
\end{array}
\begin{array}{c}
\left|+\frac{5}{2},-\frac{5}{2}\right\rangle \\
\hline
0 \\
0 \\
0 \\
0 \\
0 \\
6 \\
0 \\
0
\end{array}
\begin{array}{c}
\left|+\frac{5}{2},-\frac{7}{2}\right\rangle \\
\hline
0 \\
0 \\
0 \\
0 \\
0 \\
0 \\
0 \\
\sqrt{21}
\end{array}
= F^*
$$

$$
\begin{array}{c}
\\
\langle +\frac{3}{2},+\frac{7}{2}| \\
\langle +\frac{3}{2},+\frac{5}{2}| \\
\langle +\frac{3}{2},+\frac{3}{2}| \\
\langle +\frac{3}{2},+\frac{1}{2}| \\
\langle +\frac{3}{2},-\frac{1}{2}| \\
\langle +\frac{3}{2},-\frac{3}{2}| \\
\langle +\frac{3}{2},-\frac{5}{2}| \\
\langle +\frac{3}{2},-\frac{7}{2}|
\end{array}
\begin{array}{c}
\begin{array}{cccccccc}
|+\frac{3}{2},+\frac{7}{2}\rangle & |+\frac{3}{2},+\frac{5}{2}\rangle & |+\frac{3}{2},+\frac{3}{2}\rangle & |+\frac{3}{2},+\frac{1}{2}\rangle & |+\frac{3}{2},-\frac{1}{2}\rangle & |+\frac{3}{2},-\frac{3}{2}\rangle & |+\frac{3}{2},-\frac{5}{2}\rangle & |+\frac{3}{2},-\frac{7}{2}\rangle
\end{array} \\
\left[\begin{array}{cccccccc}
\frac{21}{4} & 0 & 0 & 0 & 0 & 0 & 0 & 0 \\
0 & \frac{15}{4} & 0 & 0 & 0 & 0 & 0 & 0 \\
0 & 0 & \frac{9}{4} & 0 & 0 & 0 & 0 & 0 \\
0 & 0 & 0 & \frac{3}{4} & 0 & 0 & 0 & 0 \\
0 & 0 & 0 & 0 & -\frac{3}{4} & 0 & 0 & 0 \\
0 & 0 & 0 & 0 & 0 & -\frac{9}{4} & 0 & 0 \\
0 & 0 & 0 & 0 & 0 & 0 & -\frac{15}{4} & 0 \\
0 & 0 & 0 & 0 & 0 & 0 & 0 & -\frac{21}{4}
\end{array}\right] \\
= G^*
\end{array}
$$

$$
\begin{array}{c}
\\
\langle +\frac{3}{2},+\frac{7}{2}| \\
\langle +\frac{3}{2},+\frac{5}{2}| \\
\langle +\frac{3}{2},+\frac{3}{2}| \\
\langle +\frac{3}{2},+\frac{1}{2}| \\
\langle +\frac{3}{2},-\frac{1}{2}| \\
\langle +\frac{3}{2},-\frac{3}{2}| \\
\langle +\frac{3}{2},-\frac{5}{2}| \\
\langle +\frac{3}{2},-\frac{7}{2}|
\end{array}
\begin{array}{c}
\begin{array}{cccccccc}
|+\frac{1}{2},+\frac{7}{2}\rangle & |+\frac{1}{2},+\frac{5}{2}\rangle & |+\frac{1}{2},+\frac{3}{2}\rangle & |+\frac{1}{2},+\frac{1}{2}\rangle & |+\frac{1}{2},-\frac{1}{2}\rangle & |+\frac{1}{2},-\frac{3}{2}\rangle & |+\frac{1}{2},-\frac{5}{2}\rangle & |+\frac{1}{2},-\frac{7}{2}\rangle
\end{array} \\
\left[\begin{array}{cccccccc}
0 & 0 & 0 & 0 & 0 & 0 & 0 & 0 \\
\frac{1}{2}\sqrt{105} & 0 & 0 & 0 & 0 & 0 & 0 & 0 \\
0 & 3\sqrt{5} & 0 & 0 & 0 & 0 & 0 & 0 \\
0 & 0 & \frac{15}{2} & 0 & 0 & 0 & 0 & 0 \\
0 & 0 & 0 & 2\sqrt{15} & 0 & 0 & 0 & 0 \\
0 & 0 & 0 & 0 & \frac{15}{2} & 0 & 0 & 0 \\
0 & 0 & 0 & 0 & 0 & 3\sqrt{5} & 0 & 0 \\
0 & 0 & 0 & 0 & 0 & 0 & \frac{1}{2}\sqrt{105} & 0
\end{array}\right] \\
= H^*
\end{array}
$$

$$
\begin{array}{c}
\\
\langle +\frac{3}{2},+\frac{7}{2}| \\
\langle +\frac{1}{2},+\frac{5}{2}| \\
\langle +\frac{1}{2},+\frac{3}{2}| \\
\langle +\frac{1}{2},+\frac{1}{2}| \\
\langle +\frac{1}{2},-\frac{1}{2}| \\
\langle +\frac{1}{2},-\frac{3}{2}| \\
\langle +\frac{1}{2},-\frac{5}{2}| \\
\langle +\frac{1}{2},-\frac{7}{2}|
\end{array}
\begin{array}{c}
\begin{array}{cccccccc}
|+\frac{3}{2},+\frac{7}{2}\rangle & |+\frac{3}{2},+\frac{5}{2}\rangle & |+\frac{3}{2},+\frac{3}{2}\rangle & |+\frac{3}{2},+\frac{1}{2}\rangle & |+\frac{3}{2},-\frac{1}{2}\rangle & |+\frac{3}{2},-\frac{3}{2}\rangle & |+\frac{3}{2},-\frac{5}{2}\rangle & |+\frac{3}{2},-\frac{7}{2}\rangle
\end{array} \\
\left[\begin{array}{cccccccc}
0 & \frac{1}{2}\sqrt{105} & 0 & 0 & 0 & 0 & 0 & 0 \\
0 & 0 & 3\sqrt{5} & 0 & 0 & 0 & 0 & 0 \\
0 & 0 & 0 & \frac{15}{2} & 0 & 0 & 0 & 0 \\
0 & 0 & 0 & 0 & 2\sqrt{15} & 0 & 0 & 0 \\
0 & 0 & 0 & 0 & 0 & \frac{15}{2} & 0 & 0 \\
0 & 0 & 0 & 0 & 0 & 0 & 3\sqrt{5} & 0 \\
0 & 0 & 0 & 0 & 0 & 0 & 0 & \frac{1}{2}\sqrt{105} \\
0 & 0 & 0 & 0 & 0 & 0 & 0 & 0
\end{array}\right] \\
= I^*
\end{array}
$$

$$
\begin{array}{c|cccccccc}
 & |+\frac{1}{2},+\frac{7}{2}\rangle & |+\frac{1}{2},+\frac{5}{2}\rangle & |+\frac{1}{2},+\frac{3}{2}\rangle & |+\frac{1}{2},+\frac{1}{2}\rangle & |+\frac{1}{2},-\frac{1}{2}\rangle & |+\frac{1}{2},-\frac{3}{2}\rangle & |+\frac{1}{2},-\frac{5}{2}\rangle & |+\frac{1}{2},-\frac{7}{2}\rangle \\
\hline
\langle +\frac{1}{2},+\frac{7}{2}| & \frac{7}{4} & 0 & 0 & 0 & 0 & 0 & 0 & 0 \\
\langle +\frac{1}{2},+\frac{5}{2}| & 0 & \frac{5}{4} & 0 & 0 & 0 & 0 & 0 & 0 \\
\langle +\frac{1}{2},+\frac{3}{2}| & 0 & 0 & \frac{3}{4} & 0 & 0 & 0 & 0 & 0 \\
\langle +\frac{1}{2},+\frac{1}{2}| & 0 & 0 & 0 & \frac{1}{4} & 0 & 0 & 0 & 0 \\
\langle +\frac{1}{2},-\frac{1}{2}| & 0 & 0 & 0 & 0 & -\frac{1}{4} & 0 & 0 & 0 \\
\langle +\frac{1}{2},-\frac{3}{2}| & 0 & 0 & 0 & 0 & 0 & -\frac{3}{4} & 0 & 0 \\
\langle +\frac{1}{2},-\frac{5}{2}| & 0 & 0 & 0 & 0 & 0 & 0 & -\frac{5}{4} & 0 \\
\langle +\frac{1}{2},-\frac{7}{2}| & 0 & 0 & 0 & 0 & 0 & 0 & 0 & -\frac{7}{4}
\end{array}
= K^*
$$

$$
\begin{array}{c|cccccccc}
 & |-\frac{1}{2},+\frac{7}{2}\rangle & |-\frac{1}{2},+\frac{5}{2}\rangle & |-\frac{1}{2},+\frac{3}{2}\rangle & |-\frac{1}{2},+\frac{1}{2}\rangle & |-\frac{1}{2},-\frac{1}{2}\rangle & |-\frac{1}{2},-\frac{3}{2}\rangle & |-\frac{1}{2},-\frac{5}{2}\rangle & |-\frac{1}{2},-\frac{7}{2}\rangle \\
\hline
\langle +\frac{1}{2},+\frac{7}{2}| & 0 & 0 & 0 & 0 & 0 & 0 & 0 & 0 \\
\langle +\frac{1}{2},+\frac{5}{2}| & 2\sqrt{7} & 0 & 0 & 0 & 0 & 0 & 0 & 0 \\
\langle +\frac{1}{2},+\frac{3}{2}| & 0 & 4\sqrt{3} & 0 & 0 & 0 & 0 & 0 & 0 \\
\langle +\frac{1}{2},+\frac{1}{2}| & 0 & 0 & 2\sqrt{15} & 0 & 0 & 0 & 0 & 0 \\
\langle +\frac{1}{2},-\frac{1}{2}| & 0 & 0 & 0 & 8 & 0 & 0 & 0 & 0 \\
\langle +\frac{1}{2},-\frac{3}{2}| & 0 & 0 & 0 & 0 & 2\sqrt{15} & 0 & 0 & 0 \\
\langle +\frac{1}{2},-\frac{5}{2}| & 0 & 0 & 0 & 0 & 0 & 4\sqrt{3} & 0 & 0 \\
\langle +\frac{1}{2},-\frac{7}{2}| & 0 & 0 & 0 & 0 & 0 & 0 & 2\sqrt{7} & 0
\end{array}
= L^*
$$

$$
\begin{array}{c|cccccccc}
 & |+\frac{1}{2},+\frac{7}{2}\rangle & |+\frac{1}{2},+\frac{5}{2}\rangle & |+\frac{1}{2},+\frac{3}{2}\rangle & |+\frac{1}{2},+\frac{1}{2}\rangle & |+\frac{1}{2},-\frac{1}{2}\rangle & |+\frac{1}{2},-\frac{3}{2}\rangle & |+\frac{1}{2},-\frac{5}{2}\rangle & |+\frac{1}{2},-\frac{7}{2}\rangle \\
\hline
\langle -\frac{1}{2},+\frac{7}{2}| & 0 & 2\sqrt{7} & 0 & 0 & 0 & 0 & 0 & 0 \\
\langle -\frac{1}{2},+\frac{5}{2}| & 0 & 0 & 4\sqrt{3} & 0 & 0 & 0 & 0 & 0 \\
\langle -\frac{1}{2},+\frac{3}{2}| & 0 & 0 & 0 & 2\sqrt{15} & 0 & 0 & 0 & 0 \\
\langle -\frac{1}{2},+\frac{1}{2}| & 0 & 0 & 0 & 0 & 8 & 0 & 0 & 0 \\
\langle -\frac{1}{2},-\frac{1}{2}| & 0 & 0 & 0 & 0 & 0 & 2\sqrt{15} & 0 & 0 \\
\langle -\frac{1}{2},-\frac{3}{2}| & 0 & 0 & 0 & 0 & 0 & 0 & 4\sqrt{3} & 0 \\
\langle -\frac{1}{2},-\frac{5}{2}| & 0 & 0 & 0 & 0 & 0 & 0 & 0 & 2\sqrt{7} \\
\langle -\frac{1}{2},-\frac{7}{2}| & 0 & 0 & 0 & 0 & 0 & 0 & 0 & 0
\end{array}
= M^*
$$

$$
\begin{array}{c|cccccccc}
 & |-\frac{1}{2},+\frac{7}{2}\rangle & |-\frac{1}{2},+\frac{5}{2}\rangle & |-\frac{1}{2},+\frac{3}{2}\rangle & |-\frac{1}{2},+\frac{1}{2}\rangle & |-\frac{1}{2},-\frac{1}{2}\rangle & |-\frac{1}{2},-\frac{3}{2}\rangle & |-\frac{1}{2},-\frac{5}{2}\rangle & |-\frac{1}{2},-\frac{7}{2}\rangle \\
\hline
\langle -\frac{1}{2},+\frac{7}{2}| & -\frac{7}{4} & 0 & 0 & 0 & 0 & 0 & 0 & 0 \\
\langle -\frac{1}{2},+\frac{5}{2}| & 0 & -\frac{5}{4} & 0 & 0 & 0 & 0 & 0 & 0 \\
\langle -\frac{1}{2},+\frac{3}{2}| & 0 & 0 & -\frac{3}{4} & 0 & 0 & 0 & 0 & 0 \\
\langle -\frac{1}{2},+\frac{1}{2}| & 0 & 0 & 0 & -\frac{1}{4} & 0 & 0 & 0 & 0 \\
\langle -\frac{1}{2},-\frac{1}{2}| & 0 & 0 & 0 & 0 & \frac{1}{4} & 0 & 0 & 0 \\
\langle -\frac{1}{2},-\frac{3}{2}| & 0 & 0 & 0 & 0 & 0 & \frac{3}{4} & 0 & 0 \\
\langle -\frac{1}{2},-\frac{5}{2}| & 0 & 0 & 0 & 0 & 0 & 0 & \frac{5}{4} & 0 \\
\langle -\frac{1}{2},-\frac{7}{2}| & 0 & 0 & 0 & 0 & 0 & 0 & 0 & \frac{7}{4}
\end{array}
= N^*
$$

$$
\begin{array}{c|cccccccc}
 & |-\frac{3}{2},+\frac{7}{2}\rangle & |-\frac{3}{2},+\frac{5}{2}\rangle & |-\frac{3}{2},+\frac{3}{2}\rangle & |-\frac{3}{2},+\frac{1}{2}\rangle & |-\frac{3}{2},-\frac{1}{2}\rangle & |-\frac{3}{2},-\frac{3}{2}\rangle & |-\frac{3}{2},-\frac{5}{2}\rangle & |-\frac{3}{2},-\frac{7}{2}\rangle \\
\hline
\langle -\frac{1}{2},+\frac{7}{2}| & 0 & 0 & 0 & 0 & 0 & 0 & 0 & 0 \\
\langle -\frac{1}{2},+\frac{5}{2}| & \frac{1}{2}\sqrt{105} & 0 & 0 & 0 & 0 & 0 & 0 & 0 \\
\langle -\frac{1}{2},+\frac{3}{2}| & 0 & 3\sqrt{5} & 0 & 0 & 0 & 0 & 0 & 0 \\
\langle -\frac{1}{2},+\frac{1}{2}| & 0 & 0 & \frac{15}{2} & 0 & 0 & 0 & 0 & 0 \\
\langle -\frac{1}{2},-\frac{1}{2}| & 0 & 0 & 0 & 2\sqrt{15} & 0 & 0 & 0 & 0 \\
\langle -\frac{1}{2},-\frac{3}{2}| & 0 & 0 & 0 & 0 & \frac{15}{2} & 0 & 0 & 0 \\
\langle -\frac{1}{2},-\frac{5}{2}| & 0 & 0 & 0 & 0 & 0 & 3\sqrt{5} & 0 & 0 \\
\langle -\frac{1}{2},-\frac{7}{2}| & 0 & 0 & 0 & 0 & 0 & 0 & \frac{1}{2}\sqrt{105} & 0
\end{array}
= O^*
$$

$$
\begin{array}{c|cccccccc}
 & |-\frac{1}{2},+\frac{7}{2}\rangle & |-\frac{1}{2},+\frac{5}{2}\rangle & |-\frac{1}{2},+\frac{3}{2}\rangle & |-\frac{1}{2},+\frac{1}{2}\rangle & |-\frac{1}{2},-\frac{1}{2}\rangle & |-\frac{1}{2},-\frac{3}{2}\rangle & |-\frac{1}{2},-\frac{5}{2}\rangle & |-\frac{1}{2},-\frac{7}{2}\rangle \\
\hline
\langle -\frac{3}{2},+\frac{7}{2}| & 0 & \frac{1}{2}\sqrt{105} & 0 & 0 & 0 & 0 & 0 & 0 \\
\langle -\frac{3}{2},+\frac{5}{2}| & 0 & 0 & 3\sqrt{5} & 0 & 0 & 0 & 0 & 0 \\
\langle -\frac{3}{2},+\frac{3}{2}| & 0 & 0 & 0 & \frac{15}{2} & 0 & 0 & 0 & 0 \\
\langle -\frac{3}{2},+\frac{1}{2}| & 0 & 0 & 0 & 0 & 2\sqrt{15} & 0 & 0 & 0 \\
\langle -\frac{3}{2},-\frac{1}{2}| & 0 & 0 & 0 & 0 & 0 & \frac{15}{2} & 0 & 0 \\
\langle -\frac{3}{2},-\frac{3}{2}| & 0 & 0 & 0 & 0 & 0 & 0 & 3\sqrt{5} & 0 \\
\langle -\frac{3}{2},-\frac{5}{2}| & 0 & 0 & 0 & 0 & 0 & 0 & 0 & \frac{1}{2}\sqrt{105} \\
\langle -\frac{3}{2},-\frac{7}{2}| & 0 & 0 & 0 & 0 & 0 & 0 & 0 & 0
\end{array}
= P^*
$$

$$
\begin{array}{c|cccccccc}
 & \left|-\frac{3}{2},+\frac{7}{2}\right\rangle & \left|-\frac{3}{2},+\frac{5}{2}\right\rangle & \left|-\frac{3}{2},+\frac{3}{2}\right\rangle & \left|-\frac{3}{2},+\frac{1}{2}\right\rangle & \left|-\frac{3}{2},-\frac{1}{2}\right\rangle & \left|-\frac{3}{2},-\frac{3}{2}\right\rangle & \left|-\frac{3}{2},-\frac{5}{2}\right\rangle & \left|-\frac{3}{2},-\frac{7}{2}\right\rangle \\
\left\langle-\frac{3}{2},+\frac{7}{2}\right| & -\frac{21}{4} & 0 & 0 & 0 & 0 & 0 & 0 & 0 \\
\left\langle-\frac{3}{2},+\frac{5}{2}\right| & 0 & -\frac{15}{4} & 0 & 0 & 0 & 0 & 0 & 0 \\
\left\langle-\frac{3}{2},+\frac{3}{2}\right| & 0 & 0 & -\frac{9}{4} & 0 & 0 & 0 & 0 & 0 \\
\left\langle-\frac{3}{2},+\frac{1}{2}\right| & 0 & 0 & 0 & -\frac{3}{4} & 0 & 0 & 0 & 0 \\
\left\langle-\frac{3}{2},-\frac{1}{2}\right| & 0 & 0 & 0 & 0 & \frac{3}{4} & 0 & 0 & 0 \\
\left\langle-\frac{3}{2},-\frac{3}{2}\right| & 0 & 0 & 0 & 0 & 0 & \frac{9}{4} & 0 & 0 \\
\left\langle-\frac{3}{2},-\frac{5}{2}\right| & 0 & 0 & 0 & 0 & 0 & 0 & \frac{15}{4} & 0 \\
\left\langle-\frac{3}{2},-\frac{7}{2}\right| & 0 & 0 & 0 & 0 & 0 & 0 & 0 & \frac{21}{4}
\end{array}
= Q^*
$$

$$
\begin{array}{c|cccccccc}
 & \left|-\frac{5}{2},+\frac{7}{2}\right\rangle & \left|-\frac{5}{2},+\frac{5}{2}\right\rangle & \left|-\frac{5}{2},+\frac{3}{2}\right\rangle & \left|-\frac{5}{2},+\frac{1}{2}\right\rangle & \left|-\frac{5}{2},-\frac{1}{2}\right\rangle & \left|-\frac{5}{2},-\frac{3}{2}\right\rangle & \left|-\frac{5}{2},-\frac{5}{2}\right\rangle & \left|-\frac{5}{2},-\frac{7}{2}\right\rangle \\
\left\langle-\frac{3}{2},+\frac{7}{2}\right| & 0 & 0 & 0 & 0 & 0 & 0 & 0 & 0 \\
\left\langle-\frac{3}{2},+\frac{5}{2}\right| & \sqrt{21} & 0 & 0 & 0 & 0 & 0 & 0 & 0 \\
\left\langle-\frac{3}{2},+\frac{3}{2}\right| & 0 & 6 & 0 & 0 & 0 & 0 & 0 & 0 \\
\left\langle-\frac{3}{2},+\frac{1}{2}\right| & 0 & 0 & 3\sqrt{5} & 0 & 0 & 0 & 0 & 0 \\
\left\langle-\frac{3}{2},-\frac{1}{2}\right| & 0 & 0 & 0 & 4\sqrt{3} & 0 & 0 & 0 & 0 \\
\left\langle-\frac{3}{2},-\frac{3}{2}\right| & 0 & 0 & 0 & 0 & 3\sqrt{5} & 0 & 0 & 0 \\
\left\langle-\frac{3}{2},-\frac{5}{2}\right| & 0 & 0 & 0 & 0 & 0 & 6 & 0 & 0 \\
\left\langle-\frac{3}{2},-\frac{7}{2}\right| & 0 & 0 & 0 & 0 & 0 & 0 & \sqrt{21} & 0
\end{array}
= R^*
$$

$$
\begin{array}{c|cccccccc}
 & \left|-\frac{3}{2},+\frac{7}{2}\right\rangle & \left|-\frac{3}{2},+\frac{5}{2}\right\rangle & \left|-\frac{3}{2},+\frac{3}{2}\right\rangle & \left|-\frac{3}{2},+\frac{1}{2}\right\rangle & \left|-\frac{3}{2},-\frac{1}{2}\right\rangle & \left|-\frac{3}{2},-\frac{3}{2}\right\rangle & \left|-\frac{3}{2},-\frac{5}{2}\right\rangle & \left|-\frac{3}{2},-\frac{7}{2}\right\rangle \\
\left\langle-\frac{5}{2},+\frac{7}{2}\right| & 0 & \sqrt{21} & 0 & 0 & 0 & 0 & 0 & 0 \\
\left\langle-\frac{5}{2},+\frac{5}{2}\right| & 0 & 0 & 6 & 0 & 0 & 0 & 0 & 0 \\
\left\langle-\frac{5}{2},+\frac{3}{2}\right| & 0 & 0 & 0 & 3\sqrt{5} & 0 & 0 & 0 & 0 \\
\left\langle-\frac{5}{2},+\frac{1}{2}\right| & 0 & 0 & 0 & 0 & 4\sqrt{3} & 0 & 0 & 0 \\
\left\langle-\frac{5}{2},-\frac{1}{2}\right| & 0 & 0 & 0 & 0 & 0 & 3\sqrt{5} & 0 & 0 \\
\left\langle-\frac{5}{2},-\frac{3}{2}\right| & 0 & 0 & 0 & 0 & 0 & 0 & 6 & 0 \\
\left\langle-\frac{5}{2},-\frac{5}{2}\right| & 0 & 0 & 0 & 0 & 0 & 0 & 0 & \sqrt{21} \\
\left\langle-\frac{5}{2},-\frac{7}{2}\right| & 0 & 0 & 0 & 0 & 0 & 0 & 0 & 0
\end{array}
= T^*
$$

$$
\begin{array}{c}
\\
\left\langle -\frac{5}{2},+\frac{7}{2}\right| \\
\left\langle -\frac{5}{2},+\frac{5}{2}\right| \\
\left\langle -\frac{5}{2},+\frac{3}{2}\right| \\
\left\langle -\frac{5}{2},+\frac{1}{2}\right| \\
\left\langle -\frac{5}{2},-\frac{1}{2}\right| \\
\left\langle -\frac{5}{2},-\frac{3}{2}\right| \\
\left\langle -\frac{5}{2},-\frac{5}{2}\right| \\
\left\langle -\frac{5}{2},-\frac{7}{2}\right|
\end{array}
\begin{array}{c}
\left|-\frac{5}{2},+\frac{7}{2}\right\rangle \quad \left|-\frac{5}{2},+\frac{5}{2}\right\rangle \quad \left|-\frac{5}{2},+\frac{3}{2}\right\rangle \quad \left|-\frac{5}{2},+\frac{1}{2}\right\rangle \quad \left|-\frac{5}{2},-\frac{1}{2}\right\rangle \quad \left|-\frac{5}{2},-\frac{3}{2}\right\rangle \quad \left|-\frac{5}{2},-\frac{5}{2}\right\rangle \quad \left|-\frac{5}{2},-\frac{7}{2}\right\rangle \\
\left[\begin{array}{cccccccc}
-\frac{35}{4} & 0 & 0 & 0 & 0 & 0 & 0 & 0 \\
0 & -\frac{25}{4} & 0 & 0 & 0 & 0 & 0 & 0 \\
0 & 0 & -\frac{15}{4} & 0 & 0 & 0 & 0 & 0 \\
0 & 0 & 0 & -\frac{5}{4} & 0 & 0 & 0 & 0 \\
0 & 0 & 0 & 0 & \frac{5}{4} & 0 & 0 & 0 \\
0 & 0 & 0 & 0 & 0 & \frac{15}{4} & 0 & 0 \\
0 & 0 & 0 & 0 & 0 & 0 & \frac{25}{4} & 0 \\
0 & 0 & 0 & 0 & 0 & 0 & 0 & \frac{35}{4}
\end{array}\right]
\end{array}
= U^*
$$

$$
\begin{array}{c}
\\
\left\langle -\frac{7}{2},+\frac{7}{2}\right| \\
\left\langle -\frac{7}{2},+\frac{5}{2}\right| \\
\left\langle -\frac{7}{2},+\frac{3}{2}\right| \\
\left\langle -\frac{7}{2},+\frac{1}{2}\right| \\
\left\langle -\frac{7}{2},-\frac{1}{2}\right| \\
\left\langle -\frac{7}{2},-\frac{3}{2}\right| \\
\left\langle -\frac{7}{2},-\frac{5}{2}\right| \\
\left\langle -\frac{7}{2},-\frac{7}{2}\right|
\end{array}
\begin{array}{c}
\left|-\frac{7}{2},+\frac{7}{2}\right\rangle \quad \left|-\frac{7}{2},+\frac{5}{2}\right\rangle \quad \left|-\frac{7}{2},+\frac{3}{2}\right\rangle \quad \left|-\frac{7}{2},+\frac{1}{2}\right\rangle \quad \left|-\frac{7}{2},-\frac{1}{2}\right\rangle \quad \left|-\frac{7}{2},-\frac{3}{2}\right\rangle \quad \left|-\frac{7}{2},-\frac{5}{2}\right\rangle \quad \left|-\frac{7}{2},-\frac{7}{2}\right\rangle \\
\left[\begin{array}{cccccccc}
0 & 0 & 0 & 0 & 0 & 0 & 0 & 0 \\
\frac{7}{2} & 0 & 0 & 0 & 0 & 0 & 0 & 0 \\
0 & \sqrt{21} & 0 & 0 & 0 & 0 & 0 & 0 \\
0 & 0 & \frac{1}{2}\sqrt{105} & 0 & 0 & 0 & 0 & 0 \\
0 & 0 & 0 & 2\sqrt{7} & 0 & 0 & 0 & 0 \\
0 & 0 & 0 & 0 & \frac{1}{2}\sqrt{105} & 0 & 0 & 0 \\
0 & 0 & 0 & 0 & 0 & \sqrt{21} & 0 & 0 \\
0 & 0 & 0 & 0 & 0 & 0 & \frac{7}{2} & 0
\end{array}\right]
\end{array}
= V^*
$$

$$
\begin{array}{c}
\\
\left\langle -\frac{7}{2},+\frac{7}{2}\right| \\
\left\langle -\frac{7}{2},+\frac{5}{2}\right| \\
\left\langle -\frac{7}{2},+\frac{3}{2}\right| \\
\left\langle -\frac{7}{2},+\frac{1}{2}\right| \\
\left\langle -\frac{7}{2},-\frac{1}{2}\right| \\
\left\langle -\frac{7}{2},-\frac{3}{2}\right| \\
\left\langle -\frac{7}{2},-\frac{5}{2}\right| \\
\left\langle -\frac{7}{2},-\frac{7}{2}\right|
\end{array}
\begin{array}{c}
\left|-\frac{5}{2},+\frac{7}{2}\right\rangle \quad \left|-\frac{5}{2},+\frac{5}{2}\right\rangle \quad \left|-\frac{5}{2},+\frac{3}{2}\right\rangle \quad \left|-\frac{5}{2},+\frac{1}{2}\right\rangle \quad \left|-\frac{5}{2},-\frac{1}{2}\right\rangle \quad \left|-\frac{5}{2},-\frac{3}{2}\right\rangle \quad \left|-\frac{5}{2},-\frac{5}{2}\right\rangle \quad \left|-\frac{5}{2},-\frac{7}{2}\right\rangle \\
\left[\begin{array}{cccccccc}
0 & \frac{7}{2} & 0 & 0 & 0 & 0 & 0 & 0 \\
0 & 0 & \sqrt{21} & 0 & 0 & 0 & 0 & 0 \\
0 & 0 & 0 & \frac{1}{2}\sqrt{105} & 0 & 0 & 0 & 0 \\
0 & 0 & 0 & 0 & 2\sqrt{7} & 0 & 0 & 0 \\
0 & 0 & 0 & 0 & 0 & \frac{1}{2}\sqrt{105} & 0 & 0 \\
0 & 0 & 0 & 0 & 0 & 0 & \sqrt{21} & 0 \\
0 & 0 & 0 & 0 & 0 & 0 & 0 & \frac{7}{2} \\
0 & 0 & 0 & 0 & 0 & 0 & 0 & 0
\end{array}\right]
\end{array}
= W^*
$$

$$
\begin{array}{c}
\\
\left\langle -\frac{7}{2},+\frac{7}{2}\right| \\
\left\langle -\frac{7}{2},+\frac{5}{2}\right| \\
\left\langle -\frac{7}{2},+\frac{3}{2}\right| \\
\left\langle -\frac{7}{2},+\frac{1}{2}\right| \\
\left\langle -\frac{7}{2},-\frac{1}{2}\right| \\
\left\langle -\frac{7}{2},-\frac{3}{2}\right| \\
\left\langle -\frac{7}{2},-\frac{5}{2}\right| \\
\left\langle -\frac{7}{2},-\frac{7}{2}\right|
\end{array}
\begin{array}{c}
\begin{array}{cccccccc}
\left|-\frac{7}{2},+\frac{7}{2}\right\rangle & \left|-\frac{7}{2},+\frac{5}{2}\right\rangle & \left|-\frac{7}{2},+\frac{3}{2}\right\rangle & \left|-\frac{7}{2},+\frac{1}{2}\right\rangle & \left|-\frac{7}{2},-\frac{1}{2}\right\rangle & \left|-\frac{7}{2},-\frac{3}{2}\right\rangle & \left|-\frac{7}{2},-\frac{5}{2}\right\rangle & \left|-\frac{7}{2},-\frac{7}{2}\right\rangle
\end{array} \\
\left[\begin{array}{cccccccc}
-\frac{49}{4} & 0 & 0 & 0 & 0 & 0 & 0 & 0 \\
0 & -\frac{35}{4} & 0 & 0 & 0 & 0 & 0 & 0 \\
0 & 0 & -\frac{21}{4} & 0 & 0 & 0 & 0 & 0 \\
0 & 0 & 0 & -\frac{7}{4} & 0 & 0 & 0 & 0 \\
0 & 0 & 0 & 0 & \frac{7}{4} & 0 & 0 & 0 \\
0 & 0 & 0 & 0 & 0 & \frac{21}{4} & 0 & 0 \\
0 & 0 & 0 & 0 & 0 & 0 & \frac{35}{4} & 0 \\
0 & 0 & 0 & 0 & 0 & 0 & 0 & \frac{49}{4}
\end{array}\right]
\end{array}
= X^*
$$

B Transition probability

The transition probabilities for a thin polycrystalline absorber are proportional to the square of the Clebsch-Gordan coefficient. The Clebsch-Gordon coefficients are given by Wigner [64] by the use of group-theoretical methods as the following expression:

$$\begin{aligned} &C(j_1 j_2 m_1 m_2 | j_1 j_2 j m) = \delta(m, m_1 + m_2) \\ &\times \sqrt{(2j+1)\frac{(j+j_1-j_2)!(j-j_1+j_2)!(j_1+j_2-j)!(j+m)!(j-m)!}{(j_1+j_2+j+1)!(j_1-m_1)!(j_1+m_1)!(j_2-m_2)!}(j_2+m_2)!} \\ &\times \sum \frac{(-1)^{\kappa+j_2+m_2}(j_2+j+m_1-\kappa)!(j_1-m_1+\kappa)!}{\kappa!(j-j_1+j_2-\kappa)!(j+m-\kappa)!(\kappa+j_1-j_2-m)!} \end{aligned} \tag{B.1}$$

where j_1 is I_{gr}, m_1 is $m_{I_{gr}}$, j_2 is I_γ, the spin of the γ-quantum, which is equal to 1 and m_2 is Δm, given by the selection rule for the transitions, which is equal to 0, ± 1. j is I_{ex} and m is $m_{I_{ex}}$. In our case I_{gr} is 5/2 and I_{ex} is 7/2, with this $m_{I_{gr}}$ goes from -5/2 to +5/2 and $m_{I_{ex}}$ from -7/2 to +7/2.

In this summation the index κ takes on all integral values such that none of the factorial arguments are negative. The index κ for m = j and m = -j is especially simple; in the first case only the therm κ = 0 occurs, and in the second, only κ = j+ $j_1 + j_2$. In the following table B.1 all possible values for κ are given.

$m_{I_{ex}}$	κ
7/2	7
5/2	0, 1, 2, 3, 4, 5, 6
3/2	0, 1, 2, 3, 4, 5
1/2	0, 1, 2, 3, 4
-1/2	0, 1, 2, 3
-3/2	0, 1, 2
-5/2	0, 1
-7/2	0

Table B.1: Possible values of κ.

Those values of κ leading to a negative factorial arguments are meaningless. Table B.2 shows the values of κ for each transitions with only positive factorial arguments.

	$m_{I_{gr}}$					
m_{I_e}	5/2	3/2	1/2	-1/2	-3/2	-5/2
7/2	-					
5/2	1, 2	1, 2				
3/2	0, 1, 2	0, 1, 2	0, 1, 2			
1/2		0, 1, 2	0, 1, 2	0, 1, 2		
-1/2			0, 1, 2	0, 1, 2	0, 1, 2 $\sqrt{7}$	
-3/2				0, 1, 2	0, 1, 2	0, 1, 2
-5/2					0, 1	0, 1
-7/2						0

Table B.2: Values of κ for each transition

For a better understanding an example of calculating the Clebsch-Gordan coefficient will be given. For the transition from $m_{I_{gr}}$ = 5/2 to $m_{I_{ex}}$=5/2, with Δm=0, I_{gr}=5/2, I_{ex}=7/2, and I_γ=1 it follows for the first part of formula B.1:

$$\begin{aligned}
&\sqrt{(2j+1)\frac{(j+j_1-j_2)!(j-j_1+j_2)!(j_1+j_2-j)!(j+m)!(j-m)!}{(j_1+j_2+j+1)!(j_1-m_1)!(j_1+m_1)!(j_2-m_2)!}(j_2+m_2)!} \\
&= \sqrt{(2\frac{7}{2}+1)\frac{(\frac{7}{2}+\frac{5}{2}-1)!(\frac{7}{2}-\frac{5}{2}+1)!(\frac{5}{2}+1-\frac{7}{2})!(\frac{7}{2}+\frac{5}{2})!(\frac{7}{2}-\frac{5}{2})!}{(\frac{5}{2}+1+\frac{7}{2}+1)!(\frac{5}{2}-\frac{5}{2})!(\frac{5}{2}+\frac{5}{2})!(1-0)!}(1+0)!} \\
&= \frac{1}{7}\sqrt{14}
\end{aligned}$$

In this case κ takes on all integral values from 0 to 6. With this it follows:

For $\kappa = 0$:

$$\begin{aligned}
&\frac{(-1)^{0+1+0}(1+7/2+5/2-0)!(5/2-5/2+0)!}{0!(7/2-5/2+1-0)!(7/2+5/2-0)!(0+5/2-1-5/2)!} \\
&= (-1)\,\frac{7!\;0!}{0!\;2!\;6!\;(-1)!}
\end{aligned}$$

Since there is (-1)! in the equation this is κ meaningless.

For $\kappa = 1$ and $\kappa = 2$, all factorial arguments are positive.

$$\kappa = 1$$
$$\frac{(-1)^{1+1+0}(1+7/2+5/2-1)!(5/2-5/2+1)!}{1!(7/2-5/2+1-1)!(7/2+5/2-1)!(1+5/2-1-5/2)!}$$
$$= 1\,\frac{6!\;1!}{1!\;1!\;5!\;0!}$$
$$= 6$$

$$\kappa = 2$$
$$\frac{(-1)^{2+1+0}(1+7/2+5/2-2)!(5/2-5/2+2)!}{2!(7/2-5/2+1-2)!(7/2+5/2-2)!(2+5/2-1-5/2)!}$$
$$(-1)\,\frac{5!\;2!}{2!\;0!\;4!\;1!}$$
$$= -5$$

The equations of κ =3, 4, 5 and 6 have negative factorial arguments and therefore they are meaningless.

$$\kappa = 3$$
$$\frac{(-1)^{3+1+0}(1+7/2+5/2-3)!(5/2-5/2+3)!}{3!(7/2-5/2+1-3)!(7/2+5/2-3)!(3+5/2-1-5/2)!}$$
$$= 1\,\frac{4!\;3!}{3!\;(-1)!\;3!2!}$$

$$\kappa = 4$$
$$\frac{(-1)^{4+1+0}(1+7/2+5/2-4)!(5/2-5/2+4)!}{4!(7/2-5/2+1-4)!(7/2+5/2-4)!(4+5/2-1-5/2)!}$$
$$= -1\frac{3!\;4!}{4!\;(-2)!\;2!\;3!}$$

$$\kappa = 5$$
$$\frac{(-1)^{5+1+0}(1+7/2+5/2-5)!(5/2-5/2+5)!}{5!(7/2-5/2+1-5)!(7/2+5/2-5)!(5+5/2-1-5/2)!}$$
$$= 1\,\frac{2!\;5!}{5!\;(-3)!\;1!\;4!}$$

$$\kappa = 6$$
$$\frac{(-1)^{6+1+0}(1+7/2+5/2-6)!(5/2-5/2+6)!}{6!(7/2-5/2+1-6)!(7/2+5/2-6)!(6+5/2-1-5/2)!}$$
$$= -1\frac{1!\;6!}{6!\;(-4)!\;0!\;5!}$$

With this it follows:

$$\begin{aligned} & C(5/2\,1\,5/2\,0|5/2\,1\,7/2\,5/2) \\ &= \delta(\frac{5}{2}, \frac{5}{2}+0)\ \frac{1}{7}\ \sqrt{14}\ (6-5) \\ &= \frac{1}{7}\sqrt{14} \end{aligned}$$

All Clebsch-Gordon coefficients are given in table B.3.

	m_{I_g}					
m_{I_e}	5/2	3/2	1/2	-1/2	-3/2	-5/2
7/2	1					
5/2	$1/7\ \sqrt{14}$	$1/7\ \sqrt{35}$				
3/2	$1/21\ \sqrt{21}$	$1/21\ \sqrt{210}$	$1/21\ \sqrt{210}$			
1/2		$1/7\ \sqrt{7}$	$2/7\ \sqrt{7}$	$1/7\ \sqrt{14}$		
-1/2			$1/7\ \sqrt{14}$	$2/7\ \sqrt{7}$	$1/7\ \sqrt{7}$	
-3/2				$1/21\ \sqrt{210}$	$1/21\ \sqrt{210}$	$1/21\ \sqrt{21}$
-5/2					$1/7\ \sqrt{35}$	$1/7\ \sqrt{14}$
-7/2						1

Table B.3: Clebsch-Gordon coefficients for all transitions

For the transition probability all coefficients have to be squared. The transition probabilities are give in table B.4.

	m_{I_g}					
m_{I_e}	5/2	3/2	1/2	-1/2	-3/2	-5/2
7/2	1					
5/2	2/7	5/7				
3/2	1/21	10/21	10/21			
1/2		1/7	4/7	2/7		
-1/2			2/7	4/7	1/7	
-3/2				10/21	10/21	1/21
-5/2					5/7	2/7
-7/2						1

Table B.4: Transition probability (square of the Clebsch-Gordon coefficients) for all transitions

These values agree with those given in [51]. If multiplied by $55.55 \cdot 10^{-3}$ we get exactly the same values (see Table B.5).

	m_{I_g}					
m_{I_e}	5/2	3/2	1/2	-1/2	-3/2	-5/2
7/2	55.55	0	0	0	0	0
5/2	15.87	39.68	0	0	0	0
3/2	2.65	26.45	26.45	0	0	
1/2	0	7.94	31.74	15.87	0	0
-1/2	0	0	15.87	31.74	7.94	0
-3/2	0	0	0	26.45	26.45	2.65
-5/2	0	0	0	0	39.68	15.87
-7/2	0	0	0	0	0	55.55

Table B.5: Transition probabilities for ^{151}Eu (10^{-3})in the presence of a magnetic field taken from [51]

C Maple programm

In the following section the Maple© program used for the simulation of the Mössbauer spectra will be described.

f is the factor to convert 10^{-4} cm^{-1} into mm/s and w is the linewidth of each transition.

```
> restart:
  with(linalg):
  with(plots):
  f:=57.4*3*10^(-3):
  w:=4:
Warning, the protected names norm and trace have been redefined and unprotected

Warning, the name changecoords has been redefined
```

Matrix A contains the energy levels of the ground state. The first six values are for $m_S = -7/2$ and m_I from -5/2 to 5/2. The next six ones are for $m_S = -7/2$ and m_I from -5/2 to -7/2 and so an. Matrix B is the equivalent for the excited state. Here m_I goes from -7/2 to 7/2. Therefore, eight values belong to one m_S.

```
> A:=matrix(8,6,[
  -1015.769,-1015.769,-1014.049,-1014.048,-1014.048,-823.937,
   -810.169,-810.169,-810.169,-798.633,-798.633,-798.633,
   -245.261,-245.261,-240.468,-240.468,-240.468,-230.138,
   -225.266,-225.266,-225.266,-204.983,-87.057,-87.057,
   -87.057, -29.852,-29.852,-29.852,12.906,12.906,
   56.209,56.209,56.209,94.834,94.834,94.834,
   950.178,953.182,953.182,953.182,955.581,955.581,
   955.581,1248.124,1248.124,1248.648,1248.648,1248.648]);

  B:=matrix(8,8,[
   -955.184,-955.184,-955.184,-954.287,-954.287,-954.287,-953.122,
   -801.596,-801.596,-801.596,-796.770,-796.770,-795.067,-795.067,
   -795.067,-792.718,-206.615,-206.615,-206.615,-204.685,-204.685,
   -204.685,-200.581,-200.581,-197.586,-197.586,-197.586,-181.085,
   -181.085,-181.085, -80.946,-80.946,-76.626,-76.626,-76.626,
   -52.567,-25.487,-25.487,-25.487,-9.144,-9.144,-9.144,11.003,
   33.309,33.309,33.309,36.071,36.071,968.140,968.140,968.140,
   969.035,969.035,969.334,969.334,969.334,969.753,1181.806,
   1181.806,1181.807,1182.022,1182.022,1182.022,1182.290]);


                [-1015.769  -1015.769 -1014.049  -1014.048  -1014.048  -823.937 ]
                [ -810.169   -810.169  -810.169   -798.633   -798.633  -798.633 ]
                [ -245.261   -245.261  -240.468   -240.468   -240.468  -230.138 ]
           A:=  [ -225.266   -225.266  -225.266   -204.983    -87.057   -87.057 ]
                [  -87.057    -29.852   -29.852    -29.852     12.906    12.906 ]
                [   56.209     56.209    56.209     94.834     94.834    94.834 ]
                [  950.178    953.182   953.182    953.182    955.581   955.581 ]
                [  955.581   1248.124  1248.124   1248.648   1248.648  1248.648 ]


                [ -955.184 -955.184 -955.184 -954.287 -954.287 -954.287 -953.122 -801.596]
                [ -801.596  -801.596 -796.770 -796.770 -795.067 -795.067 -795.067 -792.718]
                [ -206.615 -206.615 -206.615 -204.685 -204.685 -204.685 -200.581 -200.581]
           B:=  [ -197.586 -197.586 -197.586 -181.085 -181.085 -181.085  -80.946  -80.946]
                [  -76.626  -76.626  -76.626  -52.567  -25.487  -25.487  -25.487   -9.144]
                [   -9.144   -9.144   11.003   33.309   33.309   33.309   36.07    36.071]
                [  968.140  968.140  968.140  969.035  969.035  969.334  969.334  969.334]
                [  969.753 1181.806 1181.806 1181.807  182.022 1182.022 1182.022 1182.290]
```

First the matrix elements of the ground an excited state are multiplied by f to get the unit mm/s. The transition energies are the differences between these energies, taking the dipole selection rules into account. Then the eighteen possible transitions energies for each m_S are calculated. The number of each transition is consistent with those shown in Figure C.1. Each Mössbauer transitions has the Lorentzian line shape:

$$y = y_0 + \frac{2 \cdot A}{\pi} \cdot \frac{w}{4(x - x_0)^2 + w^2} \tag{C.1}$$

where y_0 is the baseline offset, A is the total area under the curve from the baseline, x_0 is the center of the peak and w is the full width of the peak at half height.

Each transition is put into a Lorentzian formula and weighted by the transition probabilities. The transition probabilities are given in Tabell B.5 in Appendix B. At least the 18 transitions are added. The steps of the loop are operated for each m_S from -7/2 to 7/2. The number of each transition is conform with those shown in Figure C.1.

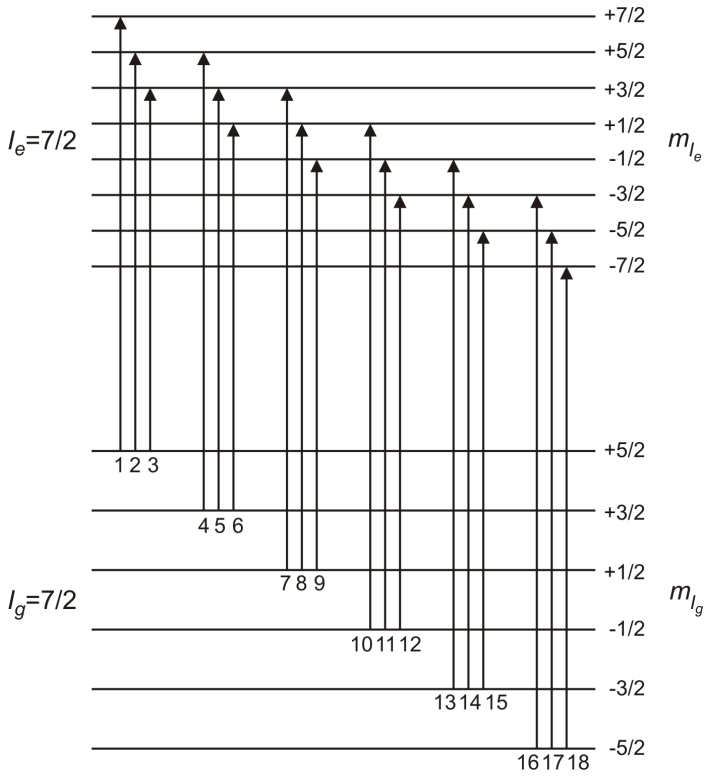

Figure C.1: Nuclear energy levels for ^{151}Eu in presence of a magnetic hyperfine interaction. The arrows denote the allowed 18 transitions.

With this results eight sums (one for each m_S) can be calculated. In the following the sums are plotted.

```
> for ms from 1 to 8 do
  ae1[ms]:=B[ms,1]*f:
  ae2[ms]:=B[ms,2]*f:
  ae3[ms]:=B[ms,3]*f:
  ae4[ms]:=B[ms,4]*f:
  ae5[ms]:=B[ms,5]*f:
  ae6[ms]:=B[ms,6]*f:
  ae7[ms]:=B[ms,7]*f:
  ae8[ms]:=B[ms,8]*f:
  ag1[ms]:=A[ms,1]*f:
  ag2[ms]:=A[ms,2]*f:
  ag3[ms]:=A[ms,3]*f:
  ag4[ms]:=A[ms,4]*f:
  ag5[ms]:=A[ms,5]*f:
  ag6[ms]:=A[ms,6]*f:

  a1[ms] :=ae1[ms]-ag1[ms]: # Transition 1
  a2[ms] :=ae2[ms]-ag1[ms]: # Transition 2
  a3[ms] :=ae3[ms]-ag1[ms]: # Transition 3
  a4[ms] :=ae2[ms]-ag2[ms]: # Transition 4
  a5[ms] :=ae3[ms]-ag2[ms]: # Transition 5
  a6[ms] :=ae4[ms]-ag2[ms]: # Transition 6
  a7[ms] :=ae3[ms]-ag3[ms]: # Transition 7
  a8[ms] :=ae4[ms]-ag3[ms]: # Transition 8
  a9[ms] :=ae5[ms]-ag3[ms]: # Transition 9
  a10[ms]:=ae4[ms]-ag4[ms]: # Transition 10
  a11[ms]:=ae5[ms]-ag4[ms]: # Transition 11
  a12[ms]:=ae6[ms]-ag4[ms]: # Transition 12
  a13[ms]:=ae5[ms]-ag5[ms]: # Transition 13
  a14[ms]:=ae6[ms]-ag5[ms]: # Transition 14
  a15[ms]:=ae7[ms]-ag5[ms]: # Transition 15
  a16[ms]:=ae6[ms]-ag6[ms]: # Transition 16
  a17[ms]:=ae7[ms]-ag6[ms]: # Transition 17
  a18[ms]:=ae8[ms]-ag6[ms]: # Transition 18

  y1[ms] :=55.55*w/(4*(x-a1[ms])^2+w^2):
  y2[ms] :=15.87*w/(4*(x-a2[ms])^2+w^2):
  y3[ms] :=2.65*w/(4*(x-a3[ms])^2+w^2):
  y4[ms] :=39.68*w/(4*(x-a4[ms])^2+w^2):
  y5[ms] :=26.45*w/(4*(x-a5[ms])^2+w^2):
  y6[ms] :=7.94*w/(4*(x-a6[ms])^2+w^2):
  y7[ms] :=26.45*w/(4*(x-a7[ms])^2+w^2):
  y8[ms] :=31.74*w/(4*(x-a8[ms])^2+w^2):
  y9[ms] :=15.87*w/(4*(x-a9[ms])^2+w^2):
  y10[ms]:=15.87*w/(4*(x-a10[ms])^2+w^2):
  y11[ms]:=31.74*w/(4*(x-a11[ms])^2+w^2):
  y12[ms]:=26.45*w/(4*(x-a12[ms])^2+w^2):
  y13[ms]:=7.94*w/(4*(x-a13[ms])^2+w^2):
  y14[ms]:=26.45*w/(4*(x-a14[ms])^2+w^2):
  y15[ms]:=39.68*w/(4*(x-a15[ms])^2+w^2):
  y16[ms]:=2.65*w/(4*(x-a16[ms])^2+w^2):
  y17[ms]:=15.87*w/(4*(x-a17[ms])^2+w^2):
  y18[ms]:=55.55*w/(4*(x-a18[ms])^2+w^2):

  y_sum[ms]:=y1[ms]+y2[ms]+y3[ms]+y4[ms]+y5[ms]+y6[ms]+y7[ms]
            +y8[ms]+y9[ms]+y10[ms]+y11[ms]+y12[ms]+y13[ms]
            +y14[ms]+y15[ms]+y16[ms]+y17[ms]+y18[ms]:
  end do:
```

Spectrum of $m_S = -7/2$ (top) and $m_S = -5/2$ (bottom).

```
> plot(-y_sum[1],x=-30..30);
```

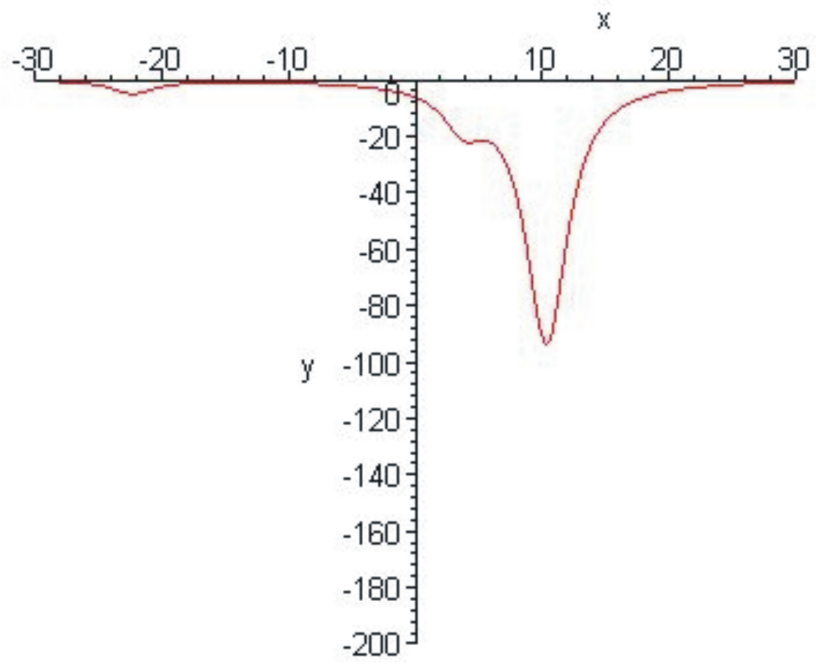


```
> plot(-y_sum[2],x=-30..30);
```

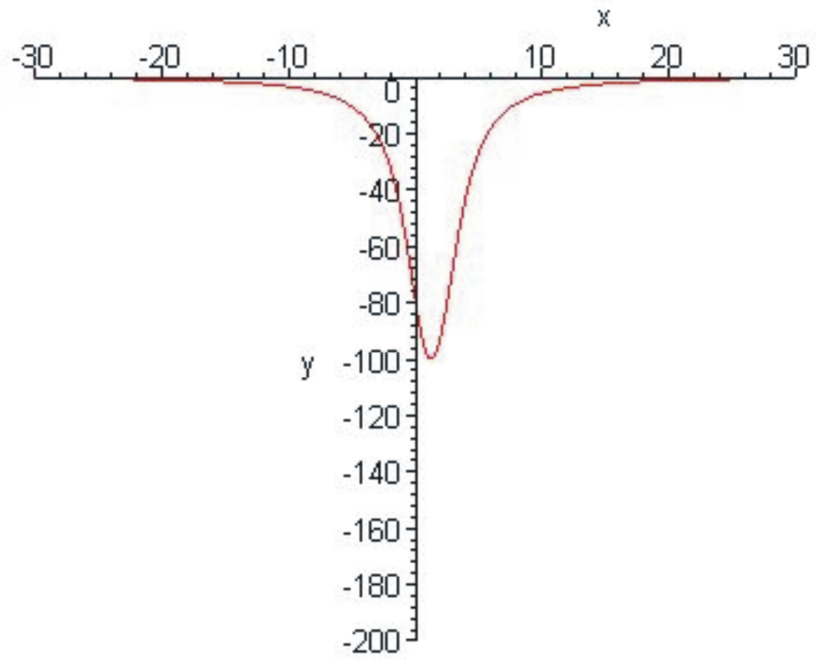

Spectra of $m_S = -3/2$ (top) and $m_S = -1/2$ (bottom).

```
> plot(-y_sum[3],x=-30..30);
```

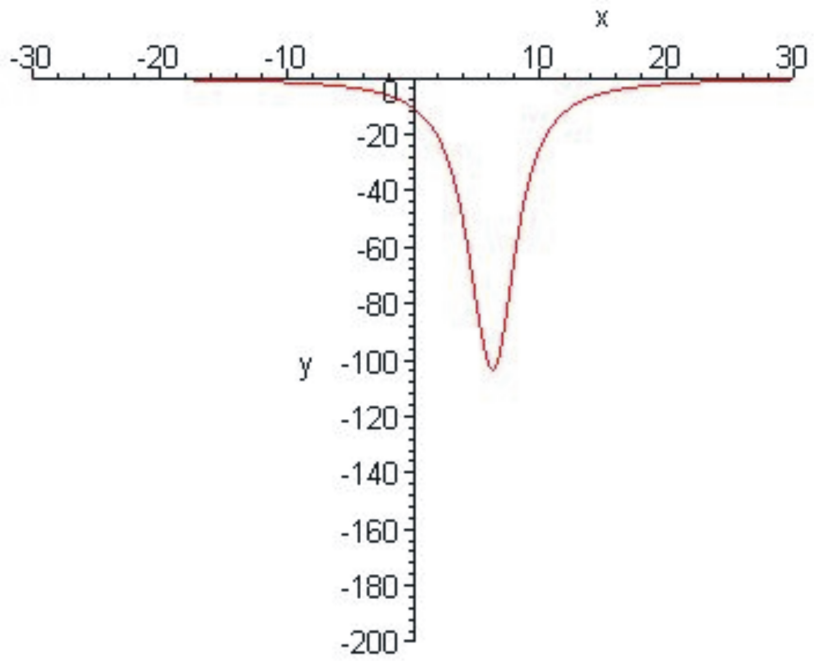


```
> plot(-y_sum[4],x=-30..30);
```

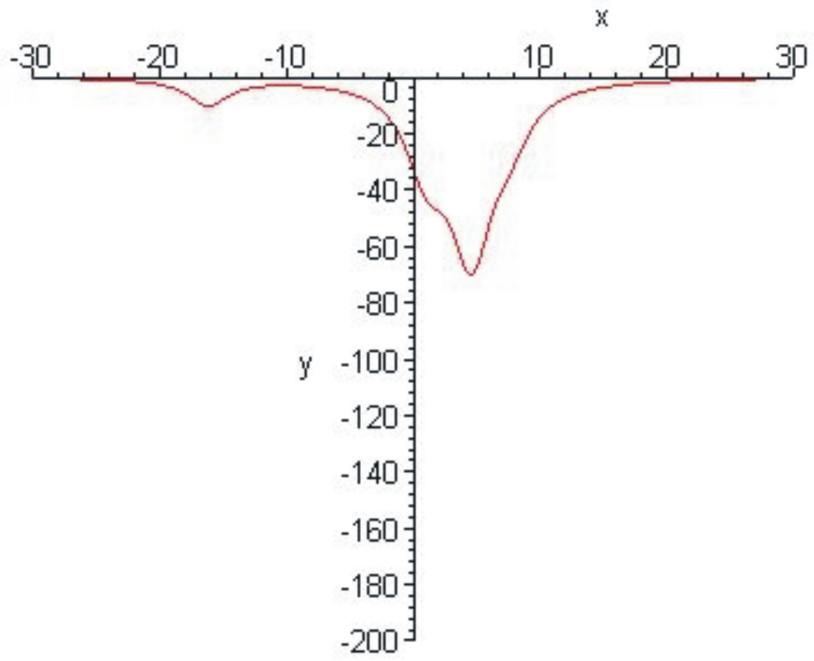

Spectra of m_S =1/2 (top) and m_S =3/2 (bottom).

```
> plot(-y_sum[5],x=-30..30);
```

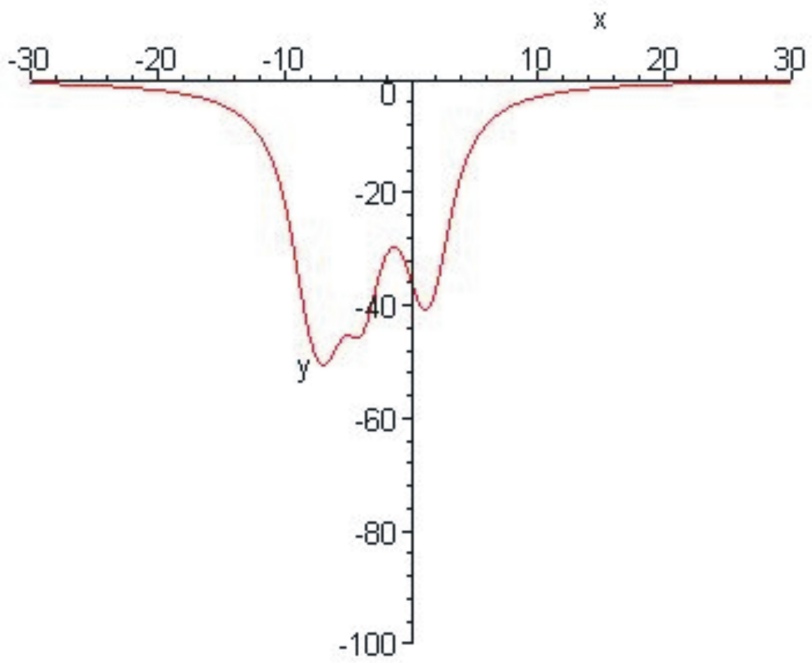


```
> plot(-y_sum[6],x=-30..30);
```

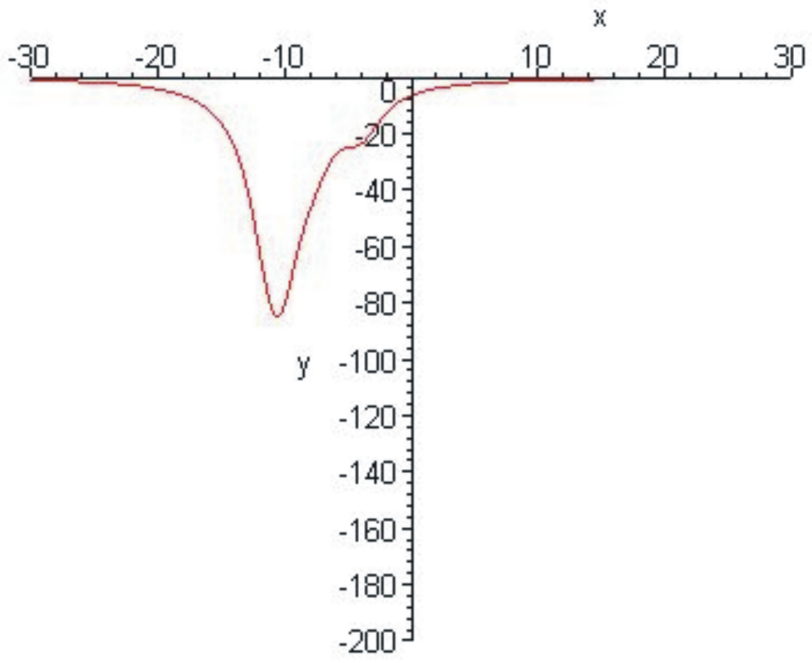

Spectra of m_S =5/2 (top) and m_S =7/2 (bottom).

```
> plot(-y_sum[7],x=-30..30);
```

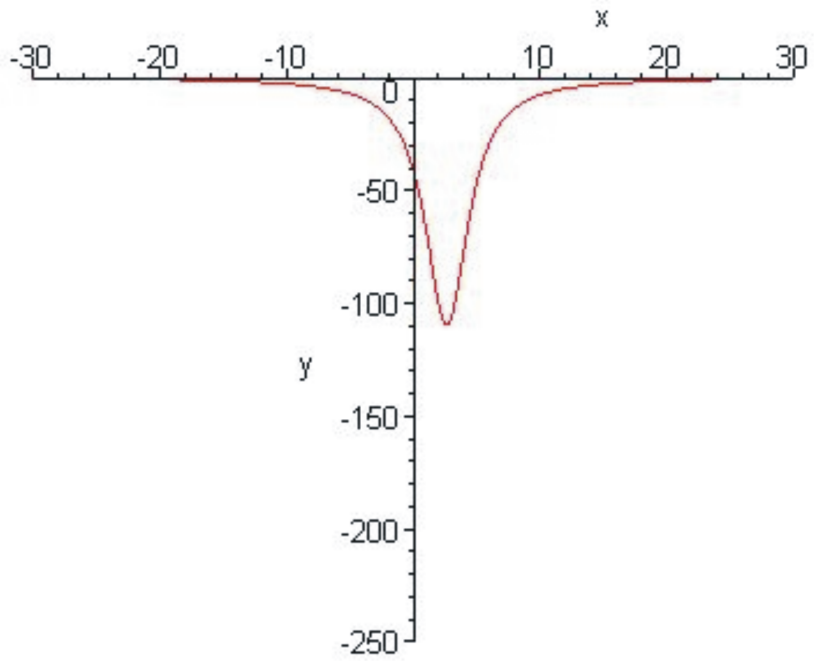


```
> plot(-y_sum[8],x=-30..30);
```

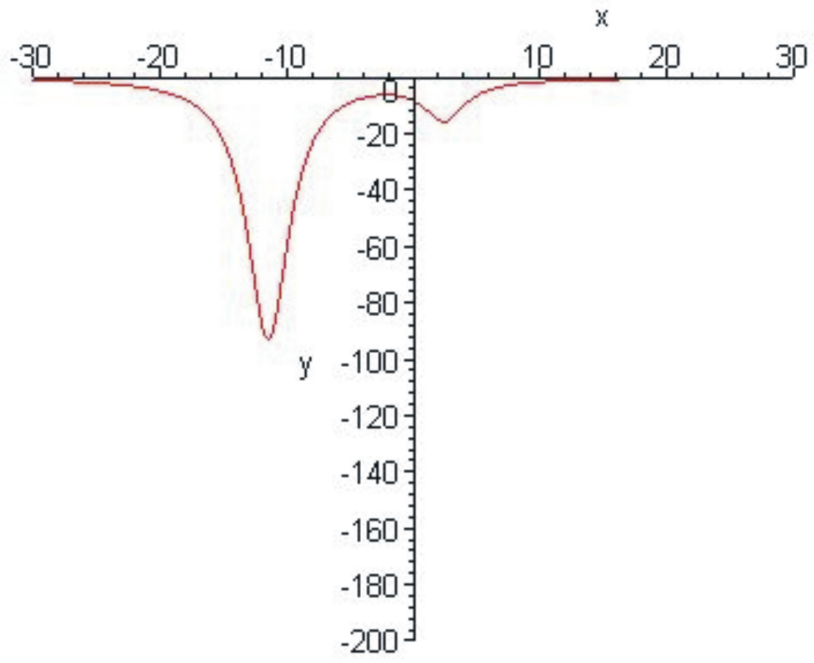

To get the total spectrum the spectra of all m_S from -7/2 to 7/2 are added and plotted.

```
> y_sum:=y_sum[1]+y_sum[2]+y_sum[3]+y_sum[4]+y_sum[5]+y_sum[6]
        +y_sum[7]+y_sum[8]:

  plot(-y_sum,x=-30..30);
```

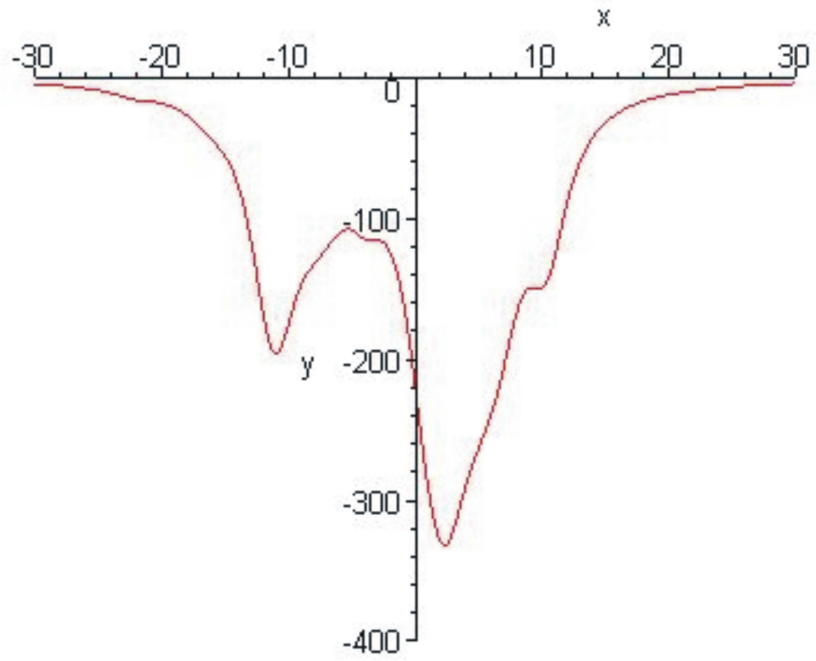

To get the right resulting spectrum the spectrum of each m_S has to be weighted with its Boltzmann factor.

Bibliography

[1] G. Chen, J. Johnson, S. Schweizer, J. Woodford, P. Newman, and D. MacFarlane. *Proceedings of SPIE, Medical Imaging 2006: Physics of Medical Imaging,* **6142**, 61422X–1 (2006).

[2] J. A. Johnson, S. Schweizer, B. Henke, G. Chen, J. Woodford, P. J. Newman, and D. R. MacFarlane. *J. Appl. Phys.* **100**, 034701 (2006).

[3] M. Secu, S. Schweizer, U. Rogulis, J.-M. Spaeth, A. Edgar, and G. V. M. Williams. *Radiation Measurements* **38**, 739–742 (2004).

[4] J. Selling, S. Schweizer, Spaeth J.-M., G. Corradi, Edgar A., and G. V. M. Williams. *phys. stat. sol (c)* **2**(1), 592 (2005).

[5] E. V. D. van Loef, P. Dorenbos, C. W. E. van Eijk, K. Krämer, and H. U. Güdel. *Appl. Phys. Lett.* **77**(10), 1467–1468 (2000).

[6] E. V. D. van Loef, P. Dorenbos, C. W. E. van Eijk, K. Krämer, and H. U. Güdel. *Appl. Phys. Lett.* **73**(10), 1573–1575 (2001).

[7] H. Wever and H. W. den Hartog. *Phys. Status Solidi B* **70**, 253–262 (1975).

[8] S. Schweizer, G. Corradi, A. Edgar, and J.-M. Spaeth. *J. Phys.: Condens. Matter* **13**, 2331–2338 (2001).

[9] J. Selling. Master's thesis, Uni Paderborn, (2004).

[10] L.M. Bollinger and G. E. Thomas. *The Review of Scienctific Instruments* **32**, 1044–1055 (1961).

[11] W. W. Moses. *Nuclear Instruments and Methods in Physics Research A* **336**, 253–261 (1993).

[12] M. Bertolaccini, S. Cova, and C. Bussolati. *Proc. Nucl. Electr. Symp., Versailles, France* **0**, 0 (1968).

[13] J. T. M. de Haas, P. Dorenbos, and C. W. E. van Eijk. *Nucl. Instrum. Methods Phys. Res., Sect. A* **537**, 97–100 (2005).

[14] A. Abragam and B. Bleany. *Electron Paramagnetic Resonance of Transition Ions*. Dover Publications, New York, (1986).

[15] J. A. Weil, J. R. Bolton, and J. E. Wertz. *Electron Paramagnetic Resonance: Elementary Theory and Practice Application*. Wiley-Interscience Publication, (1994).

[16] V. G. Grachev. *JETP* **92**, 1834–1844 (1987).

[17] V. G. Grachev. *Radiospectroscopy of Solid State* , 16–66 (1993).

[18] J.-M. Spaeth and R. H. Niklas, J. R.and Bartram. *Structural analysis of point defects in solids: an introduction to multiple magnetic resonance spectroscopy* . Springer-Verlag, (1992).

[19] T. E. Cranshaw, B. W. Dale, G. O. Longworth, and C. E. Johnson. *Mössbauer spectroscopy and its application*. Cambridge University Press, (1985).

[20] D. P. E. Dickson, F. J. Berry, E. R. Bauminger, S. Dappagupta, C. E. Johnson, G. J. Long, I. Nowik, R. V. Parish, and M. F. Thomas. *Mössbauer spectroscopy*. Cambridge University Press, (1986).

[21] E. R. Bauminger, G. M. Kalvius, and I. Nowik. *Mössbauer Isomer Shifts*. North-Holland, (1978).

[22] M. Moszynski, M. Kapusta, J. Zalipska, M. Balcerzyk, D. Wolski, M. Szawlowsk, and W. Klamra. *IEEE Trans. Nucl. Sci.* **46**, 880 (1999).

[23] D. R. Kinloch, W. Novak, P. Raby, and I. Toepke. *IEEE Trans. Nucl. Sci.* **41**, 752 (1994).

[24] C. L. Melcher. *Nucl. Instrum. Methods Phys. Res., Sect. A* **537**, 6 (2005).

[25] I. Holl, E. Lorentz, and G. Margeras. *IEEE Trans. Nucl. Sci.* **35**, 105 (1998).

[26] M. Moszynski, J. Gresset, C.and Vacher, and R. Odru. *Nucl. Instr. Meth.* **188**, 403 (1981).

[27] O. H. Nestor and C. Y. Huang. *IEEE Trans. Nucl. Sci.* **NS-22**, 68 (1975).

[28] E. B. Brackett, T. E. Brackett, and R. L. Sass. *J. Phys. Chem.* **67**(10), 2132 (1963).

[29] J. d d´Ans and E. Lax. *Taschenbuch für Chemiker und Physiker*. Springer-Verlag, (1967).

[30] C. W. E. van Eijk. In *Proc. Int. Conf. on Scintillators and their Applications, SCINT 97, Shanghai Branch Press, Shanghai, China*, 3–12, (1997).

[31] E. Monberg and Y. Ebisuzaki. *J. Cryst. Growth* **21**, 307–309 (1974).

[32] M. Secu, R. Kalchgruber, S. Schweizer, J.-M. Spaeth, and A. Edgar. *Radiation Effects & Defects in Solids* **157**, 957–962 (2002).

[33] T. Kobayasi, S. Mroczkowski, J. F. Owen, and L. H. Brixner. *Journal of Luminescence* **21**(3), 247–257 (1980).

[34] J. Selling, G. Corradi, M. Secu, and S. Schweizer. *Proceedings of the Eighth International Conference on Inorganic Scintillators and their Use in Scientific and Industrial Applications, Alushta, Crimea, Ukraine, September 19-23, 2005, ed. by A. Gektin and B. Grinyov (National Academy of Sciences of Ukraine, Ukraine - Kharkov, 2006)* **1**, 415–418 (2005).

[35] J. Selling, G. Corradi, M. Secu, and S. Schweizer. *J. Phys.: Condens. Matter* **17**, 8069 (2005).

[36] G. Corradi, M. Secu, S. Schweizer, and J.-M. J.-M. Spaeth. *Journal of Physics: Condensed Matter* **16**, 1489–1500 (2004).

[37] P. Dorenbos, J. T. M. de Haas, and C. W. E van Eijk. *IEEE Transactions on Nuclear Science* **42**, 2190–2202 (1995).

[38] M. Secu, S. Schweizer, U. Rogulis, and J.-M. Spaeth. *J. Phys.: Condens. Matter* **15**, 2061 (2003).

[39] W.-M. Li and M. Leskelä. *Mater. Lett.* **28**, 491 (1996).

[40] D. K. Williams, H. Yuan, and B. M Tissue. *Journal of Luminescence* **83-84**, 297–300 (1999).

[41] D. K. Williams, B. Bihari, B. M. Tissue, and J. M. McHale. *J. Phys. Chem. B* **102**, 916–920 (1998).

[42] A. van Dijken, J. Makkinje, and A. Meijerink. *Journal of Luminescence* **92**, 323 (2001).

[43] B. Mercier, C. Dujardin, G. Ledoux, C. Louis, O. Tillement, and P. Perriat. *Jouranl of Applied Physics* **96**, 650–653 (2004).

[44] K. Kojima, A. Kubo, M. Yamashita, N. Wada, T. Tsuneoka, and Y. Komatsubara. *J. Lumin.* **87-89**, 697 (2000).

[45] G. Blasse and B. C. Grabmaier. *Luminescent Materials*. Springer Verlag, Berlin Heidelberg, (1994).

[46] H. V. Lauer Jr. and F. K. Fong. *The Journal of Chemical Physics* **65**(8), 3108 October (1976).

[47] G. G. P. van Gorkom. *Journal of Physics and Chemistry of Solids* **31**(5), 905–912 (1970).

[48] K. W. H. Stevens. *Proceedings of the Physical Society* **65**, 209 (1952).

[49] R. L. Sass, E. B. Brackett, and T. E. Brackett. *J. Phys. Chem.* **67**, 2863–2864 (1963).

[50] J. L. Merz and P.S. Pershan. *Physical Review* **162**, 217 (1967).

[51] Gary J. Long and Fernande Grandjean. *Mössbauer Spectroscopy Applied to Inorganic Chemistry*, volume 3. Plenum Press, New York and London, (1987).

[52] J. M. Baker, B. Bleany, and W. Hayes. *Proceedings of the Royal Society of London. Series A, Mathematical and Physical Sciences* **247**, 141–151 (1958).

[53] J. M. Baker and F. I. B. Williams. *Proc. R. Soc. A* **267**(1329), 283–294 (1962).

[54] H. Maletta, W. Heidrich, and R. L. Mössbauer. *Phys. Lett. A.* **25**(4), 295 (1967).

[55] H. W. Wickman, M. Robbins, E. Buehler, and E. Catalano. *Phys. Lett. A* **31**(2), 59 (1970).

[56] N. Nitsche, J. Pelzl, S. Hufner, and P. Steiner. *Solid State Commun.* **10**(1), 145 (1972).

[57] R. L. Lambe and D. Schroeer. *Phys. Rev. Lett.* **36**(1), 45 (1976).

[58] D. Schroeer, Ch. S. Kuo, and R. L. Lambe. *phys. stat. sol. (b)* **92**, 565–572 (1979).

[59] T. J. Menne. *Physical Review* **180**, 350 (1969).

[60] F. J. Litterst, H. Michlitz, and A. Schichl. *Physics Letters* **57A**, 70 (1976).

[61] G. J. Long, T. E. Cranshaw, and G Longworth. *Mössbauer Effect Reference and Data Journal* **6**, 42–49 (1983).

[62] D. R. MacFarlane, P. J. Newman, J. D. Cashion, and A. Edgar. *J. Non-Cryst. Solids* **256&257**, 53 (1999).

[63] J. M. D. Coey, A. McEvoy, and M. W. Shafer. *Journal of Non-Crystalline Solids* **43**, 387–392 (1981).

[64] Eugene P. Wigner. *Group Theory*. Academic Press, London, (1959).

Publications

J. Selling, S. Schweizer, M. D. Birowosuto, and P. Dorenbos
Eu- or Ce-doped barium halide scintillators for x-ray and γ-ray detections
IEEE Transactions on Nuclear Science (submitted)

B. Ahrens, J. Selling, C. Eisenschmidt, A. Engel, and S. Schweizer
Sm-activated barium halide nanocrystals in fluorozirconate glasses
Nuclear Instruments and Methods in Physics Research Section B (submitted)

J. Selling, M. D. Birowosuto, P. Dorenbos, and S. Schweizer
Europium-doped barium halide x-ray scintillators
physica status solidi (c) **4**, No. 3, 976-979 (2007)

J. Selling, M. D. Birowosuto, P. Dorenbos, and S. Schweizer
Europium-doped barium halide scintillators for x-ray and γ-ray detection
Journal of Applied Physics **101**, 034901 (2007)

A. Engel, C. Ottermann, U. Resch-Genger, K. Hoffmann, S. Schweizer, J. Selling, J.-M. Spaeth, and V. Rupertus
Glass based fluorescence reference materials used for optical and biophotonic applications
Biophotonics and New Therapy Frontiers, edited by Romualda Grzymala, Olivier Haerberle, Proceeding of SPIE **6191**, 619110 (2006)

J. Selling, G. Corradi, M. Secu, and S. Schweizer
Rare-earth doped barium halide x-ray storage phosphors and scintillators
in: Proceedings of the Eighth International Conference on Inorganic Scintillators and their Use in Scientific and Industrial Applications, Alushta, Crimea, Ukraine, September 19-23, 2005, ed. by A. Gektin and B. Grinyov (National Academy of Sciences of Ukraine, Ukraine - Kharkov, 2006), p. 415 ISBN 9666-02-3884-3

J. Selling, G. Corradi, M. Secu, and S. Schweizer
Comparison of the luminescence properties of the x-ray storage phosphors $BaCl_2$:Ce^{3+} and $BaBr_2$:Ce^{3+}
Journal of Physics: Condensed Matter **17**, 8069-8078 (2005)

J. Selling, S. Schweizer, J.-M. Spaeth, G. Corradi, A. Edgar, G. V. M. Williams
Radiation defects in Ce-doped $BaCl_2$ and fluorochlorozirconate glass-ceramic X-ray storage phosphors
physica status solidi (c) **2**, No. 1, 592-595 (2005)

Danksagung

Diese Arbeit entstand unter Leitung von Herrn PD Dr. Stefan Schweizer, bei dem ich mich für die Aufnahme in seine Arbeitsgruppe, die interessanten Aufgabenstellungen und die sehr gute Betreuung bei dieser Arbeit bedanke.

Herrn Professor Dr. G. Wortmann danke ich für viele fachlichen Diskussionen und Hinweise, sowie für sein Interesse an dieser Arbeit. Außerdem bedanke ich mich bei ihm und seinem Mitarbeiter Bernd Bielemeier für alle durchgeführten Mössbauer Messungen − sei es zur Kontrolle oder zur Vervollständigung der Ergebnisse gewesen.

Diese Arbeit wurde von der Firma Schott im Rahmen des BMBF geförderten Projektes FLUOPLEX (Projektnummer 13N8849) finanziell unterstützt. Herrn Dr. A. Engel danke ich hierbei für die gute Zusammenarbeit.

Dem Deutschen Akademischen Austausch Dienst (DAAD) danke ich für die finanzielle Unterstützung durch eine Kurzzeit-Doktorandenstipedium, das mir den Forschungsaufenthalt an der Northern Illinois University (NIU), USA ermöglichte. Während dieses Aufenthalts ist ein Großteil der Mössbauer-Ergebnisse entstanden.

Prof. Dr. Dennis E. Brown danke ich für die Aufnahme in seine Arbeitsgruppe und die Benutzung seiner Labore während meines Aufenthalts an der NIU. Ebenso danke ich Prof. Dr. Charles E. Johnson für viele hilfreiche fachliche Gespräche während dieser Zeit. Hilfreich waren ebenfalls die vielen E-Mails nach meiner Rückkehr nach Paderborn. Dr. Jackie Johnson danke ich für das Korrekturlesen einiger Kapitel meiner Arbeit.

Weiterhin danke ich Dr. Pieter Dorenbos und seinem Mitarbeiter Danang Birowosuto von der TU Delft, Niederlande für die gute Zusammenarbeit. Aus dieser Zusammenarbeit sind einige Veröffentlichungen und das Kapitel "Barium halide scintillators for x-ray and γ-ray detections" dieser Arbeit hervorgegangen.

Meinen Bürogenossen − aktuellen und ehemaligen − Bastian Henke, Bernd Ahrens und Jörg Hallmann danke ich für offene Ohren, zahlreiche physikalische und unphysikalische Gespräche, die gute Zusammenarbeit und ihre gute Laune.

Für die Versorgung mit flüssigem Helium und Stickstoff danke ich Herrn J. Pauli. Weiterhin möchte ich mich bei den Kollegen des Kristallzuchtlabors Herrn D. Niggemeier und Herrn R. Winterberg für die Herstellung und Bearbeitung meiner Proben bedanken.

Allen aktuellen und ehemaligen Gruppenmitgliedern von der Ebene A4 sei an dieser Stelle für das immer angenehme Arbeitsklima herzlich gedankt.

Mein Dank gilt auch den tapferen Helfern, die sich zwecks stilistischen und orthografischen Korrekturvorschläge durch meine Arbeit gekämpft haben.

Ebenso bedanke ich mich bei allen, die nicht namentlich Erwähnung fanden, aber zum Gelingen dieser Arbeit beigetragen haben.

Last, but not least danke ich meinen Eltern und meinem Freund, für ihre liebevolle Unterstützung und Hilfe, die aufmunternden Worte und den sanften Druck, diese Arbeit zu einem erfolgreichen Abschluss zu bringen.